2022

New Roles for the Integrated Stress Response in Cancer and Proteostasis

Brian Hurwitz

New roles for the integrated stress response in cancer and proteostasis

A Thesis Presented to the Faculty of
The Rockefeller University
in Partial Fulfillment of the Requirements for
the degree of Doctor of Philosophy

by
Brian Hurwitz
June 2022

New roles for the integrated stress response in cancer and proteostasis

Brian Hurwitz, Ph.D.
The Rockefeller University 2022

The integrated stress response (ISR) is a highly conserved pathway that senses diverse stresses and responds by limiting total protein synthesis and redirecting translation to stress response transcripts. The ISR has the potential to modify a broad range of processes in cancer, but the major cancer-relevant functions of the pathway have remained elusive due to the complex and redundant nature of the upstream kinases that sense stress and activate the pathway. To overcome this challenge, we genetically targeted the central, regulatory node of the pathway, eIF2α-serine 51, directly, in primary squamous cell carcinoma cells to generate "ISR-null" SCCs. We surprisingly found that the ISR acted as a tumor suppressor early in tumorigenesis, but also promoted proteostasis in response to the chemotherapy and proteasome inhibitor, bortezomib. We found this second finding to be mechanistically linked to a previously-undescribed role for the ISR in regulating the microtubule cytoskeleton to promote the removal of aggregated proteins. As a second goal of this project we sought to develop small molecule inhibitors of the ISR for anticancer therapy, focusing on the alternative translation initiation factor, EIF2A, which we previously found to be critical for oncogenesis. Utilizing dual luciferase reporters for alternative translation (Atf4-*firefly*) and housekeeping translation (HBB-*renilla*) we performed a high throughput screen and have identified promising hits with potential as novel EIF2A inhibitors.

Dedicated to my grandfather, John Boezi, whose untimely passing prevented us from ever meeting and talking science. Thank you for being the first in our family to blaze this trail and for showing me what is possible. Stories about your life and your passion for science have been such important sources of inspiration for me.

Acknowledgements

I owe a huge debt of gratitude to my mentor, Dr. Elaine Fuchs. Throughout my training you have been a role model, source of support, and an inspiration. I've learned so much in your lab. Over time I've gained more appreciation for how special this place is to train. This environment has provided me with opportunities to take my own risks and make my own mistakes, and it has also provided the support and guidance needed to get through the challenges. You've taught me what I now see to be one of the most important challenges for a scientist, to be rigorous and detail oriented without losing sight of the big picture. I feel so privileged for the opportunity to train with you. Thank you for taking me into your lab and pushing me to be the best scientist I can be.

I also want to thank the members of my faculty advisory committee: Dr. Charlie Rice, Dr. John Blenis, and Dr. Bob Darnell. It has been a privilege to present my work to this group, and I've learned so much from each one of you. Our meetings have been the major milestones by which I've judged my progress, and the feedback from this group has majorly influenced my work. Moreover, these meetings have shaped me as a scientist. I can think of comments and feedback from each one of you that stuck with me for months after the meetings and shaped my thinking. I will always be grateful for the experience of learning from this group. I would also like to thank Dr. Michael Rapé for serving as the external examiner for my dissertation defense. It is an honor that you accepted this invitation, and I am excited for the opportunity to learn from you.

When I first rotated in the Fuchs lab in the summer of 2015 I trained under the mentorship of Dr. Ataman Sendoel, then a postdoc and now on the faculty at the University of Zurich. That rotation was such a fun and inspiring experience. I learned so much from doing experiments with you, and I certainly internalized your passion for researching the cell biology and translational control pathways of cancer. Thank you for also being such an important mentor when I began my thesis work this lab, and thank you for helping me to shape this project and progress to work independently. Most importantly, I am grateful that working together has served as the beginning of longer relationship. I'm lucky that you are still an important scientific mentor, collaborator, and friend.

I have been lucky to learn from many members of the Fuchs lab, which has always been such an inspiring and dynamic group, and there are a few collaborators to whom I want to offer a special thanks. First, I am grateful for the opportunity to have worked with Dr. Vince Fiore starting in 2020. I've learned a ton from you, not the least of which are microscopy skills that are now a point of pride for me. More importantly, I learned how great it is to collaborate scientifically with a friend. Brainstorming and planning experiments together really added a new layer of fun and excitement to this project. I would also like to thank Dr. Nicola Guzzi, with whom I have collaborated closely over the past year. Pulling off our big ribosome profiling experiment together was one of the highlights of my PhD. I've learned so much from your wealth of knowledge in the fields of translation and molecular biology, and I'm grateful we overlapped in the lab for the time we did.

I also want to acknowledge the technical staff in the Fuchs lab. You all really are the glue that keeps this lab together and running smoothly. Everything from planning mouse experiments to ordering reagents is so much easier because of the hard work of this group. You are all also such nice people and contribute so much to the positive environment in this lab. I also owe a special thanks to Maria Nikolova. I'm grateful that you've worked with me on the parts of this project that have required the most intensive cell culture. Making these CRISPR clones and doing the drug screen would not have been possible without you. I also really enjoy working with you and I will always be grateful for those experiences.

I want to thank all of the members of the Fuchs lab, past and present, for everything you have done to shape this experience. It's hard to imagine a more exciting and engaging group to be part of and do science with. I really have enjoyed it all from journal clubs to happy hours to March Madness competitions. Even during the pandemic when we spent less time together this group remained impressively engaged with each other's projects. We have all benefited from this environment, in which we push each other but also support and respect each other. I also want to acknowledge the original cytoskeleton subgroup within the lab. Although I wasn't directly working on the cytoskeleton until later on, I was well prepared when the time came.

I would also like to acknowledge the Tri-Institutional MD/PhD program for support throughout this process. I've been lucky to be part of a great community of people going through a similar educational experience. As well the program leadership was the reason I chose to enroll in this program, and they have been so helpful throughout the PhD. I want to thank Dr. Olaf Andersen, Dr. Jochen Buck, Dr. Ruth Gotian, Dr. Catherine Boothyard, and Dr. Kathy Hsu. I am also grateful for the chance to be part of the Rockefeller University Graduate Program. Rockefeller is a special place to train and do science. I feel lucky to have been part of this community, and I'll miss it dearly. I want to extend a special thanks to the Dean's office for the support throughout the entire time, and especially during the thesis defense process.

I’m also very grateful for my undergraduate community and mentors. The Biomedical Science Major at The Ohio State University was the perfect place for me to be at that stage. I received a lot of support that program, and I’m especially grateful for Dr. Gunn, Lori Martensen, and Steve Mousetes. An especially big thank you to my undergraduate PI, Dr. Balveen Kaur, and my mentor, Dr. Ji Young Yoo. Thank you for taking me in, taking the time to teach me the basics, and helping me grow the confidence to continue in science.

And now an enormous thank you to my family and friends who I love so much. To my Mom and Dad, thank you for all the support throughout the years. You’ve made so many sacrifices for your children, and I owe so much to you both. Mom, thank you for all of the support and encouragement throughout all of my education. From rides to school to now, you’ve always been so great to talk to about both the successes and the challenges, always so supportive of my path and excited to hear what’s going on. Dad, you’ve always been such an important part of this educational journey, going back to high school, college visits, and all the way forward to our conversations now. Thank you for all of the conversations, advice, and perspective that have helped me to find my path in the world. A huge thank you to my sisters, Nicole and Elise, as well. I feel so blessed to have such positive relationships with you both, and it’s always great to catch up and tell each other what we’re up to. Thank you as well to my Mother and Father-in-law, Dorota and Chris. I’m so grateful to have you both as new family, and I really appreciate all the support over the past few years. I would also like to say thank you to all of my extended family members who have supported me in this process, especially my grandma, Nannie, listening and sharing your own special insights about a life in science. Thank you all for all of your support, I love you all tremendously. I also owe a huge thank you to all of my friends who I share so many fun experiences with and who help keep my life balanced and happy.

I would finally like to thank my most important source of support, my partner in crime, my wife, Caitie. Navigating our shared life together is the most rewarding part of this all. Our marriage and our special time together is my rock and the foundation I come back to when I need to find my center. Thank you for always being such a wonderful energy to come home to, and thank you for all of the ways you've supported me throughout the years, big and small. I couldn't do this without you. I love you more than words can express, and I'm so grateful to be on this journey with you as we go through life and continue to learn what matters most, together.

Significant Contributions

This work was made possible thanks to the collaboration of many individuals. First, Dr. Ataman Sendoel was instrumental in shaping the project in the early days. We collaborated on many experiments early on, and have continued to collaborate on the drug screen presented in chapter 6. Specifically, Dr. Sendoel ran and analyzed the experiments to identify EIF2A as a target in cancer, and he ran mass-spec experiments to identify translation targets of EIF2A. We collaboratively built early generations of these reporters which I continued to optimize after Dr. Sendoel opened his own lab at the University of Zurich. At this point Dr. Sendoel and colleagues have generated and tested the cell lines we used as reporters and have provided useful guidance planning and interpreting experiments. The Tri-Institutional Drug Discovery Institute was also instrumental in our drug screening efforts, especially Dr. Peter Meinke, Dr. Leigh Baxt, and Dr. Tanweer Khan, who provided helpful guidance and critical reagents.

Ribosome profiling presented in chapter 5 was performed in collaboration with Dr. Nicola Guzzi, who brought his extensive expertise with this method to the lab and spearheaded our own successful experiment. The bioinformatic analyses for ribosome profiling were done in collaboration with the Rockefeller University Bioinformatics Core Facility, with effort from Dr. Doug Barrows, Dr. Ji-Dung Luo, and Dr. Tom Carroll. Much of the confocal microscopy and analyses of aggresomes was done in collaboration with Dr. Vincent Fiore, who generated the microscopy data demonstrating that aggresomes are absent in cells lacking the ISR. Even after he left the lab, Dr. Fiore has provided guidance and feedback related to microscopy, proteostasis, and the cytoskeleton.

Maria Nikolova, Fuchs lab manager provided a significant amount of technical support throughout this project. Maria did much of the cell culture required to generate CRISPR-KO cell lines and perform high-throughput screening. I also want to acknowledge rotation students that I have worked with who have provided help at different times: Nneoma Adaku, Alex Stuart, and Eriko Koide. Finally, Rockefeller University's world class core facilities have been tremendously helpful for this project. In addition to the bioinformatics core which was mentioned earlier, Flow cytometry was done with the help of the FACS core led by Dr. Svetlana Mazel, The genomics core led by Dr. Connie Zhao helped plan and execute all high-throughput sequencing experiments, and the electron microscopy was performed in the core facility run by Dr. Amalia Pasolli. The High-throughput and spectroscopy resource center led by Dr. Fraser Glickman provided technical assistance and helped plan all drug screening experiments. Members of that group, Dr. Lavosier Ramos-Espritu and Chloe Larsen deserve special acknowledgement for their help with the screening project as well.

Table of Contents

Chapter 1: Generating and validating ISR-null primary SCC cells…………………...8

Chapter 2: Phenotype of ISR-null SCC tumors relative to controls……..…………23

Chapter 3: ISR-null cells have defects in multiple processes mediated by the cytoskeleton……………………………………………………………………………..………38

Introduction

Proteins are the functional products of genes that do the work of life. These versatile biomolecules shoulder responsibilities as varied as carrying oxygen, sensing light, and giving shape to organisms. Although most organisms contain enough genes to encode for tens of thousands of proteins, no single cell in these organisms expresses the entire library of proteins at once. Instead, cells become specialized for certain roles, producing insulin for example, by selectively "expressing" the proteins needed for the task. Cells cannot, however, just settle on one limited toolbox of proteins forever. For an organism's entire life its cells will encounter frequent challenges and stresses, and cells must be able to adapt. Stress adaptation may require new, previously unexpressed proteins to be produced for the sake of survival. If, for example, an insulin producing cell resides in someone with prediabetes, the cell's insulin production machinery will gradually become overwhelmed by the high demand for insulin, but this cell can adapt by expressing new proteins that augment the cell's ability to produce and secrete insulin. Thus, in every cell protein expression is dynamic and responsive.

Much of the research into the regulation of protein expression has focused on how cells select and transcribe the messenger RNA (mRNA) "middleman" from genes stored on DNA. Comparatively less research has investigated how these mRNA molecules are selected for translation into functional protein. Research has uncovered, however, that protein levels do not necessarily correlate with mRNA levels, suggesting that translation may be regulated by complex and presently unappreciated processes (Schwanhausser et al., 2011). Although many of the molecular mechanisms regulating dynamic translational changes appear to be incompletely understood, it is clear that translational control plays a major role in protein expression changes associated with cellular stress (Ingolia et al., 2009) That is, by cutting out the time consuming steps of mRNA transcription, processing, and transport, a cell can more quickly respond to stress by increasing translation of preexisting stress-response genes. One pathway called the "integrated stress response" or ISR, is known to do just that (Costa-Mattioli & Walter, 2020; Harding et al., 2003; Starck et al., 2016).

The ISR was first characterized as the "general control response", a cellular program that helps yeast cells cope with a low-nutrient environment by sensing this stressful state and adapting by producing new amino acid biosynthetic enzymes (Hinnebusch, 1988). This works through a unique mechanism in which a kinase, Gcn2, senses uncharged tRNA molecules and phosphorylates a translation initiation factor, eIF2α, with the consequence that the efficiency of translation initiation is decreased for most genes but paradoxically increased for a transcription factor, Gcn4 (Dever et al., 1992; Wek et al., 1990). It was determined that Gcn4 was induced because the transcript contained upstream open reading frames in its 5' untranslated region (5' UTR) (Dever et al., 1992).

The ISR is conserved across all eukaryotes, and over the course of evolution the pathway has expanded in its complexity (Harding et al., 2000; Pakos-Zebrucka et al., 2016). While yeast contain a single eIF2α kinase that senses nutrients, mammalian genomes encode for three additional kinases which were discovered to sense unfolded proteins in the endoplasmic reticulum, double-stranded RNA characteristic of viruses, and conditions of low cellular iron. Further increasing the complexity of the pathway, the four mammalian kinases are now appreciated to sense even more diverse stresses and have some level of functional redundancy (Costa-Mattioli & Walter, 2020). This may explain why mice with the individual kinases knocked-out have absent or mild phenotypes. The pathway, however, is still clearly important because mice with complete ISR-ablation caused by the common serine target, eIF2α-S51, being converted to alanine (S51A) die within hours of birth (Scheuner et al., 2001).

Due to kinase redundancy and the lethal phenotype when eIF2α is directly targeted with a serine to alanine mutation, it has been challenging for the field to develop a comprehensive understanding of the significance the pathway plays *in vivo*. Nonetheless several seminal studies have provided examples of how the ISR can profoundly influence health and disease. Investigation into the cause of the lethal phenotype of S51A/S51A mice revealed that the pathway is required for a successful transition away from placental nutrients during the "neonatal starvation period" (Scheuner et al., 2001). This was due to the ISR being critical for the physiologic response to a low nutrient state in multiple tissues including liver, muscle, and pancreatic beta cells. Strategies to conditionally ablate the ISR in vivo have relied on rescuing expression of eIF2α-S51 in all cells of an S51A/S51A mouse with a floxed rescue allele, and then using Cre-drivers to eliminate the wild-type allele in specific cells (Back et al., 2009; Ghaddar et al., 2021). This approach can be useful but has two major limitations, the first is that cells without Cre-expression have only a single copy of eIF2α-S51 expressed from a non-endogenous promoter, which are not likely to be normal given the existence of a phenotype of heterozygous S51/S51A mice. The second limitation of this approach is that ablation of the ISR in these cells coincides with a change in copy number of the eIF2α gene, a gene essential for growth, which may provide a disadvantage independently of ISR-activity.

The ISR also appears to play a major role in brain health and disease. On one hand mutations in eIF2γ which mimic constitutive ISR activation produce MEHMO syndrome, a rare disorder characterized by intellectual disability, epilepsy, hypogonadism, microcephaly, and obesity (Skopkova et al., 2017; Young-Baird et al., 2020). Mutations in eIF2B that additionally mimic constitutive ISR activation, albeit to different extent, cause a highly heterogeneous and progressive leukodystrophy termed Vanishing White Matter Disease (Leegwater et al., 2001; Schiffmann et al., 1994; Wong et al., 2018).

On the other hand mice with partial inhibition of the ISR (Gcn2-KO, PKR-KO or S51/S51A heterozygotes) display improved learning and memory due to the pathway's apparent dominant role in regulating striatal dopamine signaling (Costa-Mattioli et al., 2005; Costa-Mattioli et al., 2007; Helseth et al., 2021; Zhu et al., 2011). Moreover, ISR inhibition can improve memory and learning in mouse models of Down Syndrome, aging, and traumatic brain injury (Chou et al., 2017; Krukowski et al., 2020; Zhu et al., 2019).

These examples demonstrate the potential for the ISR to play a role in many diseases characterized by cellular stress. One particular disease, cancer, is well known for being characterized by cells surviving despite being in a stressed state (Hanahan & Weinberg, 2000, 2011). Studies of the ISR in cancer have been somewhat conflicting, though generally falling on the side that the ISR is oncogenic. Early studies demonstrated that mouse embryonic fibroblasts homozygous for S51A are transformed, but live mice with reduced p-eIF2α (heterozygous for S51A) do not have any increased tumor burden. On the other hand eIF2α kinases, Perk and Gcn2, have been reported to promote cancer by promoting survival in the face of reactive oxygen species and low amino acids, respectively. Additional studies targeting the ISR pharmacologically in prostate cancer and with a rescue allele strategy in lung adenocarcinoma also suggest the pathway is oncogenic (Ghaddar et al., 2021; Nguyen et al., 2018). Moreover, work from our lab has demonstrated that early squamous cell carcinoma lesions have rewired protein synthesis landscapes consistent with ISR activity (Sendoel et al., 2017). That is, these cells display low protein synthesis rates and depend on the alternative translation initiation factor, eIF2A, for tumorigenesis *in vivo*.

Similarly to the case with mouse models, our understanding of the ISR in cancer limited by a paucity of studies directly and completely ablating the pathway in relevant cancer models. In this thesis I seek to contribute to the field by generating and characterizing primary squamous cell carcinoma (SCC) cell lines with complete loss of the ISR by replacing endogenous eIF2α with eIF2α-S51A. I unexpectedly found that complete ablation of the ISR pathway actually increased the efficiency of tumorigenesis in this model. At later timepoints the ISR-null SCCs and controls appeared to progress similarly, but ISR-null cells were more sensitive to proteotoxic stress induced by proteasome inhibition. These findings illustrate the complexity of this pathway's role in cancer and the need for direct genetic experiments in additional cancer models in the future.

The second major goal of this thesis is to advance the promise of ISR-inhibition for therapeutic purposes. Although there is still much to be learned about the various roles of this pathway in human health and disease, I expect that pharmacologically inhibiting this pathway could influence the natural course of diverse diseases, including cancer. This potential is highlighted first and foremost by the groundbreaking discovery of one

ISR-inhibiting molecule (ISRIB) by the lab of Peter Walter (Sidrauski et al., 2013). This group's high-throughput screen for chemical inhibitors of stress-translation identified ISRIB as a potent and selective inhibitor of the pathway. The molecule works by a unique mechanism of action, acting as a "molecular stapler", dimerizing eIF2B and inhibiting the ISR regardless of the phosphorylation status of eIF2α.

This compound's discovery has already led to new insights into both the intracellular mechanisms that govern the ISR and also the physiologic roles of the pathway *in vivo*. In fact, ISRIB has demonstrated tremendous therapeutic potential in mouse models of a broad range of diseases ranging from traumatic brain injury, down syndrome, prostate cancer, and necrotizing fasciitis (Anand et al., 2021; Chou et al., 2017; Nguyen et al., 2018; Zhu et al., 2019). This work made it additionally apparent that ISRIB has little to no side effects even at high doses, a surprising, yet exciting, finding that spurred further molecular characterization which revealed that ISRIB inhibits the ISR only when pathway activation is limited in duration and intensity (Rabouw et al., 2019).

While this molecular quirk of ISRIB gives it high therapeutic index that will make it useful for some diseases, especially those in which chronic treatment is warranted, I expect that a complete arsenal of ISR-inhibitors should include compounds that block the pathway completely and continuously regardless of the strength and kinetics of ISR activation. For this reason, in collaboration with Dr. Ataman Sendoel, I set out to perform our own high-throughput small molecule screen with the goal of finding compounds that inhibit the ISR through a different mechanism. Specifically, whereas ISRIB blocks the ISR by reversing pathway activation, I hoped to discover compounds that leave the translational shut down of the ISR intact while inhibiting the selective translation of stress-response proteins.

Previous work from our lab and others has identified an alternative translation initiation factor, EIF2A, as a promising target to inhibit stress translation downstream of ISR activation. Not to be confused with eIF2α, EIF2A mediates the translation of stress-response genes when eIF2α is phosphorylated. Moreover, we have previously found EIF2A knockout to block SCC tumorigenesis (Sendoel et al., 2017), highlighting the anticancer potential of inhibiting the downstream alternative translational machinery rather than blocking initial activation of the pathway by targeting eIF2α or eIF2B.

Building on the successful screen from Peter Walter's lab that identified ISRIB, I built a new dual luciferase reporter cell line to simultaneously report on both housekeeping gene translation and stress gene translation. By screening for compounds that inhibit stress-translation without rescuing housekeeping translation, I have identified promising compounds that may serve as building blocks for future ISR-inhibiting therapeutics. Work is in progress to validate target binding and characterize these compounds further.

This work contributes to our knowledge of the integrated stress response pathway by characterizing an ISR-null cancer model, and this work additionally progresses the future therapeutic potential of targeting this pathway by building a drug discovery platform to identify ISR-inhibitors with a new mechanism of action.

Chapter 1:

Generating and validating ISR-null primary SCC cells

Part 1 - The integrated stress response and strategies for genetic manipulation.

The ISR is a complex pathway comprised of a number of regulatory kinases, phosphatases, and effector proteins (Figure 1) (Berlanga et al., 1998; Dever et al., 1992; Meurs et al., 1990; Pakos-Zebrucka et al., 2016; Shi et al., 1998). I began this investigation by considering what new tools would be required to dissect the role of this pathway in SCC biology. Potential strategies included knocking down or knocking out eIF2α kinases in order to decrease p-eIF2α levels (Harding et al., 2001; Yang et al., 1995; Zhang et al., 2002), ablating or overexpressing phosphatase regulatory proteins, CReP or GADD34, in order to increase or decrease p-eIF2α (Harding et al., 2009; Kojima et al., 2003), or, finally, substituting serine 51 of eIF2α for alanine to create a phospho-dead eIF2α and thus directly ablate all pathway activity (Harding et al., 2003; Scheuner et al., 2001).

Figure 1.1: The integrated stress response.

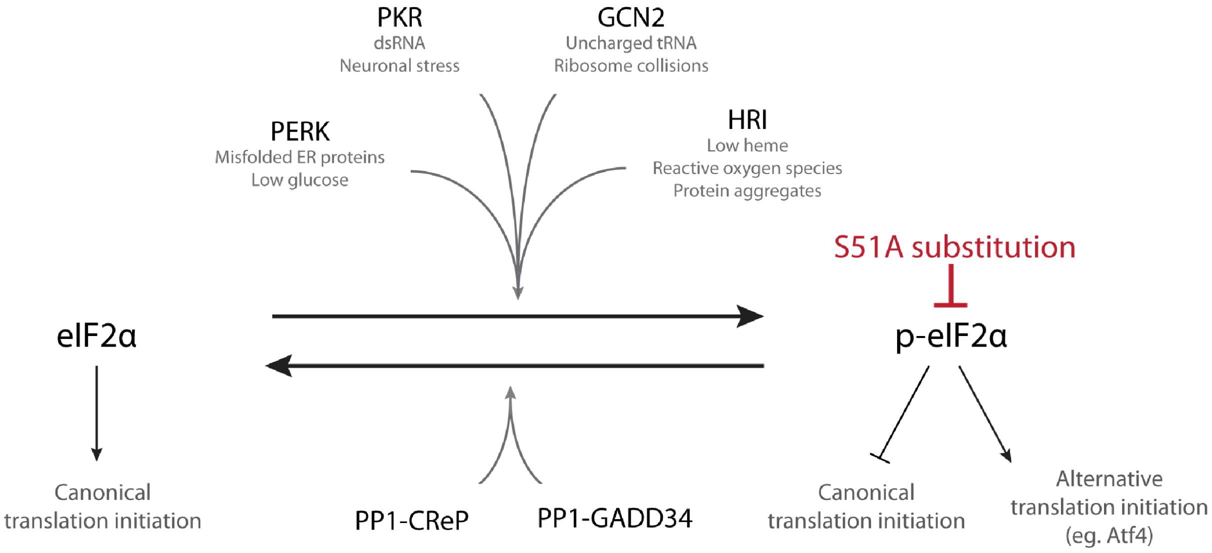

Figure 1.1: The integrated stress response.
A schematic of the major ISR regulators and effectors is depicted. After sensing their respective stressors, kinases PERK, PKR, GCN2, and HRI phosphorylate serine 51 of eIF2α, which inhibits canonical translation and activates alternative translation through a mechanism that involves eIF2α inhibiting its own GEF, eIF2B (not shown). Following resolution of the inciting stress, the ISR is deactivated by phosphatase complexes PP1-CReP, which is expressed constitutively, or PP1-GADD34, which is induced by the ISR as negative feedback.

While the regulatory kinases and phosphatases in the pathway have been targets of broad cancer research (Ghaddar et al., 2021; Lehman et al., 2015; Rouschop et al., 2013; Tian et al., 2021), no lab had previously generated an SCC model with the ISR-directly ablated with an eIF2α-S51A substitution. I expected that this approach would be most likely to inform a more definitive understanding of the role of the ISR in this cancer, and I also hoped that directly ablating the pathway in a new cell type would provide the potential to uncover novel ISR biology.

After considering our available SCC models, I chose to work with a primary murine SCC cell line previously generated by our lab (Yang et al., 2015). This cell line was previously generated by Drs. Hanseul Yang and Daniel Schramek during their time in the Fuchs Lab. The line was created by isolating primary, neonatally-derived keratinocytes that were transformed in vitro by retrovirus-mediated integration of HRas-G12V, an oncogenic mutation that frequently drives human SCC (Chen et al., 2009; Nassar et al., 2015). As a second oncogenic hit, these cells were isolated from mice with both alleles for TGFβ-receptor 2 floxed (TGFβRII-fl/fl), and Cre was induced with a Cre-GFP construct transduced by adenovirus. TGFβRII knockout bypasses the tumor-suppressive role of the TGFβ pathway and allows for consistent formation of SCCs (Bian et al., 2009; Guasch et al., 2007). This model provides the advantage of inducing aggressive cancers when transplanted into nude/nude mice while remaining amenable to the complex genetic manipulations required for complete ablation of the ISR.

Part 2 - High-throughput CRISPR-Cas9 genome editing in a complex genome.

The recent advent of genome editing with CRISPR-Cas9 provided a promising new toolbox for targeting the endogenous eIF2α allele (Doudna & Charpentier, 2014; Jiang &

Doudna, 2017). To generate these genetically modified cell lines I used a recently developed approach of liposome-mediated transfection of preformed ribonucleoproteins (RPNs) made of CRISPR-Cas9 bound to fluorescent (ATTO550-conjugated) guide RNA (gRNA) (DiNapoli et al., 2020). By transiently transfecting these preformed RNPs, I could introduce a large number of RNP molecules into the cell while avoiding the long term expression of Cas9, gRNA, or selection markers. This approach also allowed for fluorescence-activated cell sorting (FACS) to enrich for successfully transfected cells by sorting for ATTO550-postive cells (Fig. 1.2 A). Using this approach and with the help of the Rockefeller University flow cytometry core facility, I generated clones derived from single cells sorted into 96-well plates in order to generate sets of isogenic, clonal cell lines optimized for stability in culture.

While this approach allowed for the generation a large number of putatively edited cell lines, it also created a challenge. Analyzing the outcomes of genome editing in a large number of samples was extremely cumbersome, so I developed a high-throughput method to quantify the number of edited verses wild-type alleles. When CRISPR-Cas9 creates a double-stranded break in a eukaryotic genome, the cell often repairs the cut using the non-homologous end-joining pathway, which introduces indels that may cause a frameshift and disrupt the expression of encoded proteins (Sansbury et al., 2019).

To quantify the alleles present following genome editing and clone generation, I isolated genomic DNA (gDNA) from a small number of cells from each clone and used a polymerase chain reaction (PCR) with primers containing 5' adapters to amplify PCR products of around 400 basepairs with the CRISPR-Cas9-targeted locus in the center. Following a PCR-cleanup in 96-well plates, I could then use a second indexing PCR to add unique molecular barcodes to each samples. These samples were then pooled and sequenced on an Illumina MiSeq Nano in the Rockefeller University Genomics core facility to quantify edited alleles (Fig 1.2. B). Up to 200 clones can be simultaneously analyzed using this method, and by capturing thousands of reads per sample and aligning to the target region we could easily validate the exact consequences of genome editing by comparing the different indels or wild-type alleles present as allelic ratios. When the goal was to knock out a gene, success would be evident if all alleles detected in a cell line were indels that would put the encoded protein out of frame.

Because I was editing cancer cells, which often have complex and dynamic aneuploidy (Davoli & de Lange, 2011; Rajagopalan & Lengauer, 2004), I wished to confirm that I could successfully knock out genes regardless of gene copy number. Following test runs of the process targeting ISR-related proteins (Atf4, EIF2A, and PHGDH), I compared the genomic copy number of each gene by using our sequencing approach to quantify the allelic ratios of CRISPR-Cas9-induced indels. I found genomic copy number was indeed heterogenous within cancer cells and differed by locus target (Fig 1.2 C). I were reassured to find, however, that our approach consistently yielded a allelic-editing efficiencies between 60 and 100%, which produced frameshift-knockouts with up to 70% efficiency (Fig 1.2 D). With this efficient and scalable method in hand I was ready to generate SCC cells with complete ablation of the ISR pathway.

Figure 1.2: CRISPR-Cas9 RNP transfection and high-throughput sequencing analysis allows for knockouts in a complex genome.
A. Workflow to generate clonal, CRISPR-Cas9-edited cell lines. gRNA and ATTO-550-conjugated tracrRNA are complexed with Cas9 in vitro. RNPs are transfected into cells and clones are grown from single ATTO550-postive isolated by FACS.
B. Strategy for high-throughput analysis of outcome of indels generated by CRISPR-Cas9. The locus of interest is amplified using primers with adapters for Illumina sequencing, and following a second barcoding PCR amplicons are pooled and sequenced.
C. Quantifying indels following CRISPR-Cas9-mediated genome editing revealed heterogeneity in copy number that differed by genes.
D. CRISPR-Cas9 RNP method yielded indel-formation efficiencies of 60-100% and knockout efficiencies of up to 70%.

Figure 1.2: CRISPR-Cas9 RNP transfection and high-throughput sequencing analysis generates gene knockouts in a complex genome.

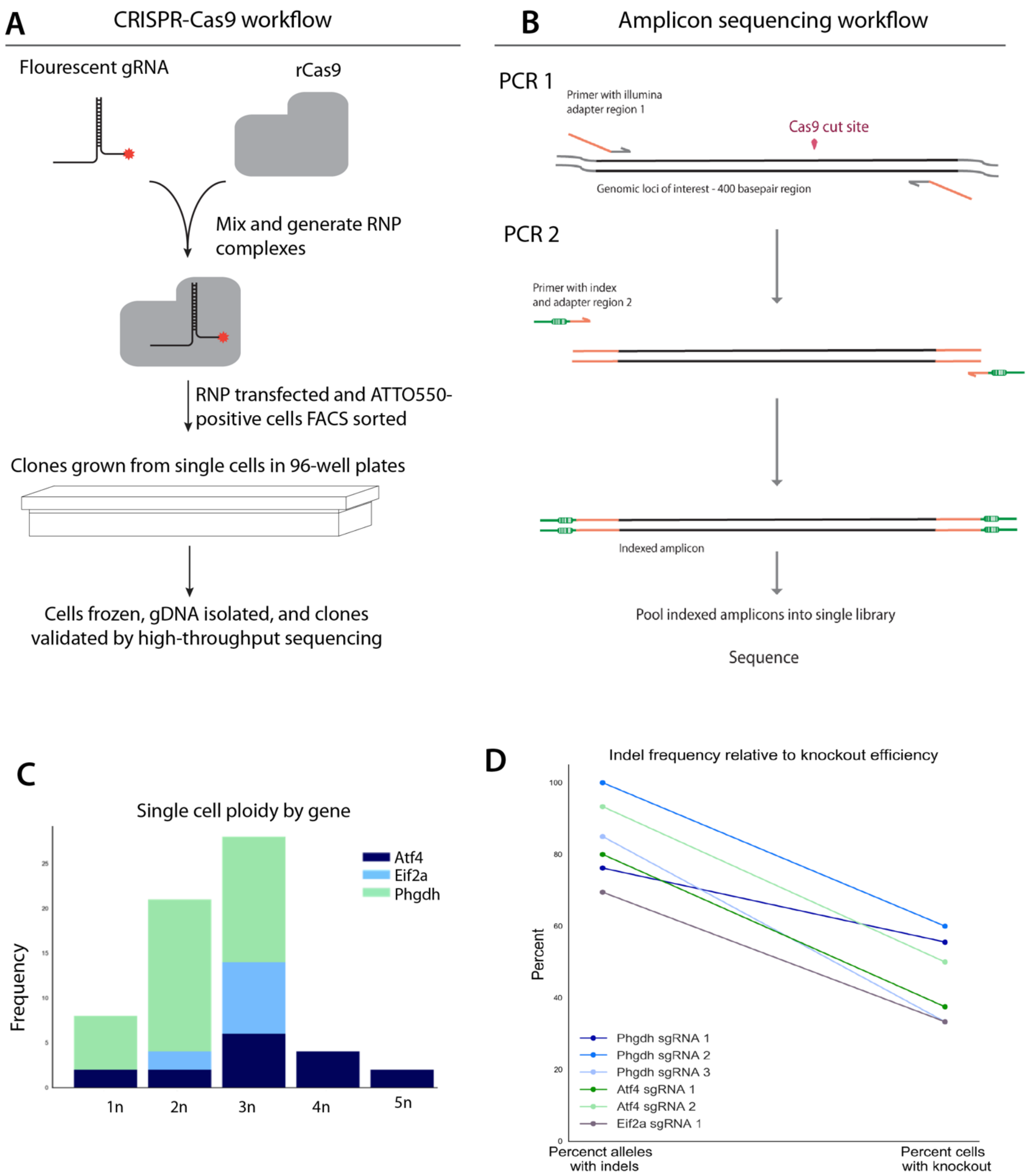

Part 3 - Generation and initial *in vitro* characterization of ISR-null cells.

Generating cell lines with complete ablation of the ISR required replacing all endogenous eIF2α alleles with alleles containing the serine 51 to alanine (S51A) substitution. I selected a "knockout and reconstitution approach" after unsuccessful attempts to use donor DNA and homologous recombination (HR) to introduce edits within the endogenous locus, a failure perhaps owing to dysregulated HR machinery in cancer cells (Helleday, 2010). In this knockout and reconstitution strategy, experimental myc-tagged S51A or control alleles were transduced with lentivirus followed by neomycin selection and knockout of the endogenous alleles (Fig 1.3 A). The experimental alleles were designed to be gRNA-resistant by introducing a synonymous mutation in the CRISPR-Cas9 PAM sight.

Cells were transfected with CRISPR-RNPs, ATTO-550-positive clones were sorted, and then analyzed them for successful knockout of the endogenous allele using primers specific for the genomic locus and high-throughput indel quantification. I found two control (S51) and two ISR-null (S51A) clones with only frameshift mutations at the endogenous locus (Fig. 1.3 B). These clones were expanded and confirmed as reconstituted ISR-null or control cells by western blot (Fig. 1.3 C, clone 1 for each genotype shown).

I began initial characterization of the new ISR-null SCC lines by simply evaluating the cell lines' proliferation rates and gross morphology in culture. Unsurprisingly, the control and ISR-null cells proliferated at the same rates in complete media lacking any endogenously introduced stressors (Fig 1.4. A). The control and mutant cells were also morphologically indistinguishable by bright-field microscopy (Fig 1.4 B)

Figure 1.3: Generation and validation of ISR-null cancer cells.

A

Parental cell line - primary mouse SCC
(HRas-G12V;TGFβ-RII KO)
↓
Integrate gRNA-resistant eIF2α transgene
PGK-eIF2α_MycTag-P2A-PuroR
↓
Clonal S51 and S51A SCC lines

B

Genotype & Clone	Alleles detected
WT clone 1 (WT3D10)	8 bp deletion
WT clone 2 (WT2G3)	8 bp deletion
S51A clone 1 (S51A8C3)	22, 10, 10 bp deletions
S51A clone 2 (S51A6G3)	10 bp deletion

C

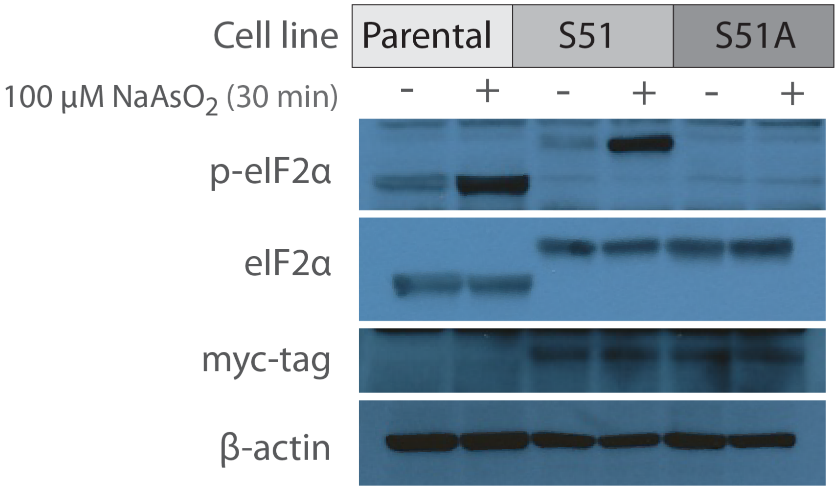

Figure 1.3: Generation and validation of ISR-null cancer cells.
A. Strategy for knockout and reconstitution of experimental eIF2α alleles. HT cells have rescue allele integrated by lentiviral transduction, and following neomycin selection endogenous allele is knocked out.
B. Indel analysis summary of two control and two S51A clones found to have successful knockout of endogenous eIF2α.
C. Western blot confirmation of knockout and reconstitution as well as lack of p-eIF2α in S51a cells.

Figure 1.4: ISR-null and control cells proliferate at the same rate and have similar morphology.

A. Proliferation assay of control and ISR-null SCC cells in culture. Doubling time is calculated by fitting exponential growth curve to raw data (Y=Y0*exp(k*X)).

B. Brightfield images of control and ISR-null SCC cells.

Figure 1.4: ISR-null and control cells proliferate at the same rate and have similar morphology.

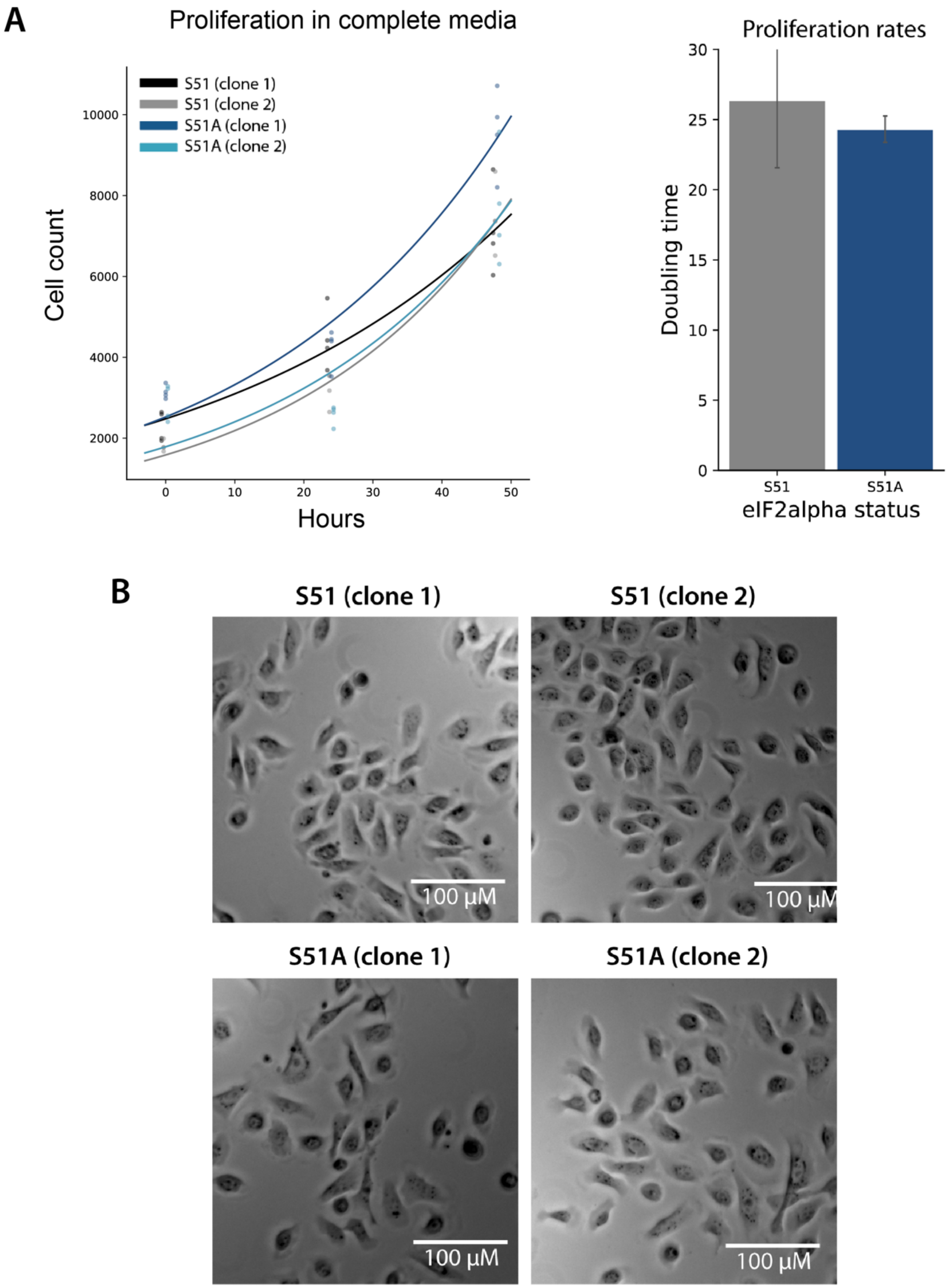

I next asked if the ISR-null SCC cells had any defects in response to stressors known to rely upon the ISR for management, which did turn out to be the case. The ISR induces a profound shutdown of canonical translation in response to stresses like ER-stress or sodium-arsenite stress (McEwen et al., 2005; Walter & Ron, 2011). While the control cells were found to decrease global translation rates as measured by OP-puromycin-conjugated fluorescence, a quantitative readout of global translation rates (J. Liu et al., 2012; Signer et al., 2014), the ISR-null cells failed to similarly decrease translation rates (Fig. 1.5 A). The ISR is also known to be required for the formation of stress granules, dynamic phase-separated structures that function to sequester mRNA molecules following translational shutdown (Sidrauski et al., 2015). ISR-null cells were unable to form stress-granules following the addition of sodium arsenite stress (Fig. 1.5 B). Finally, the ISR is required for cells to adapt to chronic ER stress induced by tunicamycin, a drug that inhibits ER N-linked glycosylation of new proteins (Buchan & Parker, 2009; Salaroglio et al., 2017). ISR-null SCC cells were significantly more sensitive than controls to tunicamycin, suggesting that SCC cells lacking this pathway are unable to adapt to an increased load of unfolded ER proteins (Fig. 1.5 D)

Figure 1.5: Cells with S51A substitution have defects in known ISR-mediated processes.

A. Translation rates of control and ISR-null cells subjected to sodium arsenite stress as measured by OP-puromycin fluorescence intensity.

B. Translation rates of control and ISR-null cells subjected to ER-stress induced by tunicamycin.

C. Stress-granules formed following sodium arsenite stress imaged using anti-G3BP1 antibody and quantified on fluorescence intensity.

D. Cell viability following 48 hour treatment of tunicamycin measured by Cell Titer Glo kit (Promega). LD50 values calculated by fitting dose response curve (inhibitor vs. response with variable slope: Y=Bottom + (Top-Bottom)/(1 + ((X^HillSlope)/(IC50^HillSlope)))).

Figure 1.5: Cells with S51A substitution have defects in known ISR-mediated processes.

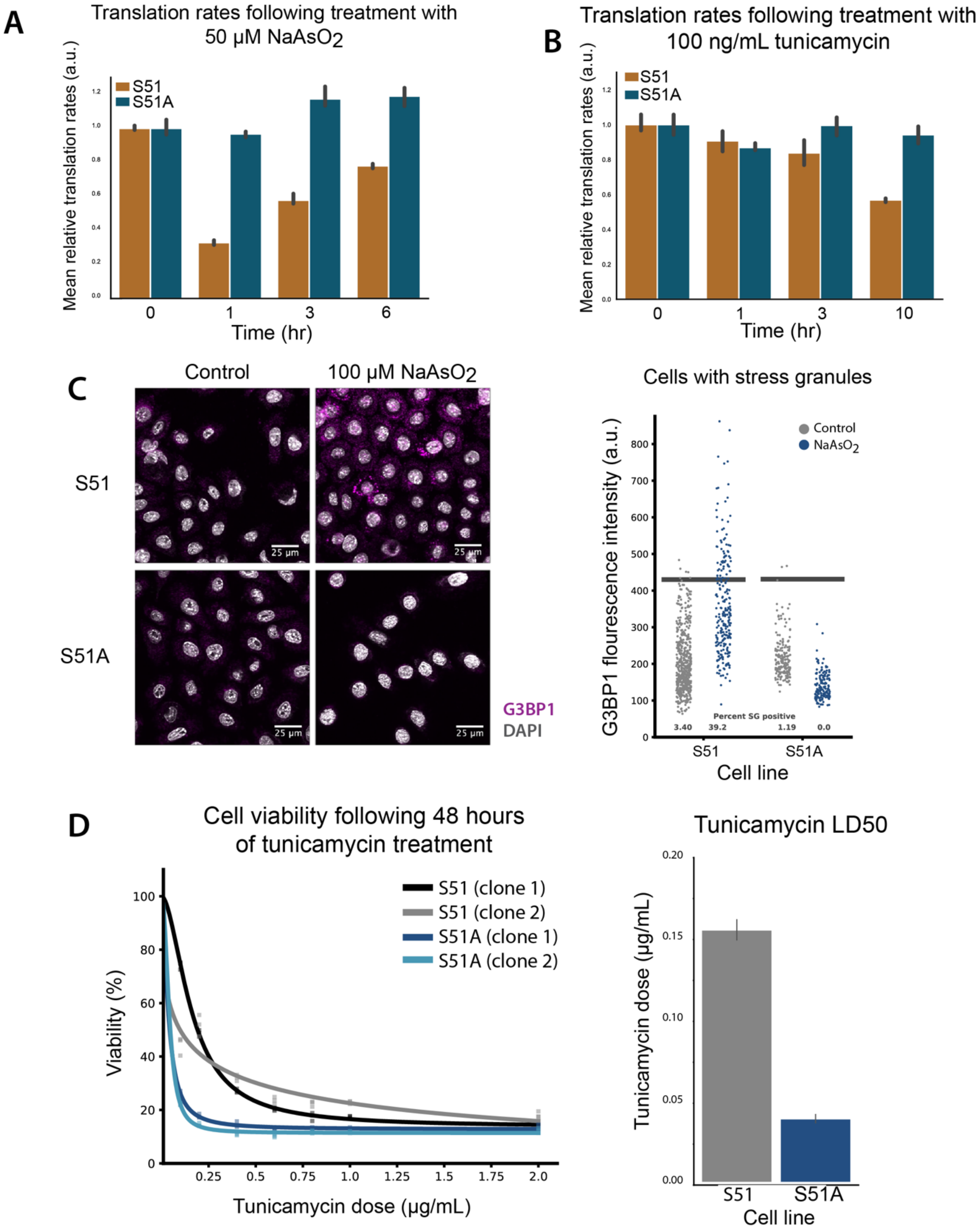

Chapter 2:

Phenotype of ISR-null SCC tumors relative to controls

Part 1 - *In vivo* characterization of ISR-null SCC.

After generating ISR-null SCC cell lines and validating functional loss of the pathway in vitro, I began to characterize tumors formed from these cells *in vivo*. I was most interested in studying how ISR ablation would affect tumor growth, tumor initiation, and tumor histology. To run these experiments tumor cells were grafted intradermally into immunocompromised, athymic nude mice, and tumors were monitored as they formed and progressed. In the first experiment tumor growth was evaluated by simply injecting 100,000 cells per tumor, four tumors per mouse, and tumor volume were measured at various timepoints between 10 and 40 days, when tumors had reached a predetermined size endpoint. Tumor dimensions were measured with an electronic caliper and tumor volume was calculated using the equation, Volume=L*(W^2)(Faustino-Rocha et al., 2013). I was surprised to find that ISR-null SCC cells grew tumors that reached an endpoint at a similar rates to controls (Fig. 2.1 A). Moreover, the ISR-null tumors appeared larger at the earliest timepoints, which suggested that they might even be initiating tumors more efficiently than controls. These effects were consistent across clones.

To assess tumor initiation more directly I turned to a limiting dilution assay. In this experiment tumor cells were serially diluted so that 100000, 10000, 1000, or 100 cells are injected to form single tumors. The assay is based on the idea that within a population of cancer cells only a fraction have tumor initiation capacity (Al-Hajj et al., 2003). As decreasing numbers of cells are grafted the likelihood of a "tumor initiating cell" (TIC) being present in the population of cells grafted decreases, and the fraction of TICs within the population can be estimated from the tumor initiation efficiency across cell numbers (Al-Hajj et al., 2003; Schober & Fuchs, 2011). For each SCC clone and cell number 6-10 tumors were grafted and tumor initiation was confirmed as the presence of a visible SCC in the injected region at any time post grafting. ISR-null cells formed tumors more efficiently at lower cell numbers than controls, with both ISR-null cells forming tumors the majority of the time with as few as 100 cells injected (Fig. 2.1 B). Data was pooled by genotype and TIC frequency was assessed by extreme limiting dilution analysis (Hu & Smyth, 2009), which estimated that one in 604 ISR-null cells had tumor initiation capacity, compared to one in 3025 for controls (Fig. 2.1C).

Figure 2.1: ISR-null SCC cells initiate tumors at lower cell numbers than controls.

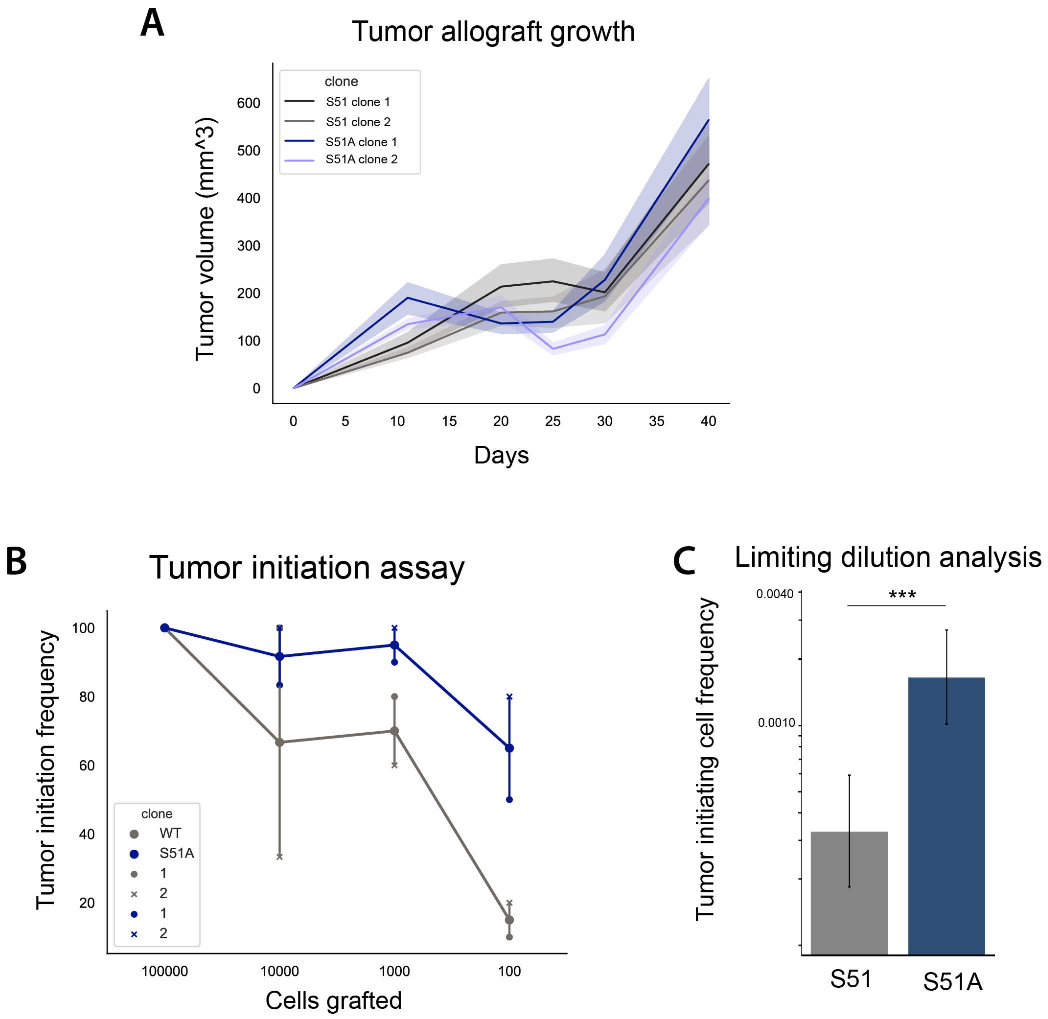

Figure 2.1: ISR-null SCC cells initiate tumors at lower cell numbers than controls.
A. Tumor allograft growth following intradermal injection of 100,000 SCC cells into immunocompromised mice.
B. Limiting dilution/tumor initiation assay. Decreasing SCC cell numbers were grafted intradermally into immunocompromised mice, and tumor initiation was evaluated by visually inspecting for tumor growth at each injection site.
C. Extreme limiting dilution analysis (ELDA) to determine tumor initiating cell frequency. Data was pooled by genotype and analyzed.

I was curious if ISR-null SCC tumors had a different histology at early timepoints compared to controls. I hypothesized that increased efficiency of tumor initiation would correlate to a less differentiated histology. To assess for this histology I collected tumors 10 days after grafting, fixed and froze tumors in cryomolds, and prepared slides by cryosectioning 14 μM sections onto slides. Histology was assessed by performing immunofluorescence on slides for GFP, α6-integrin, and E-cadherin, which mark tumor cells, the stem cells residing in the basal layer, and differentiating suprabasal cells, respectively (Schober & Fuchs, 2011; Tinkle et al., 2004).

Both genotypes formed stratified layers, with basal α6-integrin-positive basal cells residing at the basement membrane and E-cadherin-positive suprabasal cells forming stratified layers that extended apically. I noticed, however, that while control tumors formed comparatively small, circular or tubular structures, the ISR-null cells formed larger, less organized structures of larger diameter. These differences were consistent with the control tumors being in a more well-differentiated, papilloma state compared to the ISR-null tumors appearing less organized and less well differentiated, more similar to an a carcinoma state (Fiore et al., 2020; Schober & Fuchs, 2011) (Fig. 2.2 A). Moreover, intensity of E-cadherin appeared lower in ISR-null cells, suggesting that suprabasal layers possessed a less well-formed network of cadherin-junctions (Fig. 2.2 B).

Figure 2.2: ISR-null tumors appear less differentiated at an early timepoint post grafting.
A. Histology of tumors was assessed 10 days post grafting with immunofluorescence targeting α6-integrin (basal stem cells) and E-cadherin (differentiated suprabasal cells).
B. Quantification of average E-cadherin fluorescence intensity.

Figure 2.2: ISR-null tumors appear less differentiated at an early timepoint post-grafting.

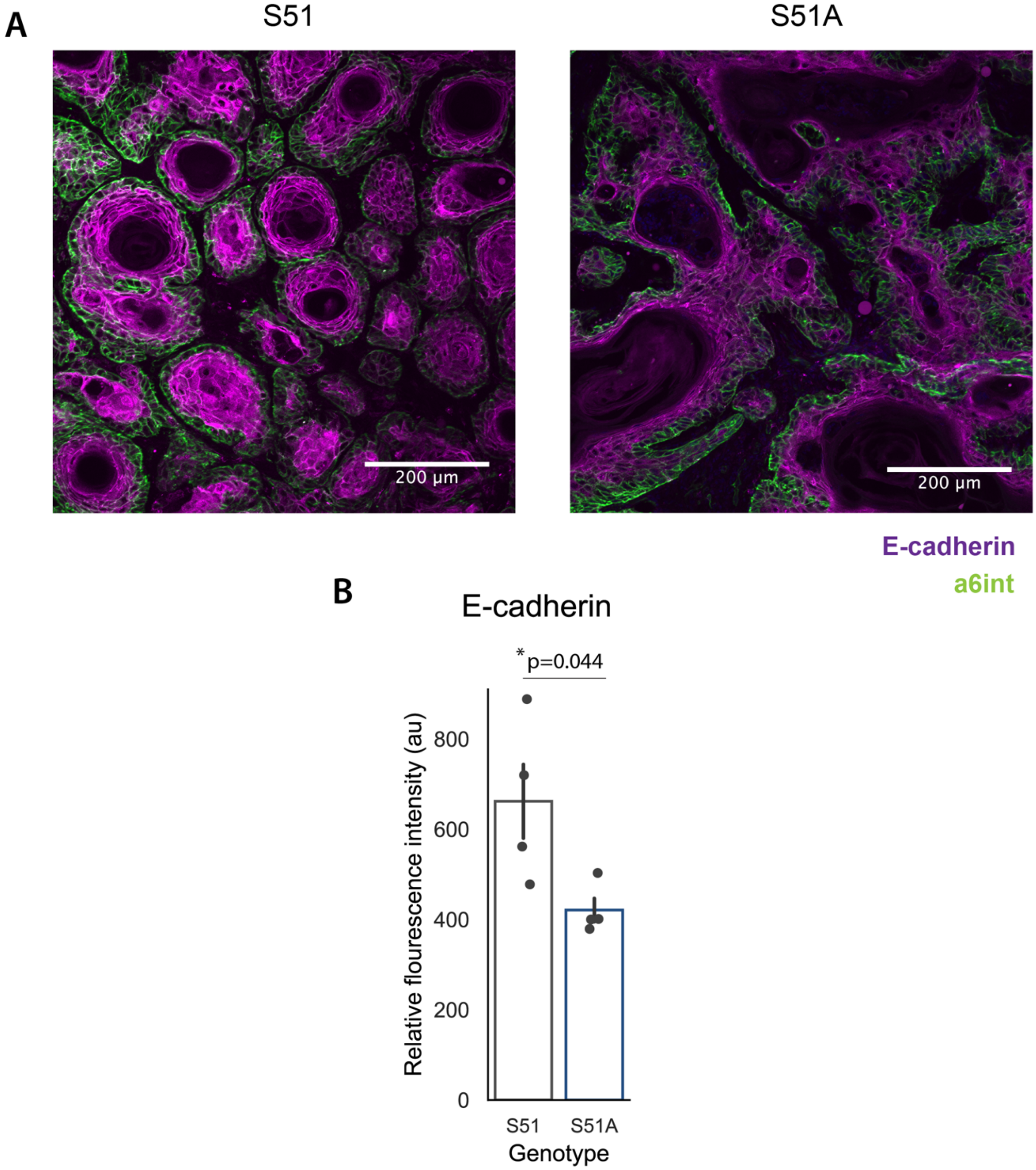

To investigate how histology compared between genotypes at later timepoints I harvested late-stage tumors after 30 days of growth and assessed histology using similar immunofluorescence approaches as well as hematoxylin and eosin (H&E) staining. Unlike at early timepoints, late-stage ISR-null tumors appeared similar to controls, with both genotypes appearing to have progressed to SCCs of an advanced stage. Immunofluorescence for GFP, α6-integrin, and E-cadherin revealed that the organized, stratified structures present at early timepoints had partially broken down, and tumors appeared more like SCCs (Fig. 2.3 A). H&E staining confirmed that tumors formed from the two genotypes had similar histology (Fig 2.3 B).

Figure 2.3: ISR-null tumors and controls have similar morphology at late timepoints.
A. Histology of tumors was assessed 31 days post grafting with immunofluorescence targeting α6-integrin (basal stem cells) and E-cadherin (differentiated suprabasal cells).
B. Histology of day 31 tumors was assessed by hematoxylin and eosin staining.

Figure 2.3: ISR-null tumors and controls have similar morphology at late timepoints.

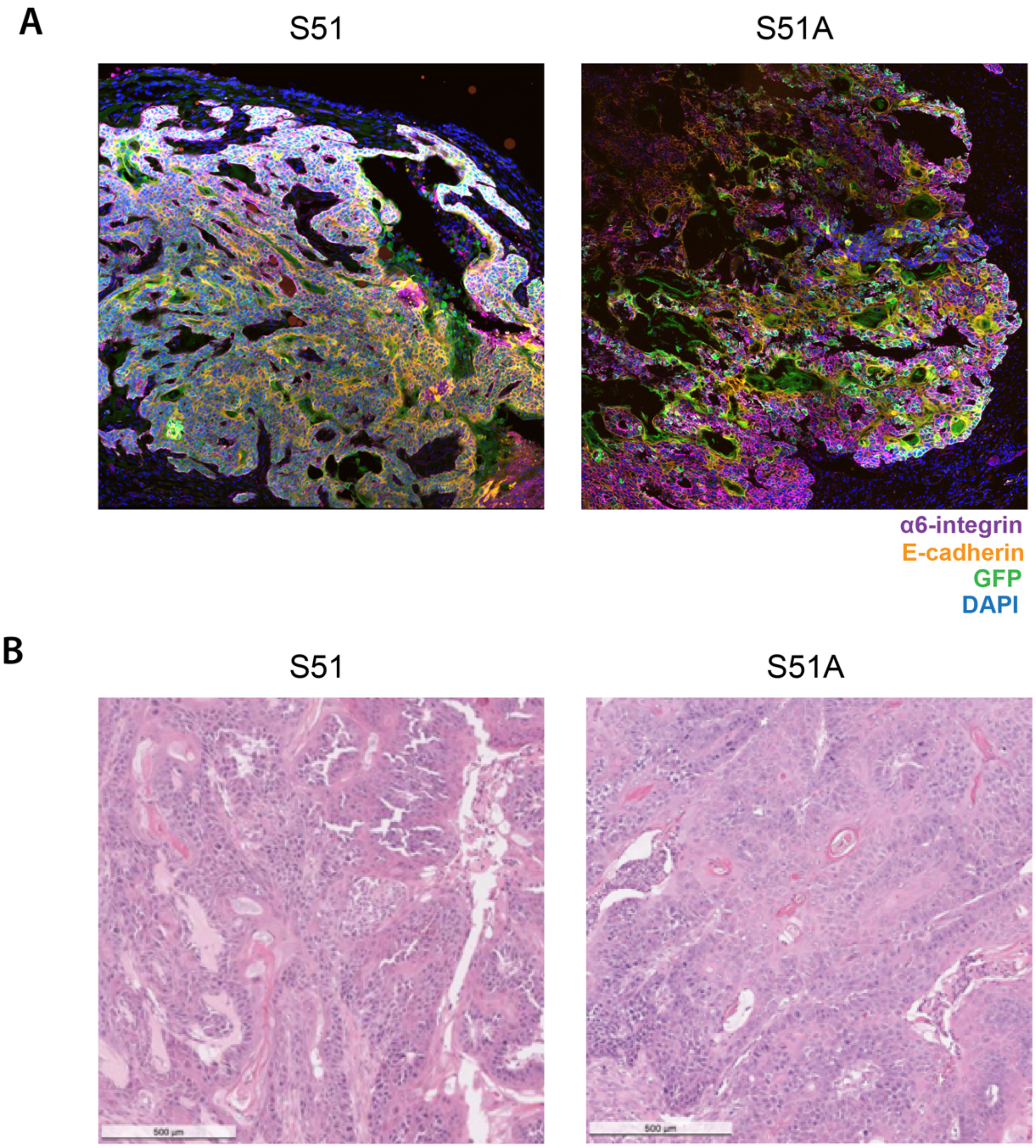

Part 2 - Experiments treating SCCs with ISRIB.

I was next interested in investigating how pharmacologic inhibition of the ISR affected tumor growth. The new drug, ISRIB, offers a promising approach to inhibit the ISR in diverse disease processes (Sidrauski et al., 2013). I tested the effect of ISRIB on the growth of SCC tumors generated from the parental, primary SCC cell line from which ISR-null and control cell lines were generated. ISRIB's potency and favorable safety profile improved the tractability of *in vivo* SCC treatment. On the other hand, the relatively short half-life of ISRIB in vivo and the compound's partial inhibition in cases of high ISR-activation did threaten to complicate interpretation of this experiment (Rabouw et al., 2019; Sidrauski et al., 2013). Despite these concerns ISRIB has been used successfully in a series of experiments treating prostate cancer which demonstrated anticancer activity (Nguyen et al., 2018). With this information in mind I initiated *in vivo* experiments using ISRIB to treat SCCs at two different doses and treatment schedules.

First, I validated the batch of ISRIB's inhibitory effect on ISR function. Treatment with 1 μM ISRIB potently inhibited Atf4 accumulation following 4 hours of 50 μM sodium arsenite treatment. Moreover, ISRIB prevented translational shutdown following sodium arsenite treatment as assessed by op-puromycin fluorescence. These results confirmed that ISRIB has the expected activity in the SCC cells *in vitro*.

I grafted SCC tumors as described above and treated ISRIB using two different doses and treatment schedules. In the first experiment in which I sought to assess tumor initiation and growth, ISRIB was injected intraperitoneally, daily, at a dose of 2.5 mg/kg beginning on the day of grafting. An equal volume of the drug vehicle (DMSO:PEG) was injected into control mice. In this experiment tumors treated with ISRIB grew more slowly than controls, with a statistically significant difference in tumor volumes measured at 18 days. In a follow up experiment, I sought to evaluate the effect of ISRIB on SCC growth once tumors have formed. Out of concern that more ISRIB would be required for an effect on later tumors, and because 2.5 mg/kg of ISRIB was well tolerated, the dose of ISRIB was escalated to 5 mg/kg, and daily injections were initiated 7 days after tumor grafting. In this experiment I found no effect of ISRIB on tumor growth.

Figure 2.4: Effect of daily ISRIB treatment on tumor growth.
A. Western blot targeting p-eIF2α and Atf4 in the presence of sodium arsenite, ISRIB, or the combination.
B. Translation rates measured by OP-puromycin fluorescence following *in vitro* treatment with sodium arsenite, ISRIB, or the combination.
C. Effect of daily ISRIB injections beginning on the day of tumor grafting on tumor growth.
D. Effect of daily ISRIB injections beginning 7 days post grafting on tumor growth.

Figure 2.4: Effect of daily ISRIB treatment on tumor growth.

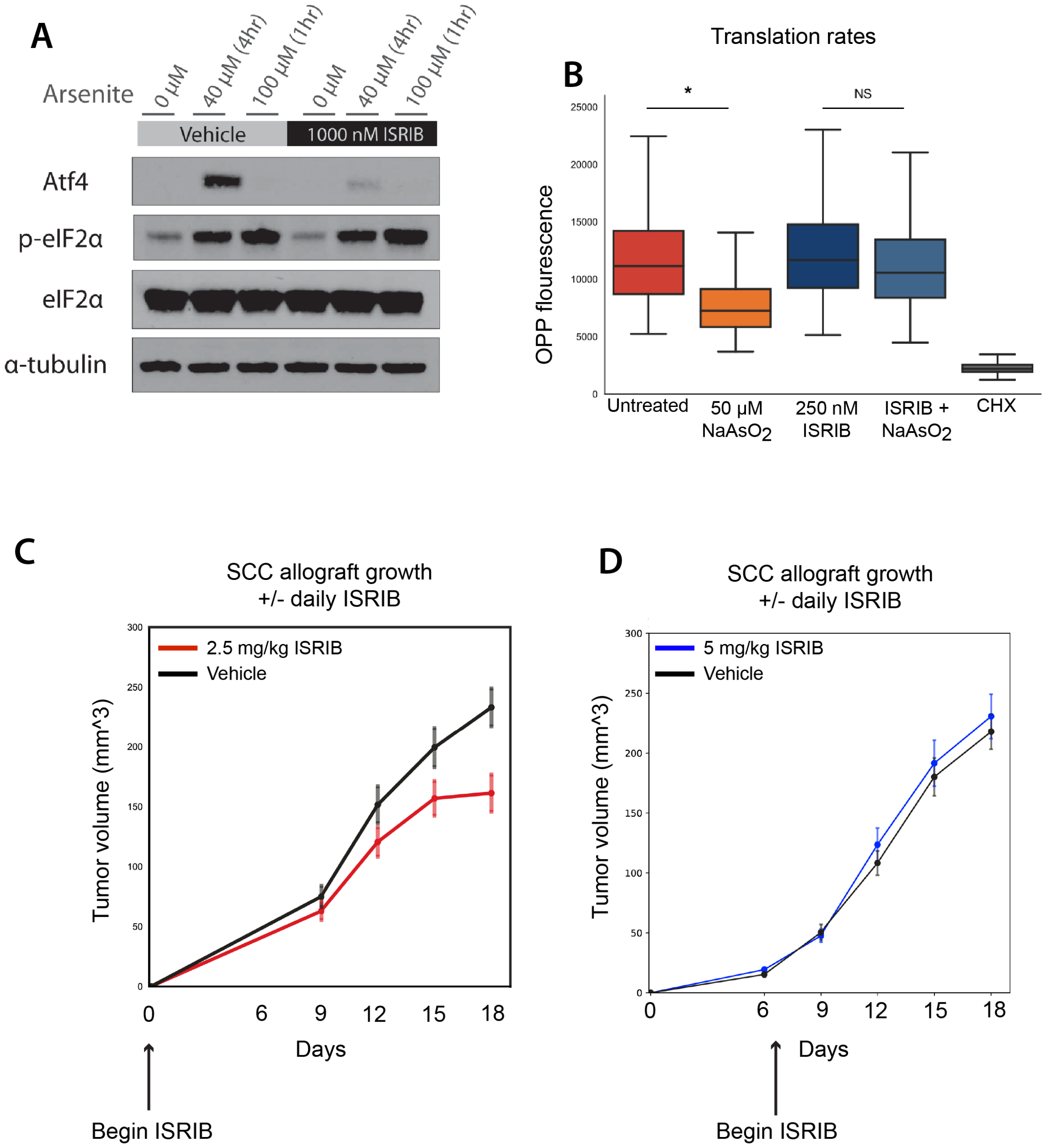

The discrepancy between results suggested that ISRIB exerts an effect primarily at early stages of tumor growth. Perhaps in the first experiment growth was slowed in the first week which set the two groups onto different growth trajectories. I was, however, more puzzled that daily ISRIB treatment affected tumors differently than genetic ISR ablation. In the case of the ISR-null cancers, these lines grafted tumors more efficiently than controls and then groups became equal. In the case of ISRIB treatment, it appeared that treatment with ISRIB slowed tumor growth in a way dependent upon effects shortly after grafting. Perhaps the discrepancy stems from different cellular consequences of complete and chronic ISR inhibition (in the case of genetic ablation) verses partial and potentially intermittent ISR inhibition (in the case of daily ISRIB injections). ISRIB treatment was also systemic and would impact all cells within the mouse, whereas genetic ISR inhibition was specific to SCC cells. Perhaps at early stages of tumor growth ISRIB exerted some non-SCC cell autonomous anticancer effect. At this point I have not further investigated the effect of ISRIB on SCC initiation and growth. With my interest in what could be learned from characterizing ISR-null SCC cells, as well as the difficulty and necessarily short-term nature of experiments requiring daily ISRIB injections, I focused the rest of my studies on the effects of genetic ISR ablation in SCC cells.

Chapter 3:

ISR-null cells have defects in multiple processes mediated by the cytoskeleton

In the course of characterizing the phenotype of ISR-null tumors *in vivo* I recognized changes in the pattern of E-cadherin staining. E-cadherin is a cell-cell adhesion protein that links the actin cytoskeleton of two cells, and in the squamous tissues of normal skin and SCCs it is associated with differentiation (Borghi et al., 2012; Halbleib & Nelson, 2006; Tinkle et al., 2004). A drop in E-cadherin staining could be due to upstream differences in either the cytoskeleton or cellular differentiation pathways. I thus hypothesized that ISR-null cells had an underlying defect in the cytoskeleton. In our lab's experience, cytoskeletal phenotypes can be more dramatic and reliably observed in vitro (Schober et al., 2007; Wu et al., 2008), so I asked if ISR-null and control cells displayed any differences in a suite of *in vitro* assays relying on the cytoskeleton.

Having previously recognized what appeared to be a difference between the cell lines in process of settling onto plates, I performed a cell spreading assay. In this experiment cells are plated onto glass slides coated with fibronectin, and samples are fixed at different timepoints and whether or not they have spread is assessed by immunofluorescence of cytoskeleton markers. Cell spreading on fibronectin is a well characterized process that requires the coordinated action of actomyosin and microtubule networks (Garcin & Straube, 2019; Giannone et al., 2004; Wolfenson et al., 2019). We found that ISR-null cells spread significantly less quickly than controls (Figure 3.1, A). At three hours post plating the majority of control cells had spread, but the ISR-null cells were still mostly not spread. This difference abated by 20 hours post-plating.

Figure 3.1: ISR-null cells spread less quickly than controls when plated on fibronectin.

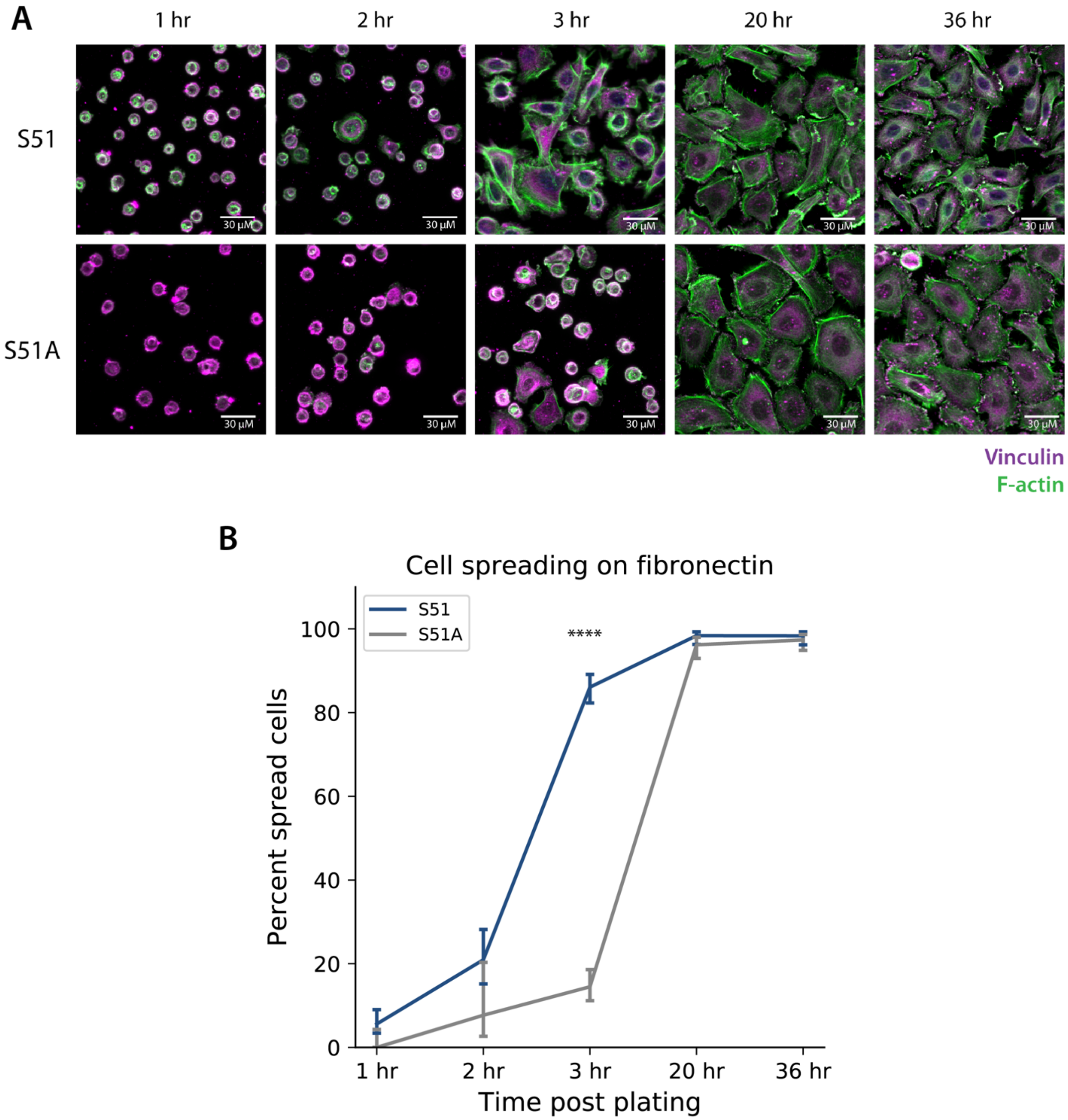

Figure 3.1: ISR-null cells spread less quickly than controls when plated on fibronectin.
A. Cell spreading assessed by immunofluorescence for Vinculin and F-actin (phalloidin).
B. Quantification of percent cells spread by timepoint. Error bars represent 95% confidence intervals and $p<0.0001$.

During the cell spreading experiment I observed a difference in cell morphologies between the cell lines at 20 hours. I hypothesized that in addition to spreading less quickly ISR-null cells were delayed in becoming polarized. A useful marker for cell polarization on glass is phospho-myosin light chain II (p-MyoII), a regulatory subunit of myosin complexes which is phosphorylated by myosin light chain kinase to stimulate actomyosin-dependent contractile forces (Ikebe & Hartshorne, 1985). During polarized migration p-MyoII is induced at the cellular leading edge (Gupton & Waterman-Storer, 2006; Lauffenburger & Horwitz, 1996). When p-MyoII staining was evaluated in the cells at 20 hours post plating, control cells had appropriately polarized, but ISR-null cells appeared to have less clear polarity (Figure 3.2, A). Instead of having restricted regions of p-MyoII at leading edges, ISR-null cells possessed large arcs of p-MyoII signal at multiple regions along the cell periphery. This result in conjunction with the delayed spreading rates of ISR-null cells suggested the presence of a previously undescribed link between the ISR pathway and the cytoskeleton.

Figure 3.2: ISR-null cells polarize less quickly than controls after plating.

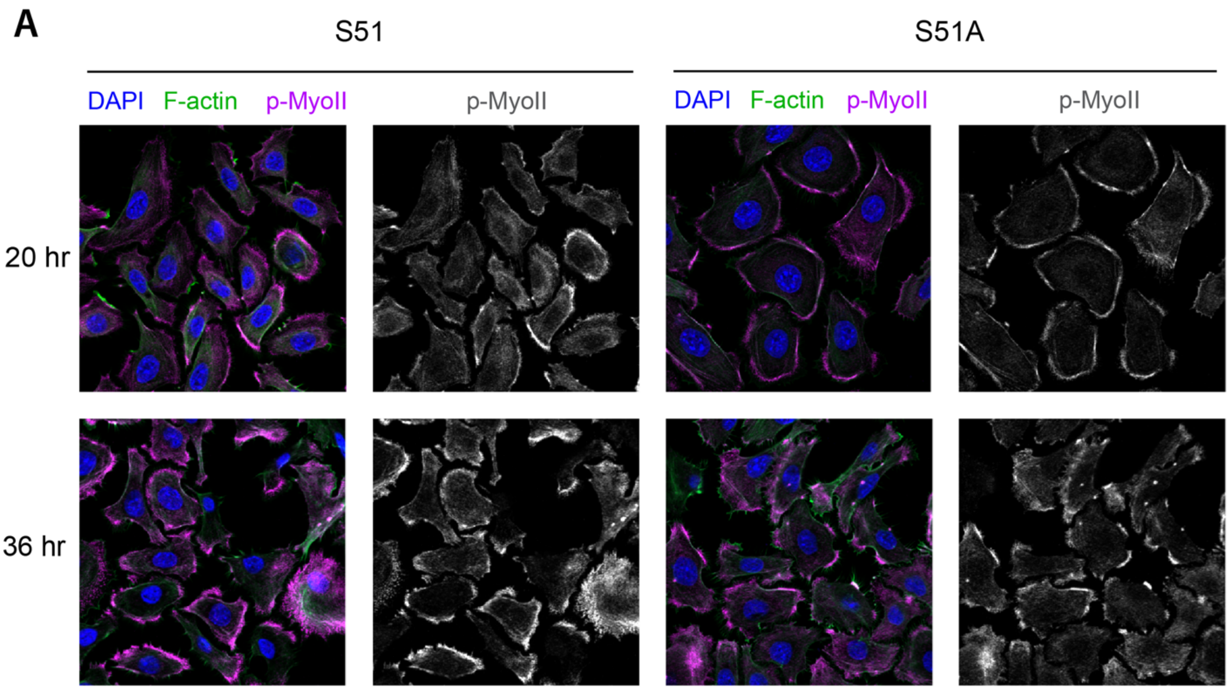

Figure 3.2: ISR-null cells polarize less quickly than controls after plating.
A. Cell polarity assessed by p-MyoII and F-actin immunofluorescence at 20 and 36 hours after plating.

I next asked if ISR-null cells were also defective in the formation of cell-cell adhesions. Cadherin-based cell-cell adhesions require an organized process of adhesion initiation, actomyosin activity, and force-dependent adhesion maturation (Borghi et al., 2012; Buckley et al., 2014). Our lab frequently cultures keratinocytes and SCC cells in low calcium media (50 µM CaCl2), which inhibits the formation of calcium-dependent cadherin junctions. By increasing the concentration of CaCl2 to 1.5 mM, which approximates that of the skin, cadherin junctions are able to form, and cells reorganize the cytoskeleton, decreasing cell-matrix adhesions in favor of cell-cell adhesions (Hennings et al., 1980). Upon calcium addition, control cells joined together, decreased cell-matrix adhesions and the associated stress fibers, and upregulated cortical actin and cell-cell adhesions through E-cadherin. ISR-null cells, on the other hand, joined together but failed to downregulate stress fibers and form an organized network of cell-cell adhesions and cortical actin (Figure 3.3, A). Moreover, the failure to form an epithelial sheet was apparent at the multicellular level, with sheets of ISR-null cells forming long actin fibers that were not clearly associated with single cells (Figure 3.3, B). The inability of ISR-null cells to form cell-cell adhesions *in vitro* further suggests that the different E-cadherin immunofluorescence patterns *in vivo* were due to a primary cytoskeletal process.

Figure 3.3: ISR-null cells fail to form an organized epithelial sheet upon addition of calcium to the media.
A. Timecourse of epithelial sheet formation after calcium switch. Cytoskeletal morphology assessed by immunofluorescence for E-cadherin and F-actin (phalloidin).
B. Zoomed out image to visualize multicellular structure of epithelial sheet.

Figure 3.3: ISR-null cells fail to form an organized epithelial sheet upon addition of calcium to the media.

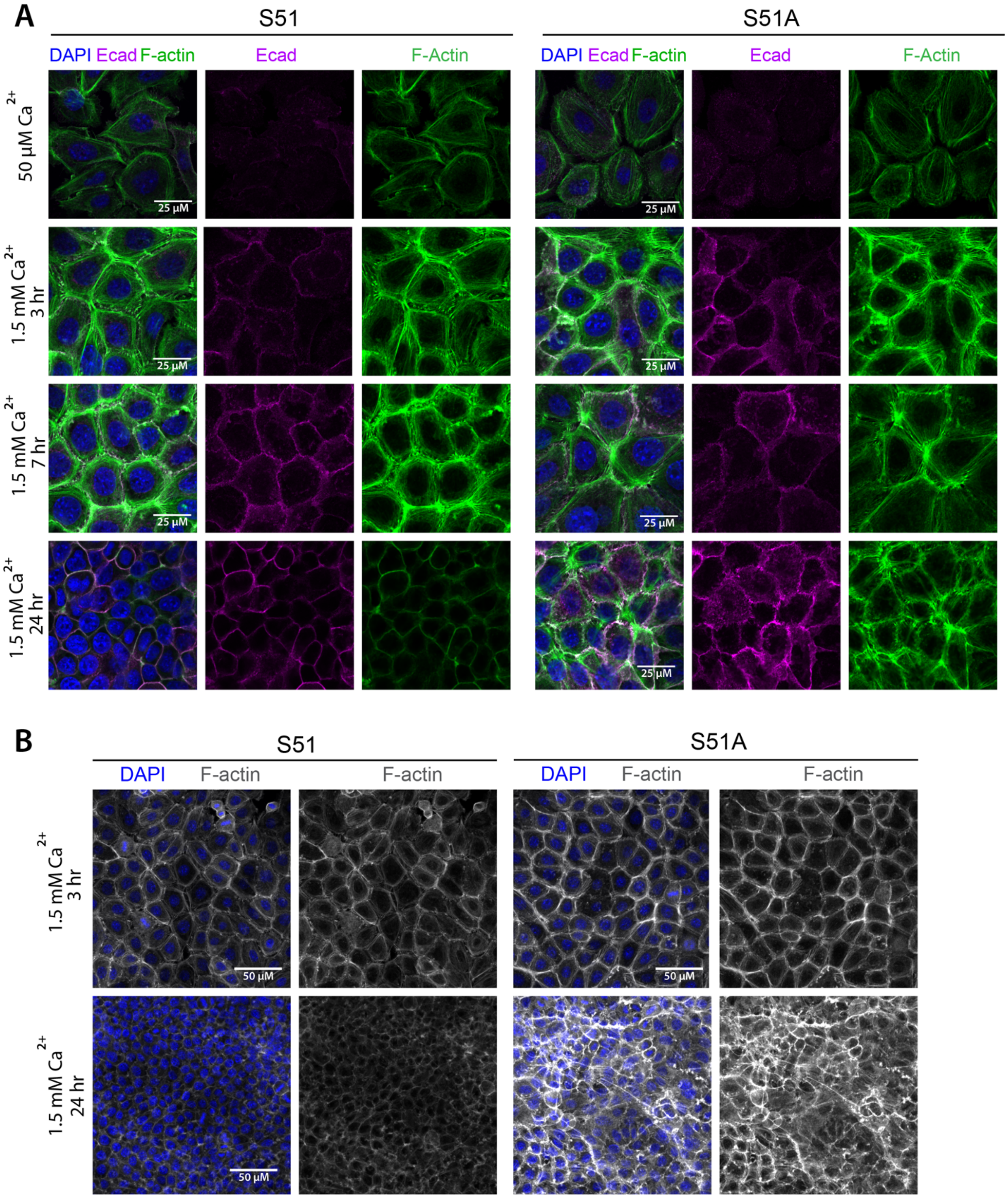

It was surprising to find these morphological differences in the absence of exogenous stress. In order to better understand the link between the ISR and the cytoskeleton I chose to look for cellular stresses that required the ISR and were also associated with changes in morphology that were ISR-dependent. I expected that this strategy could lead to opportunities to discover a mechanism linking these processes while also shedding light on the purpose of the cytoskeleton being under the apparent regulation of a stress-response pathway.

Chapter 4:

Liability of ISR-null SCC cells to proteotoxic stress

Part 1: ISR-null cells cannot clear protein aggregates as quickly as controls.

At this point in the project I had identified some surprising phenotypes of SCC cells lacking the ISR pathway. First, ISR-null SCC cells had an advantage over controls in tumor initiation efficiency, a surprising finding. Additionally interesting was an apparent defect in a handful of cytoskeletally-mediated processes, including cell plating, polarization, and adhesion formation. These effects were, however, subtle in ways. Although ISR-null SCC cells formed tumors more efficiently at low cell numbers, by later timepoints the tumors resembled controls in growth and histology. Similarly, the apparent cytoskeleton defects were only apparent in certain situations. ISR-null and control cells had similar morphology and proliferation rates in growth phase culture. Because the ISR responds to a myriad of stresses in ways that are potentially context specific, I sought to broaden the scope of this work by asking if ISR-null SCC cells were more sensitive to any cancer-relevant treatments or stresses.

One stress, mTOR inhibition, immediately stood out. The mTOR pathway regulates cell growth and translation rates in response to nutrient and growth factor availability (Kim & Guan, 2019; Saxton & Sabatini, 2017). Because this pathway is functionally similar to the ISR, I asked if there was any epistasis between the two pathways that would become evident upon inhibiting mTOR in control and ISR-null cells. I indeed observed a surprising change in cell morphology in ISR-null SCC cells after treatment with two different mTOR inhibitors, rapamycin and torin1 (Heitman et al., 1991; Q. Liu et al., 2012; Sehgal et al., 1975) (Figure 4.1, A). Both inhibitors induced the formation of large, clear vacuoles in ISR-null cells to a much greater extent than in controls (Figure 4.1, B).

Figure 4.1: ISR-null cells accumulate “foamy” vacuoles after mTOR inhibition, a phenotype resembling cells with defective proteostasis.

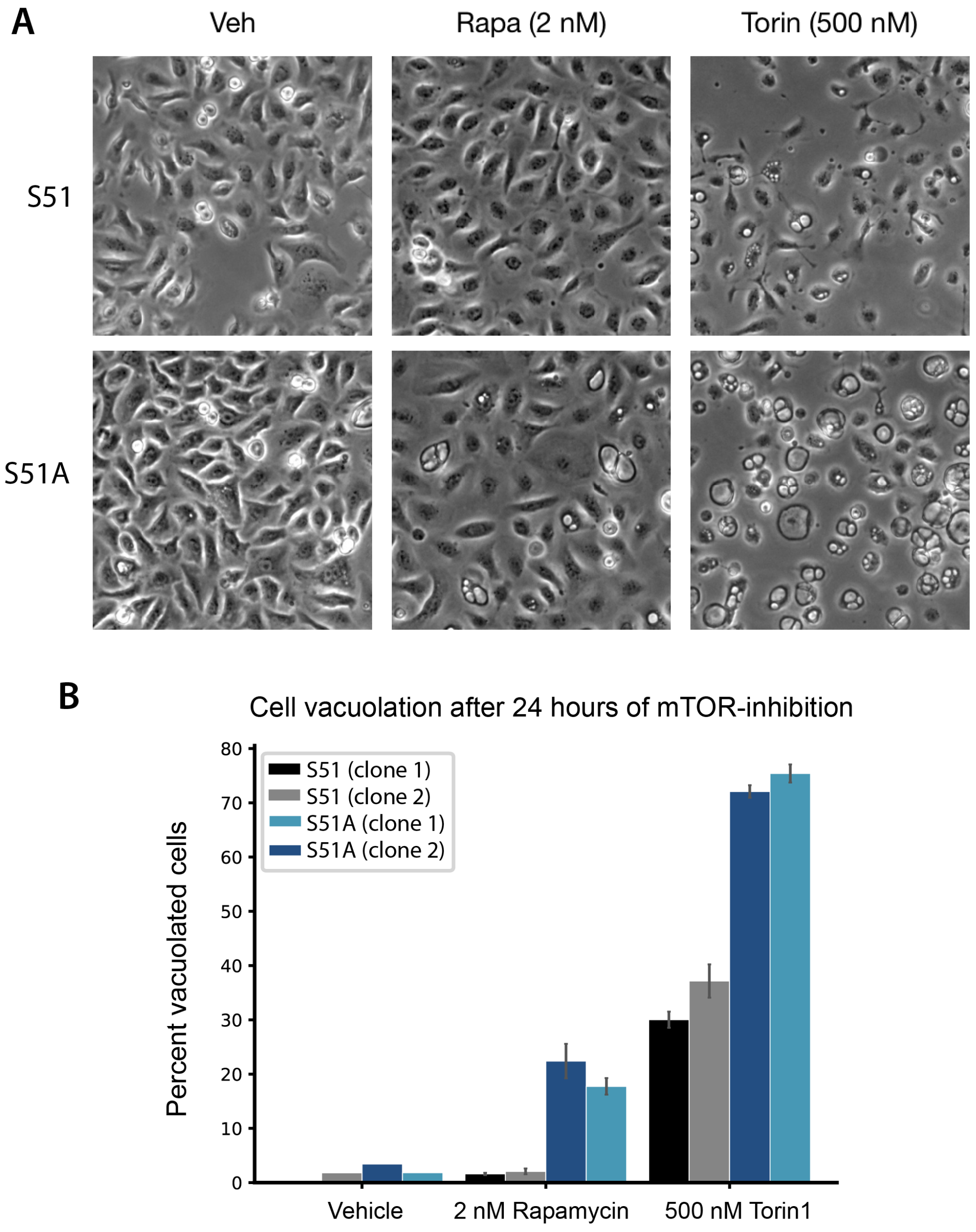

Figure 4.1: ISR-null cells accumulate “foamy” vacuoles after mTOR inhibition, a phenotype resembling cells with defective proteostasis.

A. Cell morphology visualized by brightfield microscopy after 24 hour treatment with either 2 nM rapamycin or 500 nM Torin1.

B. Quantification of the percentage of cells with vacuoles after treatment.

A literature search revealed that similar appearing vacuoles were present in cells with defective clearance of protein aggregates (Armstrong et al., 2001; Mimnaugh et al., 2006; Wojcik et al., 2004; Wong et al., 2000). Such defects in "proteostasis", or protein homeostasis, underly many common and devastating diseases, ranging from Cystic Fibrosis to Parkinson's Disease (Ashraf et al., 2014; Dechecchi et al., 2018; Valastyan & Lindquist, 2014). Moreover, similar vacuoles were found in multisystem proteinopathy, an overlap syndrome of inclusion body myositis, frontotemporal dementia, and amyotrophic lateral sclerosis caused by mutations in genes required for ubiquitin-dependent autophagy (Ching et al., 2013; Nedelsky & Taylor, 2019). Based on this connection plus a recent report that the eIF2α kinase, HRI, senses cytosolic protein aggregates, I hypothesized that the ISR-null SCC cells would be unable to clear protein aggregates induced by proteasome inhibition (Abdel-Nour et al., 2019).

In order to assess the process of protein aggregate clearance I developed a model of recovery after temporary proteasome inhibition. Cells with a saturating dose of the reversible proteasome inhibitor, bortezomib, which I expected to cause the buildup of insoluble, aggregated proteins that would have otherwise been prevented by the ubiquitin-proteasome system (Bence et al., 2001; Meyer & Rape, 2014; Nandi et al., 2006; Paramore & Frantz, 2003). After the drug was washed out of the media, the cells entered a recovery process to eliminate the protein aggregates and recover proteostasis. Importantly, ISR-null and control SCC cells were equally sensitive to chronic proteasome inhibition, suggesting a lack of underlying differences in the response to the drug that would affect the recovery stage (Fig. 4.2, A). However, when cells were challenged to recover after a 6 hour treatment of 100 nM bortezomib, large differences between the cell lines became apparent. Following this bortezomib "pulse", control cells recovered and began to proliferate within 24 to 48 hours. ISR-null cells, however, took a full extra day to begin to proliferate again (Fig. 4.2, B). Moreover, cell morphologies appeared dramatically different during the recovery phase. Unlike control cells which appeared relatively normal, ISR-null cells had clear, cytoplasmic vacuoles that persisted for one day while the cells were not proliferating (Fig. 4.2 C). These vacuoles had similarities to both ISR-null cells treated with mTOR-inhibitors and literature reports of cells with defective proteostasis.

Figure 4.2: ISR-null cells are slower to recover from temporary proteasome inhibition.

A. Cell viability following 24 hours of proteasome inhibition as measured by Cell Titer Glo (Promega).

B. Cell proliferation over 72 hours following a 6 hour pulse of proteasome inhibition.

C. Cell morphology 24 hours after drug wash out.

Figure 4.2: ISR-null cells are slower to recover from temporary proteasome inhibition.

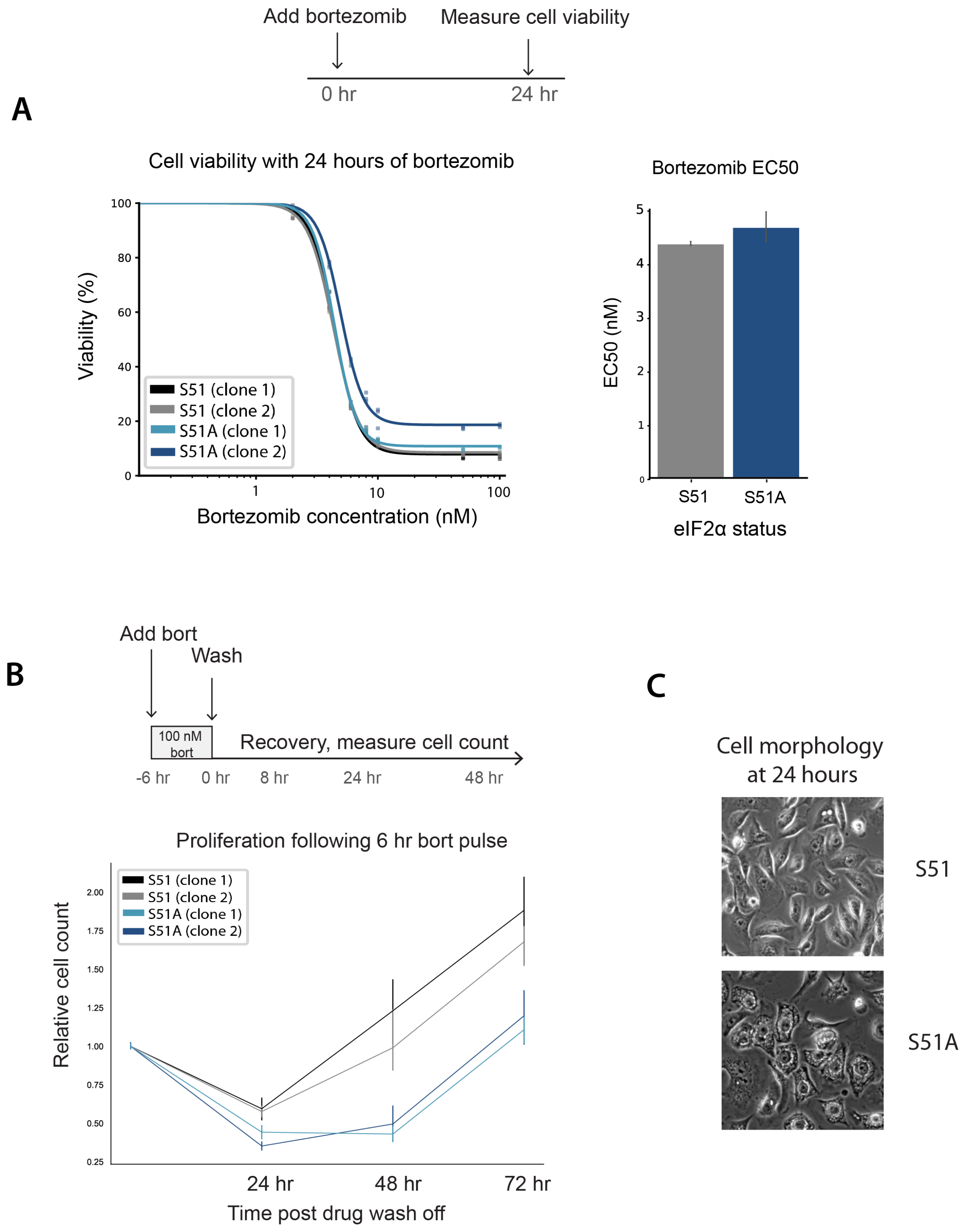

I next sought to follow up on this finding by utilizing cell fractionation to more directly assess the presence of ubiquitinated protein aggregates. This well-established protocol relies on the idea that proteins which are aggregated and insoluble inside the cell will remain insoluble in a detergent buffer after cell lysis (Ochaba et al., 2018). In order to be as stringent as possible, cells were lysed in ionic RIPA (Radioimmunoprecipitation) buffer following bortezomib treatment. Briefly, to fractionate cells into a soluble and insoluble fractions, I lysed cells, gently centrifuged out the membrane fraction, and then subjected the remaining cytosolic fraction to a 30 minute long centrifugation at 20,000 xg. The insoluble pellet was washed in RIPA buffer, spun again, and resuspended by boiling in LDS-buffer with β-mercaptoethanol (Fig. 4.3 A). Both the soluble and insoluble fractions were normalized based on the protein concentration of the soluble fraction and analyzed by an anti-ubiquitin western blot. Treatment with bortezomib not only increased the ubiquitin level in the soluble fraction, but it also caused the clear accumulation of ubiquitin in the insoluble fraction (Fig. 4.3 B).

Figure 4.3: Cell fractionation protocol to analyze ubiquitinated, insoluble protein aggregates.

A. Cell fractionation workflow relying on cell lysis and sequential centrifugation at 4 C.

B. Anti-ubiquitin western blot of soluble and insoluble protein fractions after bortezomib treatment. Protein bound to nitrocellulose membranes visualized by Ponceau stain.

Figure 4.3: Cell fractionation protocol to analyze ubiquitinated, insoluble protein aggregates.

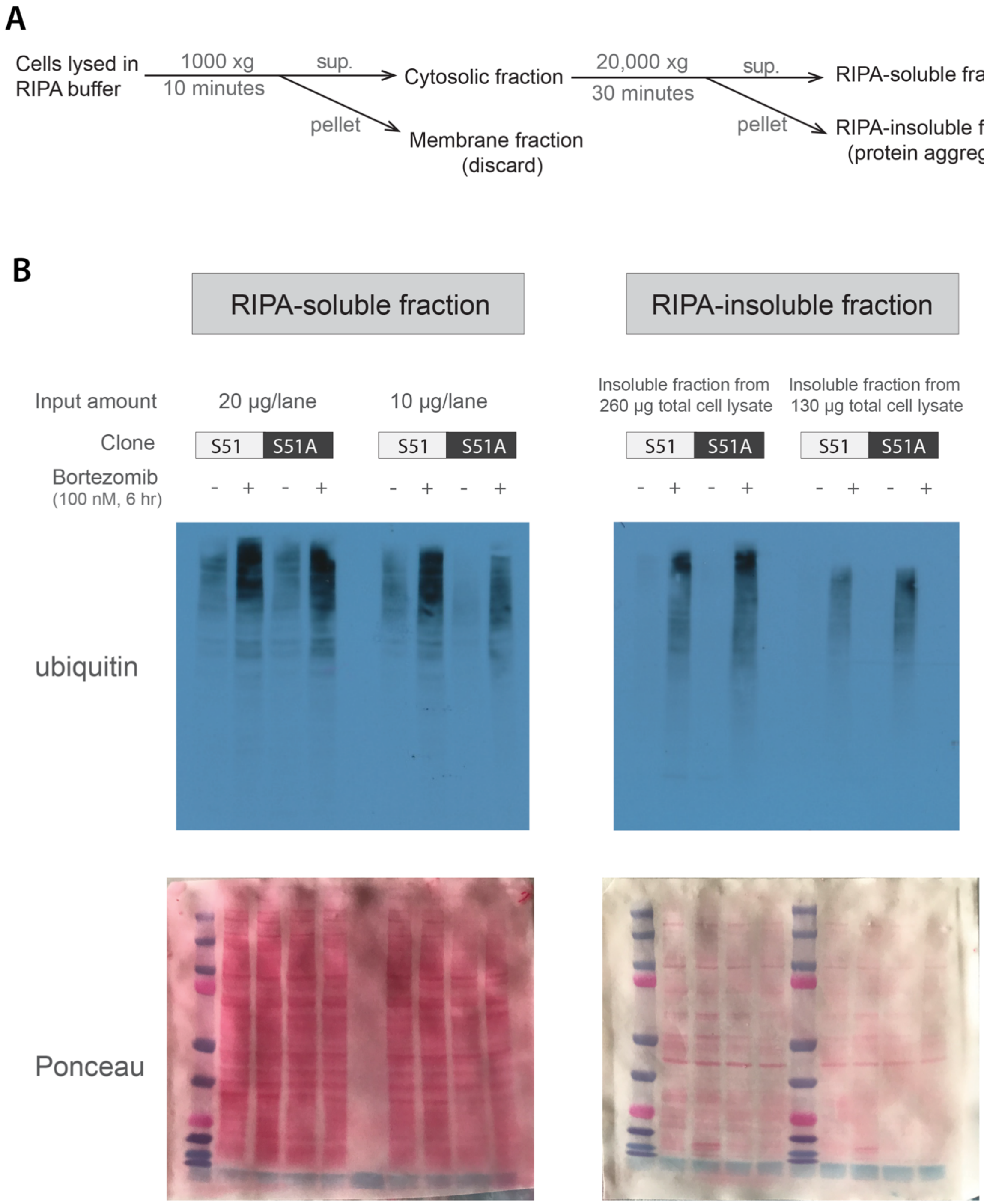

With this assay to analyze protein aggregates validated, I asked if the ISR-null cells were delayed in the ability to clear ubiquitinated aggregates. Consistent with this hypothesis, ISR-null cells still contained ubiquitin signal in the insoluble fraction 24 hours after the bortezomib pulse, a timepoint at which control cells had cleared the aggregates completely (Fig. 4.4 A). The ISR-null cells did, however, clear aggregates by 48 hours, corresponding to the time at which they began to proliferate again (Fig. 4.4 B). In order to confirm that both cell lines were appropriately decorating the aggregates with K-48 linked polyubiquitin, which marks a protein for proteasomal degradation (Thrower et al., 2000), I assessed anti-K48-polyubiquitin binding using the same samples as in Figure 4.4, and I found that the aggregates were positive for K48-linked polyubiquitin (Fig. 4.5). In addition to providing a second antibody to assess the presence of protein aggregates, this result also suggested that the difference in aggregate clearance rates was not due a defective the E3-ubiquitin-ligase system in ISR-null cells.

Figure 4.4: ISR-null cells are delayed in clearing ubiquitinated protein aggregates.
A. Anti-ubiquitin western blot of soluble and insoluble protein fractions from ISR-null and control cells following temporary proteasome inhibition.
B. 48 hour timecourse of anti-ubiquitin western blots of fractionated lysates.

Figure 4.4: ISR-null cells are delayed in clearing ubiquitinated protein aggregates.

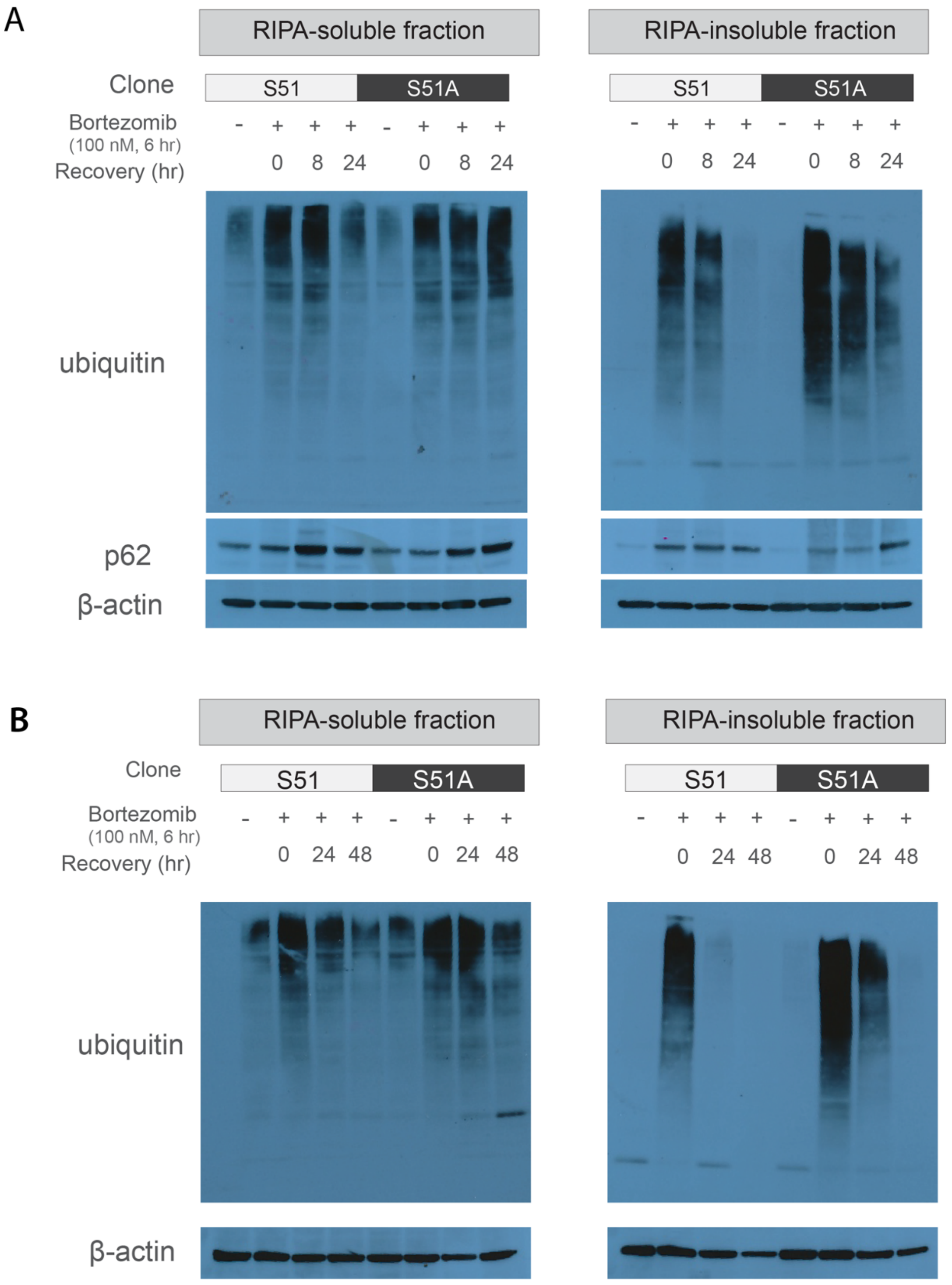

Figure 4.5: Protein aggregates induced by temporary proteasome inhibition are modified by K48-linked polyubiquitin-chains.

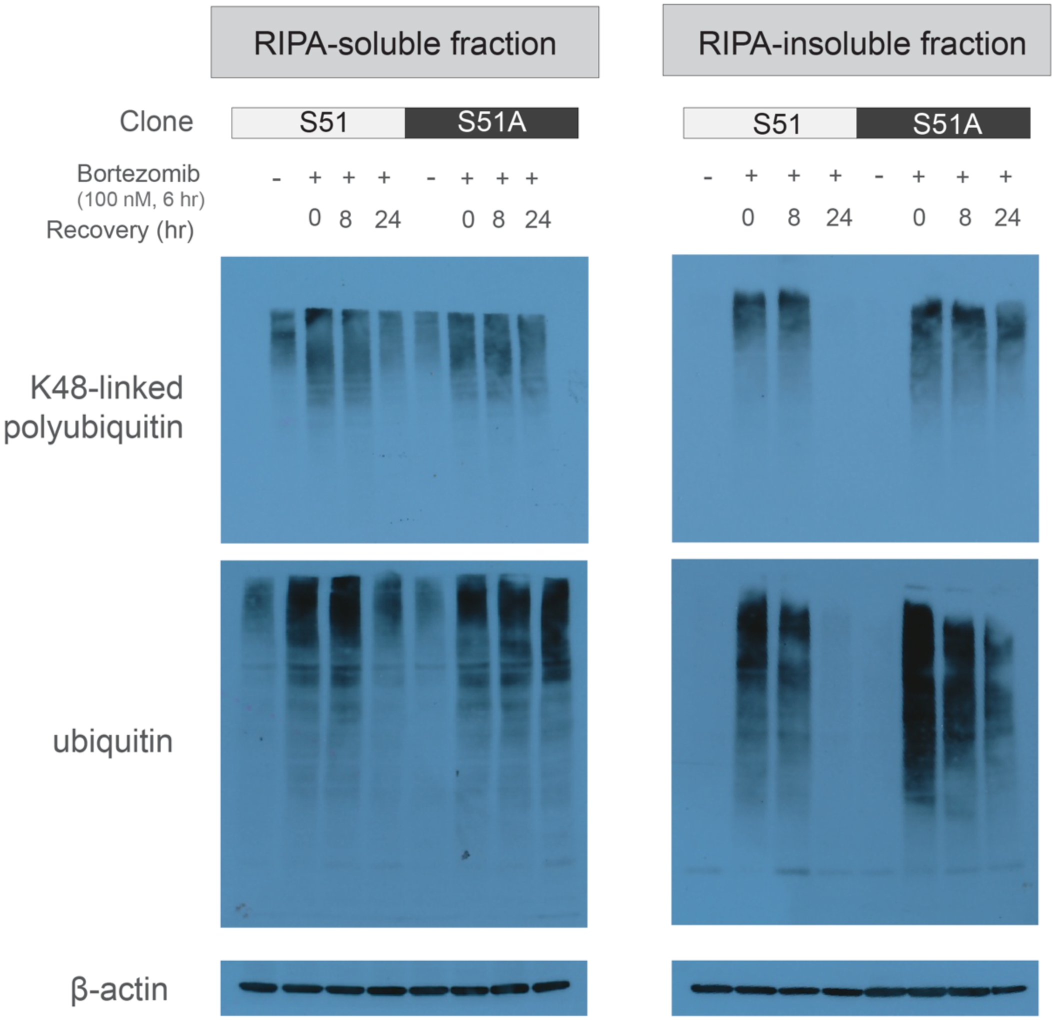

I next asked what upstream eIF2α kinase was responsible for activating the ISR in response to protein aggregates in our cells. I hypothesized that the kinase would be HRI based on a recent report that HRI can be activated by protein aggregates based on an interaction with the chaperone protein, HSPB8 (Abdel-Nour et al., 2019). I had previously generated HRI KO cells, and simply asked if these cells were also defective in clearing protein aggregates. Indeed HRI KO cells did not clear ubiquitinated aggregates from the insoluble fraction as quickly as isogenic controls, suggesting a role for HRI as the relevant upstream kinase (Figure 4.6, A). Curious however was a finding that HRI KO cells did still induce Atf4 following bortezomib treatment (Fig. 4.6, B), which suggested that other eIF2α kinases were acting redundantly and activating the ISR during a proteotoxic challenge. Although I did not follow up on this further, I hypothesized that ISR activation in different subcellular compartments or with different kinetics, as could be the case in HRI KO cells, could lead to the translation of different target genes relevant to proteostasis. A method to evaluate the potential for kinase-specific translational control would be to compare ribosome profiling results from HRI KO cells to ISR-null cells following proteasome inhibition.

Figure 4.6: HRI knockout cells are also defective in clearing ubiquitinated protein aggregates.

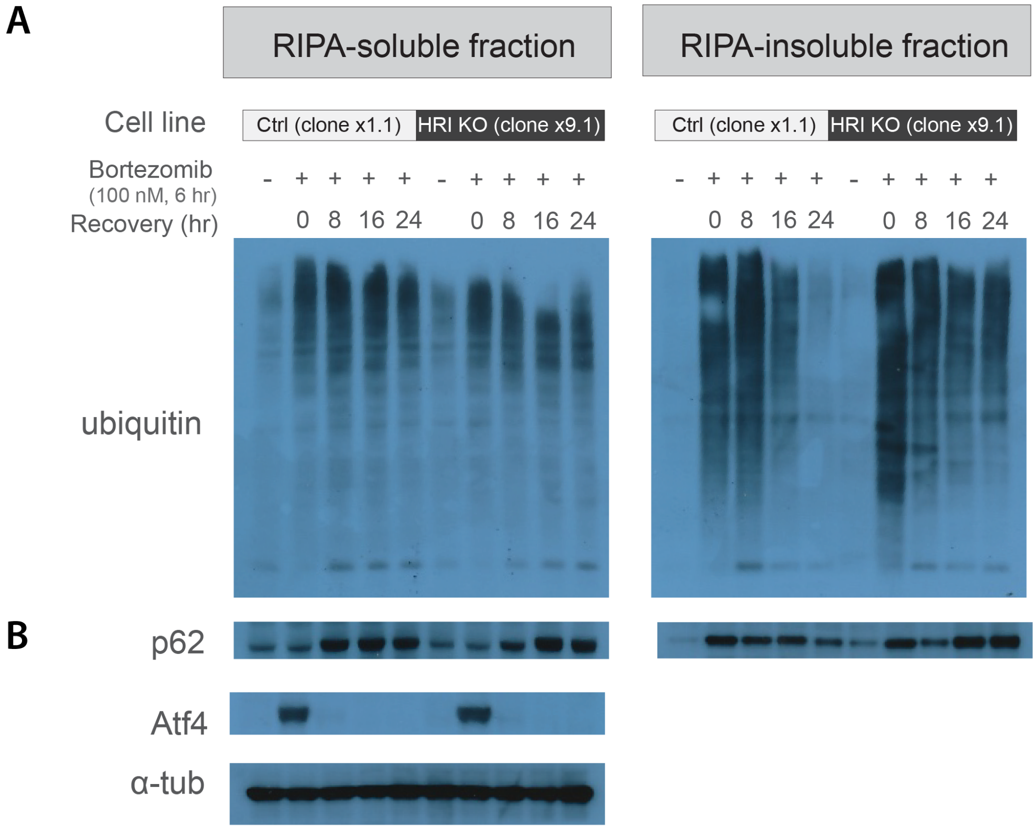

Figure 4.6: HRI knockout cells are also defective in clearing ubiquitinated protein aggregates.
A. Anti-ubiquitin western blot of soluble and insoluble protein fractions from HRI-KO and control cells following temporary proteasome inhibition.
B. Atf4 protein levels from the soluble fraction of HRI-KO and control cells treated with bortezomib.

With this information on the upstream signaling responsible for the ISR-response to proteasome inhibition, I next began an effort to understand the molecular mechanism by which ISR activation was promoting the clearance of protein aggregates. One hypothetical mechanism, a difference in the E3 ubiquitin ligase system, was unlikely due to the appropriate presence of K48-linked polyubiquitin in protein aggregates in both ISR-null and control cell lines (Figure 5). The next step in the process of clearing ubiquitinated proteins is the recognition of these proteins by p62/SQSTM, a ubiquitin binding protein that shuttles protein aggregates to the cell’s two major degradative machineries, the proteasomes and autophagosomes (Bjorkoy et al., 2005; Zaffagnini et al., 2018).

In collaboration with Dr. Vincent Fiore, I assessed the subcellular location of p62 by immunofluorescence and found a surprising difference between the cell lines. Control lines recovering from the bortezomib pulse displayed a dramatic change in the pattern of p62 staining. Between 4 and 8 hours after drug wash out many cells appeared to have shuttled most of the p62 to a perinuclear puncta (Figure 4.7, A). This was consistent with the cells forming an "aggresome" structure. The aggresome is a non-membrane-bound, subcellular compartment containing aggregated proteins, p62, chaperones, and proteasomes, which forms as a cellular response to unfolded proteins as a dedicated site for aggregate breakdown (Johnston et al., 1998; Kopito, 2000). It appeared likely that the control cells were using this process of aggresome formation to clear protein aggregates. The subcellular location of p62 was dramatically different in ISR-null cells. During the recovery process in ISR-null cells, the p62 remained fairly diffuse, with only few cells forming perinuclear puncta (Figure 4.7, A). Moreover the aggresomes that appeared to be present in ISR-null cells were larger and less spherical in shape (Figure 4.7, A). Over the course of the recovery process we observed a decrease, but not complete inhibition, of aggresome formation in ISR-null cells (Figure 4.7, A & B).

Figure 4.7: ISR-null cells are defective in forming the p62-dependent aggresome structures following temporary proteasome inbition.

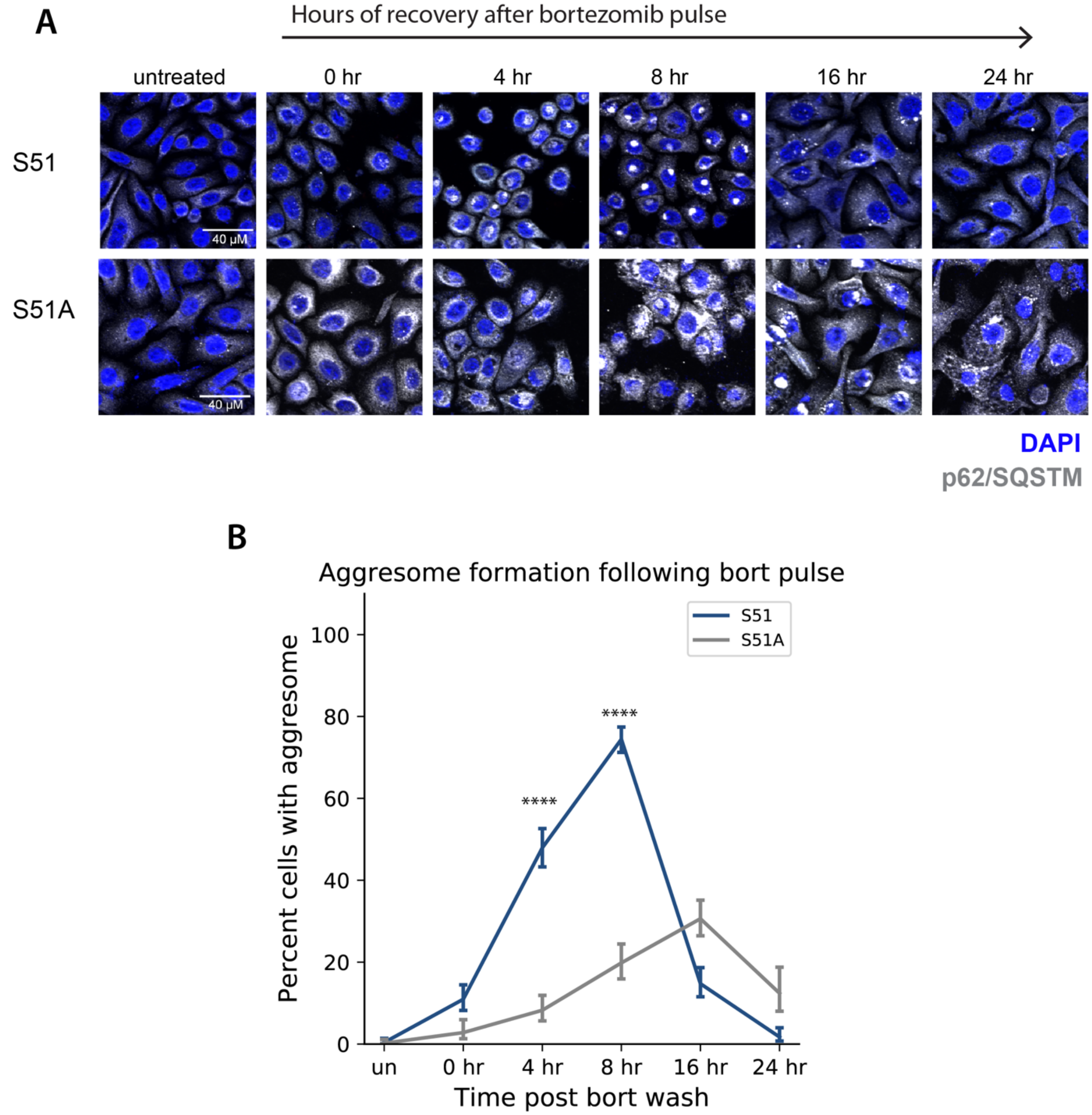

Figure 4.7: ISR-null cells are defective in forming the p62-dependent aggresome following temporary proteasome inhibition.
A. Aggresomes visualized by p62 immunofluorescence during a 24 hour timecourse of recovery from proteasome inhibition.
B. Quantification of the percentage of cells with aggresomes.

I was curious about the nature of the aggresome structure in our cells, so in collaboration with Dr. Amalia Pasolli, director of the Rockefeller University Electron Microscopy core facility, I next performed transmission electron microscopy (TEM) to visualize the aggresomes at the ultrastructural level. The aggresome was clearly apparent in control cell lines as a mass of granules and partially degraded organelles pushing into and deforming the nucleus (Figure 4.8). While ISR-null cells did contain similar granules and degradation products, these structures appeared more diffuse and were not as clearly deforming the nucleus (Figure 4.8). Based on these surprising results I hypothesized that the ISR pathway promoted aggresome formation to clear aggregated proteins, and I next began an investigation into molecular link between these processes.

Figure 4.8: Aggresomes visualized by transmission electron microscopy.

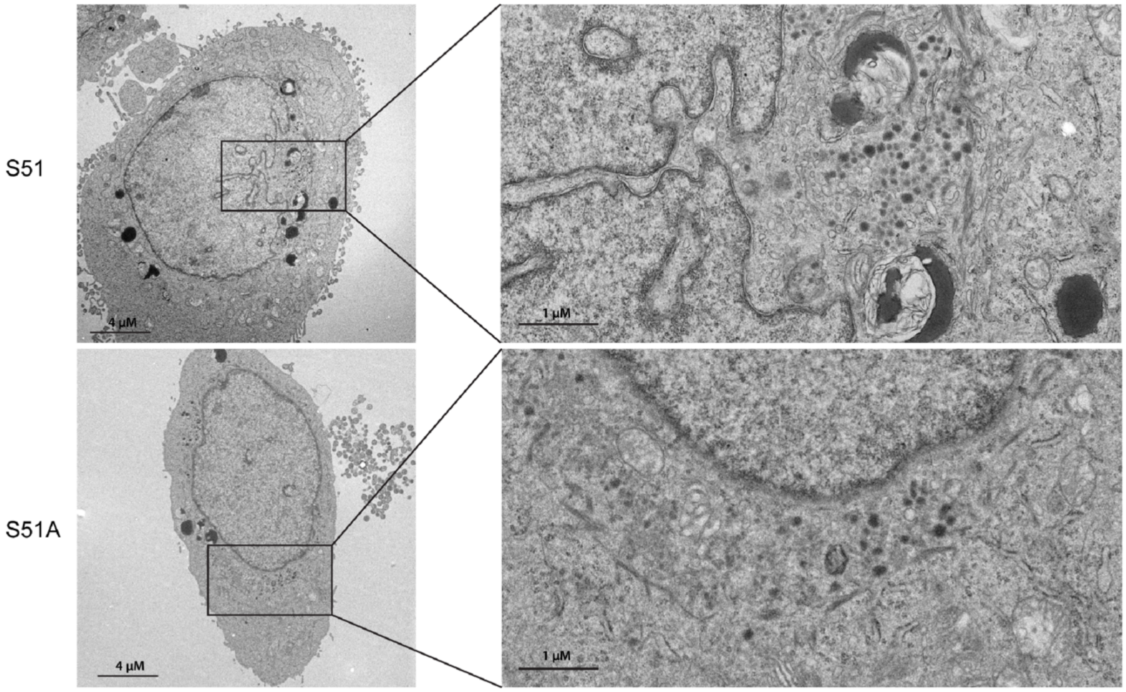

Figure 4.8: Aggresomes visualized by transmission electron microscopy.
Acquired in collaboration with Dr. Amalia Pasolli, director of the Rockefeller University Electron Microscopy Core Facility.

Part 2: Proteotoxic stress induces changes in cell morphology that are ISR-dependent.

During the previous experiments I noticed that control, but not ISR-null, cells went through a dramatic change in cell morphology while recovering from aggregate stress. Specifically, control cells "unspread", becoming more compact and tall between 4 and 8 hours after washing out bortezomib. ISR-null cells, on the other hand, did not similarly unspread, and they instead became flat with some cells possessing elongated processes (Figure 4.9, A). Because this change in cell shape correlated with aggresome formation, a process that requires large-scale intracellular transport, I was interested in further understanding the relationship between cell shape and the recovery of proteostasis.

In collaboration with Dr. Vincent Fiore, I used confocal microscopy to reconstruct the three-dimensional structure of cells recovering from bortezomib, and I observed that many control cells that possessed aggresomes had also become compact (Figure 4.9, B).

I was additionally curious about the appearance of elongated ISR-null cells during aggregate recovery. I recognized that these long processes were reminiscent of the appearance of keratinocytes with a defect in the disassembly of focal adhesions (Kodama et al., 2003; Wu et al., 2008). To force polarized migration in aggregate-stressed cells, I performed a scratch assay immediately following a bortezomib pulse, and analyzed scratch closure and cytoskeletal morphology with immunofluorescence for F-Actin and vinculin (a focal adhesion protein). In line with my hypothesis, ISR-null cells failed to close the scratch, and I observed that the elongated processes of ISR-null cells emanated from large focal adhesions (Figure 9.10, A & B).

Figure 4.9: Recovery of proteostasis correlates with a dramatic change in cell morphology in control but not ISR-null cells.

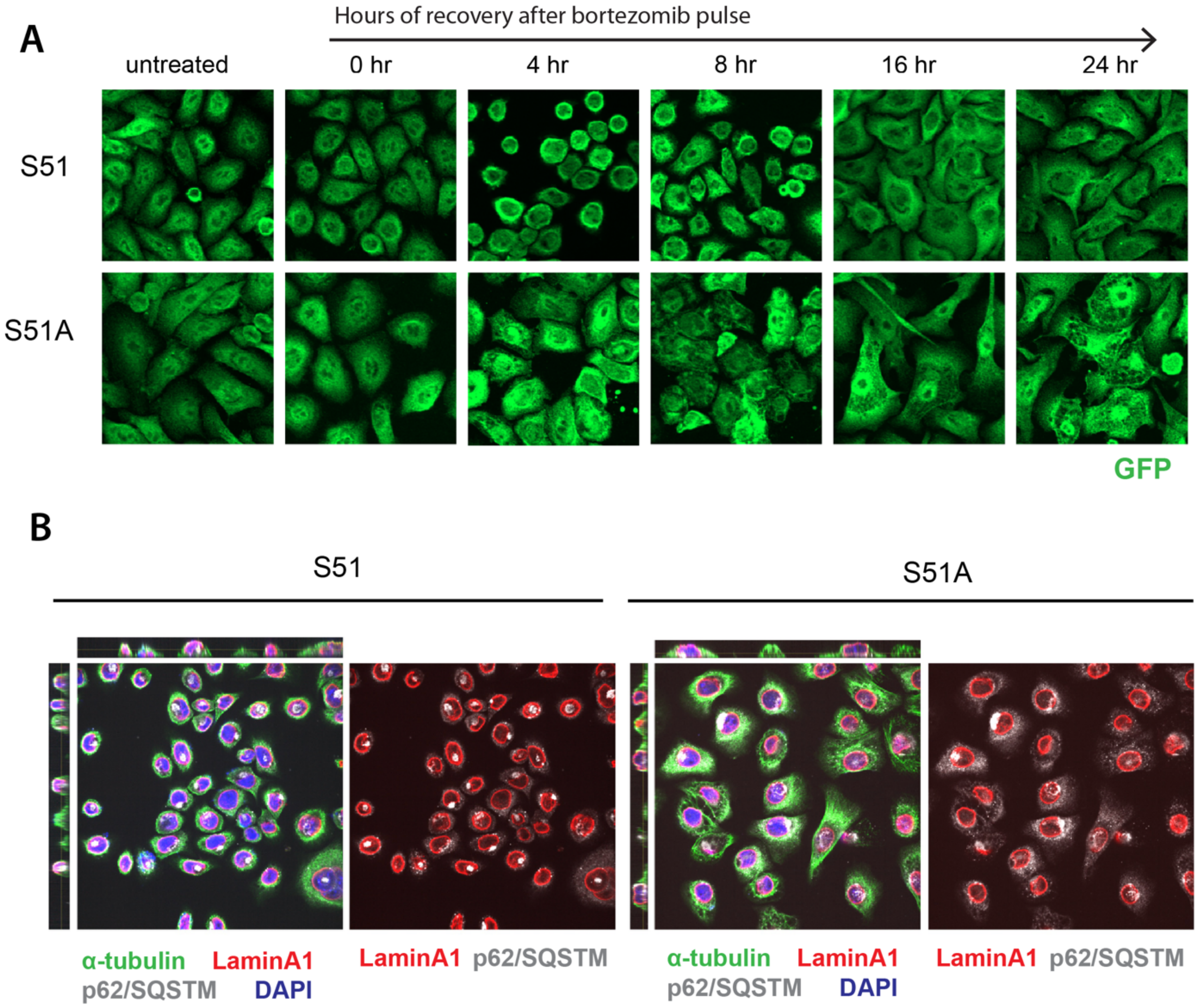

Figure 4.9: Recovery of proteostasis correlates with a dramatic change in cell morphology in control but not ISR-null cells.

A: GFP immunofluorescence of control and ISR-null cells to visualize cell body during recovery of proteostasis.

B: Orthogonal projections of aggresomes, nuclear membrane, and the microtubule cytoskeleton 8 hours after bortezomib pulse.

Figure 4.10: Following proteotoxic challenge ISR-null cells lose the ability to migrate and become elongated with large focal adhesions.

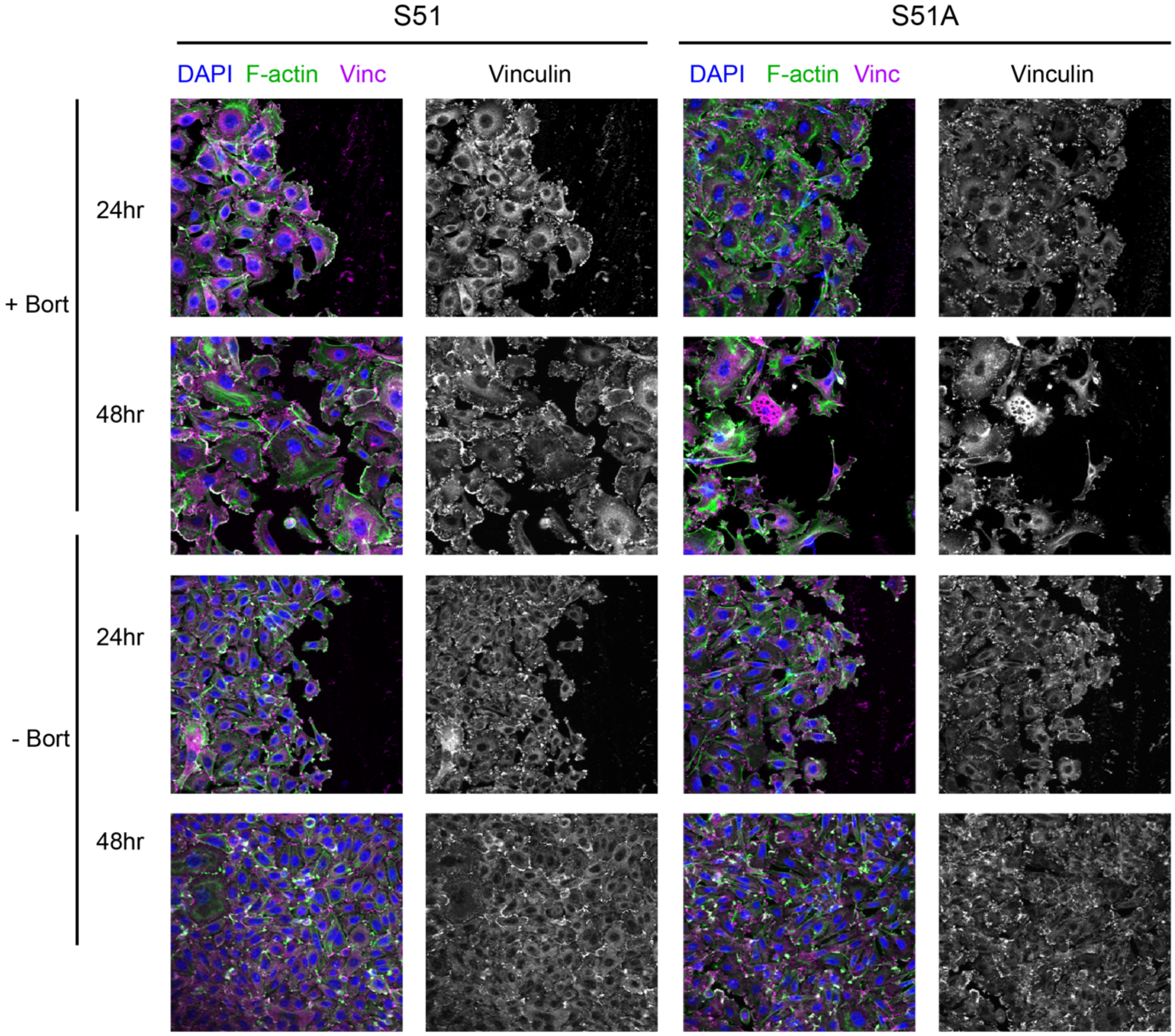

Figure 4.10: Following proteotoxic challenge ISR-null cells lose the ability to migrate and become elongated with large focal adhesions.

A. Cells were scratched following bortezomib pulse, and migration and focal adhesions were visualized with immunofluorescence for F-actin and vinculin.

I was quite intrigued by these major differences in cell morphology that only became apparent during the process of recovery from aggregate stress. Because these seemed to be potentially linked to previously observed differences in some cytoskeletally-mediated processes (chapter 3: cell spreading, polarization, and adhesion formation), I began to narrow my focus on searching for potential roles for the ISR in regulating the cytoskeleton during stress. I was specifically intrigued by the hypothesis that ISR-null cells had a primary defect in cytoskeletal biology, and that the ISR was promoting proteostasis recovery indirectly, by coordinating changes in the cytoskeleton and cell morphology that were required for cells to clear protein aggregates. Because teasing apart cytoskeletal phenotypes is often complicated by tight structural linkage among the actin, microtubules, and intermediate filaments, I next turned to ribosome profiling as a hypothesis generating strategy.

Chapter 5:

The ISR remodels the microtubule organizing center to promote the recovery of proteostasis

At this point in the project I focused on questions related to the mechanism responsible for the cytoskeletal differences arising between control and ISR-null cells during the recovery from proteotoxic stress. Because the ISR regulates the translation of specific target genes during stress (Costa-Mattioli & Walter, 2020; Starck et al., 2016), I hypothesized that differential translation of cytoskeletal regulators could be responsible for the major change in cell morphology following bortezomib treatment. Mammalian cells encode a large number cytoskeletal components and regulators (Alberts, 2015), so I anticipated needing to employ a genome-wide approach to search for ISR-targets that could be responsible for the phenotype.

A relatively new technique, ribosome profiling, was well suited for our use as a hypothesis-generating experiment (Ingolia et al., 2012; Ingolia et al., 2014; Ingolia et al., 2009; Ingolia et al., 2011). This method allows for the quantitative measurement of translation, genome-wide, in multiple conditions and compares the "translational efficiency" of all genes between samples. Ribosome profiling relies on the phenomenon that as ribosomes processively translate protein from an mRNA transcript, the approximately 30 nucleotide mRNA segment that is inside the ribosome at any given time is protected from RNase digestion. Thus, after freezing ribosomes with the translation elongation inhibitor, cyclohexamide, and lysing a population of cells in a lysis buffer that preserves assembled ribosomes on mRNA, an RNase can be added to the cell lysate to digest away all RNA that is not actively bound by ribosomes. The resulting "ribosome protected fragments" or RPFs can be purified by polyacrylamide gel electrophoresis, and prepared for deep sequencing by NGS (more information in methods) (McGlincy & Ingolia, 2017). Total RNA is collected in parallel, is not digested, and is instead prepared for sequencing of total mRNA in the cell. By comparing the number of detected RPFs and traditional mRNA-sequencing reads we would be able to infer, on a genome-wide basis, which genes are being translated into protein most efficiently in the cell (McGlincy & Ingolia, 2017).

I performed ribosome profiling in collaboration with Dr. Nicola Guzzi, and all bioinformatic analyses were performed in collaboration with Drs. Tom Carrol and Doug Barrows in the Rockefeller University Bioinformatics core facility. To set up the experiment, I treated large quantities of control and ISR-null cells with 100 nM bortezomib or vehicle for 4.5 hours, the earliest time point at which morphological differences between cell lines appeared. Cells were then lysed in the presence of cyclohexamide to stall ribosomes, and we proceeded with the ribosome profiling protocol (Figure 5.1). At the end of the of the protocol we had successfully purified, amplified, and prepared both RPFs and total mRNA for Illumina sequencing.

Figure 5.1: Ribosome profiling workflow and experimental design.

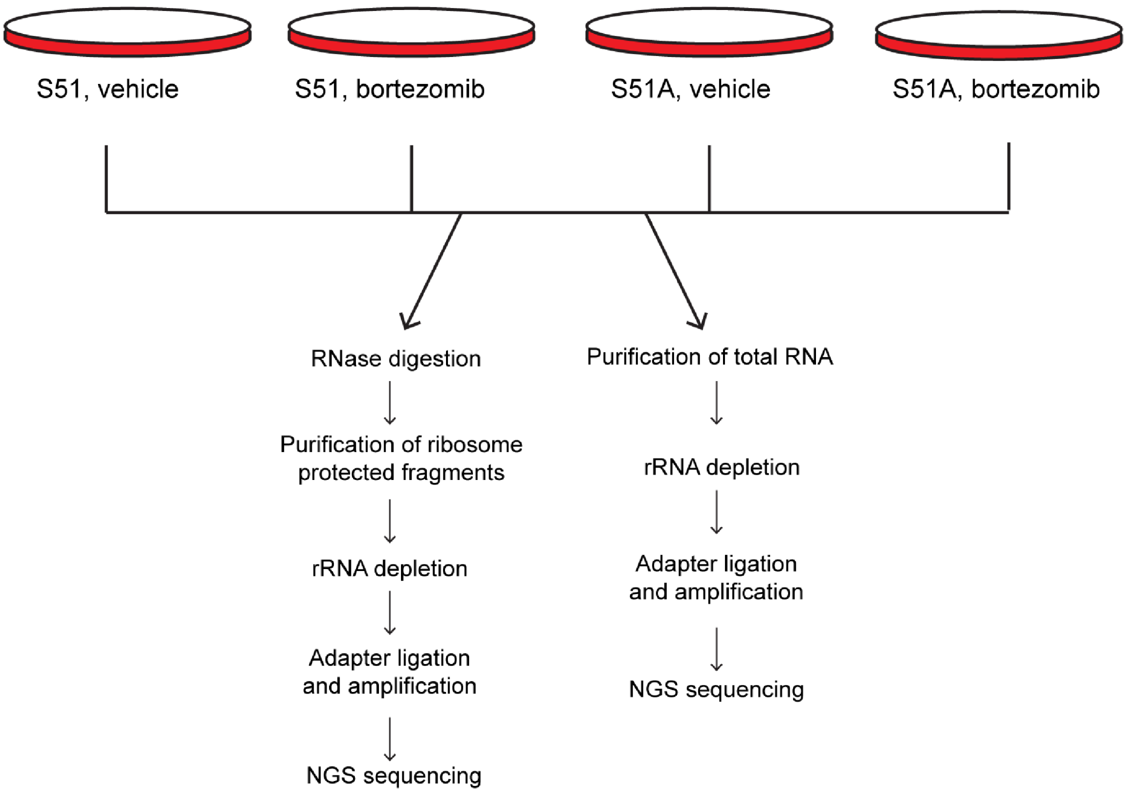

Reads were aligned to the mouse reference genome, and quality control was performed to confirm that we had successfully purified and sequenced RNA fragments protected by translating ribosomes. Technical replicates were found to co-vary within samples using principal component analysis (Love et al., 2014). Reassuringly, experimental replicates clustered tightly, but the two genotypes and conditions clearly differed (Figure 5.2, A). As a second quality control metagene analysis was performed to ask where RPFs were located on transcripts (McGlincy & Ingolia, 2017). As we would expect for a dataset containing primarily translating ribosomes, the majority of RPFs were found within the coding segment, or CDS, with relative peaks at the translation start and stop sites (Figure 5.2, B). This pattern is due to the time taken for ribosomes to assemble and disassemble and is expected in a high-quality ribosome profiling dataset. Read length of RPFs was also evaluated. The read lengths peaked between 29 and 32 nucleotides, which corresponds to the correct length of mRNA protected by ribosomes from RNase digestion (Figure 5.2, C).

Figure 5.2: Quality control for ribosome profiling samples.
A. Principal component analysis for RPFs aligned to a mouse refence genome and counted in bins corresponding to 5' UTRs, coding sequences, and 3' UTRs on the annotated transcriptome.
B. Metagene analysis to evaluate the position of RPFs on a typical transcript. TSS=start codon and TES=stop codon.
C. Density plot of the length of aligned RPFs and codon phasing for each read length compared across samples. Analyses in this figure were performed in collaboration with Drs. Tom Carroll and Doug Barrows in the Rockefeller University Bioinformatics facility.

Figure 5.2: Quality control for ribosome profiling samples.

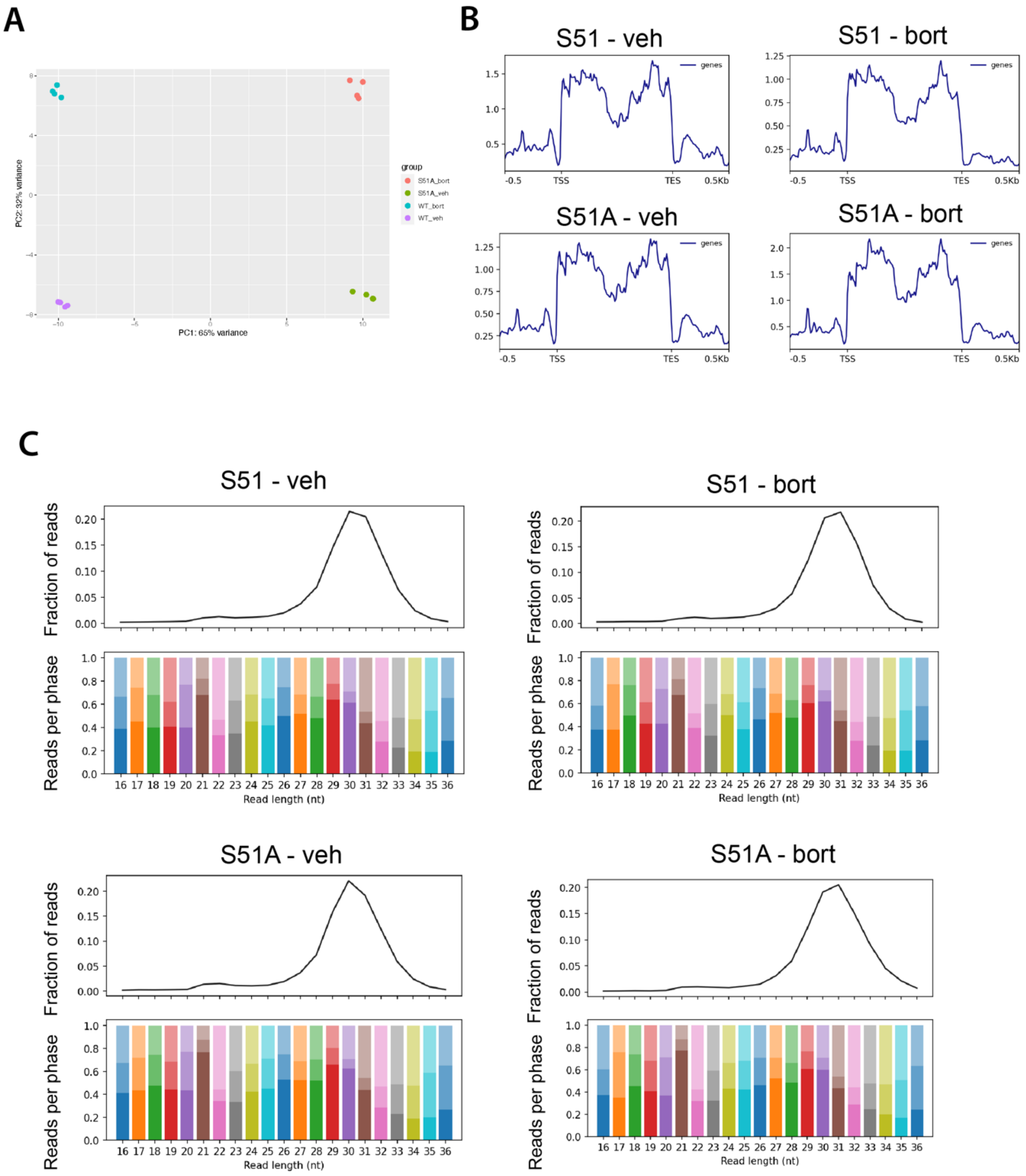

Confident that the dataset was of high enough quality to proceed with analysis, genome-wide changes in translational efficiency were analyzed. The translational changes were determined by differential counting of RPFs for each gene, and mRNA levels were similarly compared by counting mRNA reads for each gene. With these parameters calculated genome wide for each sample, comparisons were made between conditions. Four comparisons were made with the intention of selecting genes that were significantly changed at the translational level for further analysis. I compared vehicle treated control and ISR-null cells (Figure 5.3, A), control cells treated with or without bortezomib (Figure 5.3, B), ISR-null cells treated with or without bortezomib (Figure 5.3, C), and bortezomib treated control or ISR-null cells (Figure 5.3, D). I filtered for genes having an RPF fold change between conditions greater than 1.5 in either direction and a p-value adjusted for multiple hypothesis testing less than 0.05, and these genes were colored in red and saved for further analysis and "differentially translated".

A gene could be differentially translated either because there are more translating ribosomes on each mRNA molecule, or because there are more mRNA molecules but proportionally similar translating ribosomes per molecule. Although this is assessed more directly and quantitatively with "translational efficiency" analysis, simply visualizing the data as in Figure 5.3, A-D can begin to provide insights to translational changes between each sample. For example, although there were differentially translated transcripts between vehicle treated control and ISR-null cells (Figure 5.3, A), translational differences correlated closely to mRNA level differences for each gene, as evident by the relatively tighter linear relationship between the two measures. In the bortezomib verses vehicle treated control cells, however, a different relationship between translation and mRNA levels is clearly present (Figure 5.3, B). The partial loss of the linear relationship suggested that in this comparison translation levels were changing independently of mRNA levels, which would be expected if a cellular translational control pathway had become activated. Interestingly, the same thing was seen in bortezomib verses vehicle treated ISR-null cells, albeit to a lesser extent (Figure 5.3, C). This suggests that some other translational control pathways, mTOR perhaps, were changing and regulating translation, but the changes were not as dramatic as in cells with an intact ISR.

Figure 5.3: Visualizing translation and transcriptional changes between genotypes and treatments.
A. Plot of fold change (S51-vehicle vs. S51A-vehicle) of total mRNA reads (x axis) and RPF counts (y axis).
B. Same as in A. but for the comparison of S51-bortezomib vs. S51-vehicle.
C. Same as in A. but for the comparison of S51A-bortezomib vs. S51A-vehicle.
D. Same as in A. but for the comparison of S51-bortezomib vs. S51A-bortezomib.

Figure 5.3: Visualizing translational and transcriptional changes between genotypes and treatments.

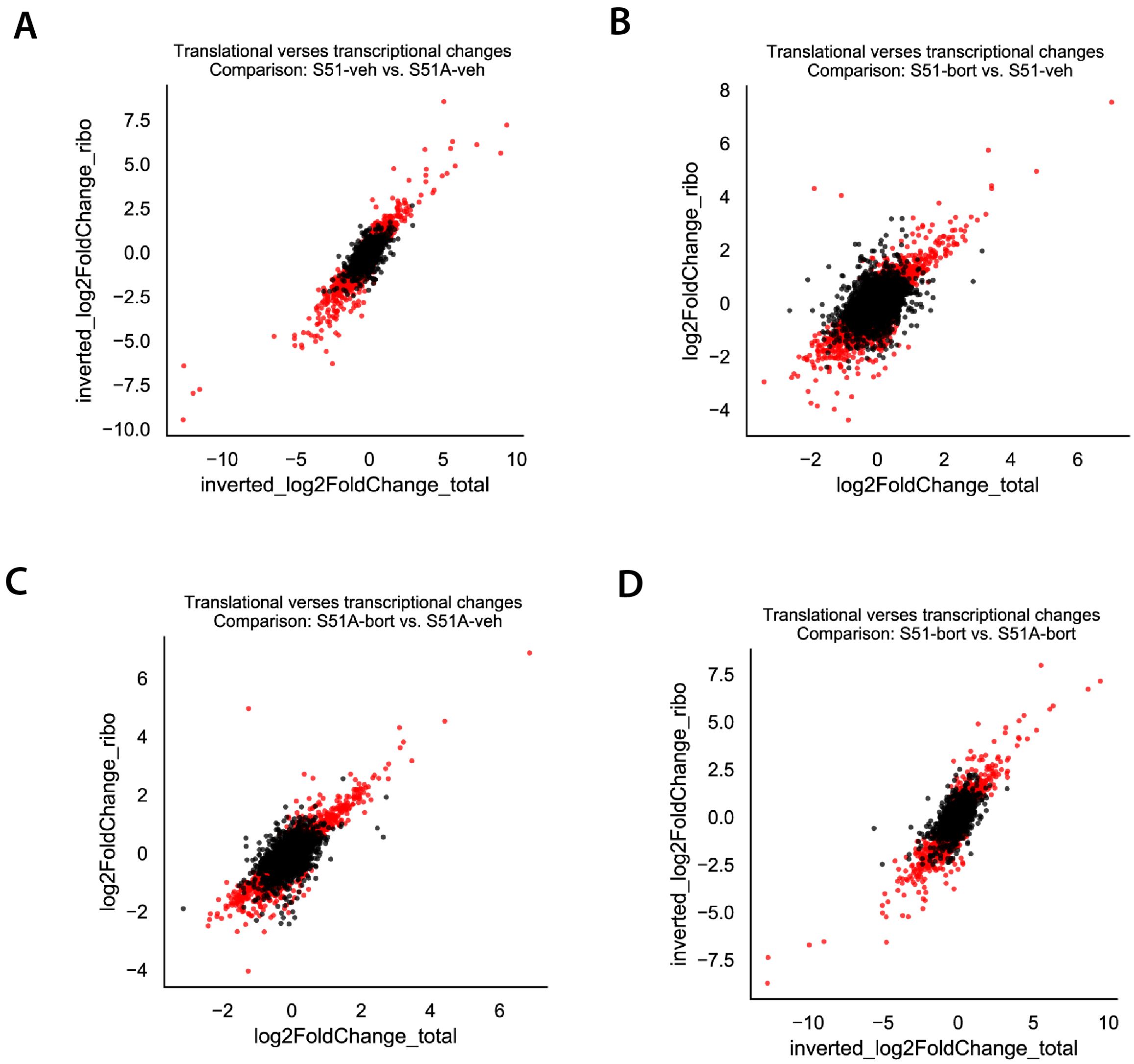

Next, differential translational efficiency analysis was assessed to identify which genes change in their translation in response to ISR-activity during proteotoxic stress. Translational efficiency is calculated by quantifying RPF reads for each transcript normalized to total mRNA levels (TE=RPF/mRNA) (Ingolia et al., 2009; McGlincy & Ingolia, 2017). I sought to curate a list of translational ISR-targets by finding the genes for which TE changed in response to bortezomib *only in cells with an intact ISR*. This analysis took advantage of the lack of TE differences in vehicle treated control and ISR-null cells, and further analyses focused on two comparisons, (A) S51 cells treated with or without bortezomib, and (B) bortezomib treated S51 and S51A cells. Our ideal ISR-target would (A) change in response to bortezomib in S51 cells and (B) would also be measured as differentially translated in bortezomib treated S51 vs. bortezomib treated S51A cells. Put another way, an ISR-target's translation would change in response to bortezomib, and it would change more in cells with an intact ISR. After filtering all differentially translated genes as described above and visualized in figure 5.3, I selected only those genes which also changed in terms of translational efficiency, setting a cutoff as a TE change greater than 1.5 fold (Figure 5.4, A). Using this analysis I detected genes that were both up and down-regulated in terms of translational efficiency in each comparison (Figure 5.4, A & B). Interestingly, a subset of highly abundant genes were potently down regulated in response to bortezomib, something consistent with the known role of the ISR in inhibiting translation of housekeeping genes (Figure 5.4, B).

Gene lists were created as described above, and as a stringent approach to curate ISR-targets, we further filtered these lists by collecting the overlap of the datasets, and we moved on with analyses of genes that changed in response to ISR activity (Figure 5.4, D & F). To understand if sets of related genes were being targeted by the ISR for translational up or down-regulation, GO-term analysis was performed, searching for genes sets of genes corresponding to common biological processes or cellular components. I included the GO-term cellular component analysis out of interest in identifying regulated structural and cytoskeleton components. The downregulated genes were clearly enriched in components of translational machinery, which is consistent with the known role for the ISR pathway in downregulating translation and housekeeping gene synthesis (Figure 5.4, F). Interestingly, it seemed that the ISR was not only directly decreasing translation by inhibiting translation initiation, but the ISR may also be indirectly decreasing translation by specifically targeting translational machinery for down-regulation.

GO-term analysis of the upregulated ISR-targets was especially interesting. The centrosome was the one cytoskeletal component that was enriched in these genes (Figure 5.4, F & G). The centrosome is the major microtubule organizing center (MTOC) within a cell (Caviston & Holzbaur, 2006; Sanchez & Feldman, 2017; Woodruff et al., 2017). It's location determines the inner-outer polarity of a cell, and also has a major role in regulating cell polarity and intracellular transport (Musch, 2004). This enrichment further stood out because it is well-documented that aggresome formation requires retrograde transport on an intact microtubule cytoskeleton, and the aggresome forms at the MTOC (Johnston et al., 1998; Kopito, 2000). This seemed potentially connected to the previous finding that ISR-null cells could not effectively form aggresomes during the recovery from proteotoxic stress, and it suggested the new hypothesis that in response to proteotoxic stress the ISR is regulating the MTOC in a way that promotes aggresome formation and recovery of proteostasis.

Figure 5.4: The integrated stress response upregulates centrosomal proteins in response to proteotoxic stress.

A. Filtering strategy to identify genes targeted by the ISR for selective translation during proteotoxic stress.

B. Plot of translational efficiency fold change (RPF/total mRNA) relative to transcript abundance (average normalized mRNA counts across all samples) for S51-bortezomib verses S51-vehicle.

C. Same as in B. but for the comparison of S51-bortezomib vs. S51A-bortezomib.

D. Overlap of genes found to be upregulated in both B. and C.

E. Overlap of genes found to be downregulated in both B. and C.

F. GO-term analysis of ISR-targets.

G. Gene list of upregulated ISR-targets with known centrosomal proteins highlighted.

Figure 5.4: The integrated stress response upregulates centrosomal proteins in response to proteotoxic stress.

A

Filtering strategy

RPF reads FC > 1.5 and padj<0.05 ⟶ Translational efficiency (RPF/total mRNA) FC > 1.5 ⟶ ISR targets, overlap of:
1. S51 bort vs. S51 veh
2. S51 bort vs. S51A bort

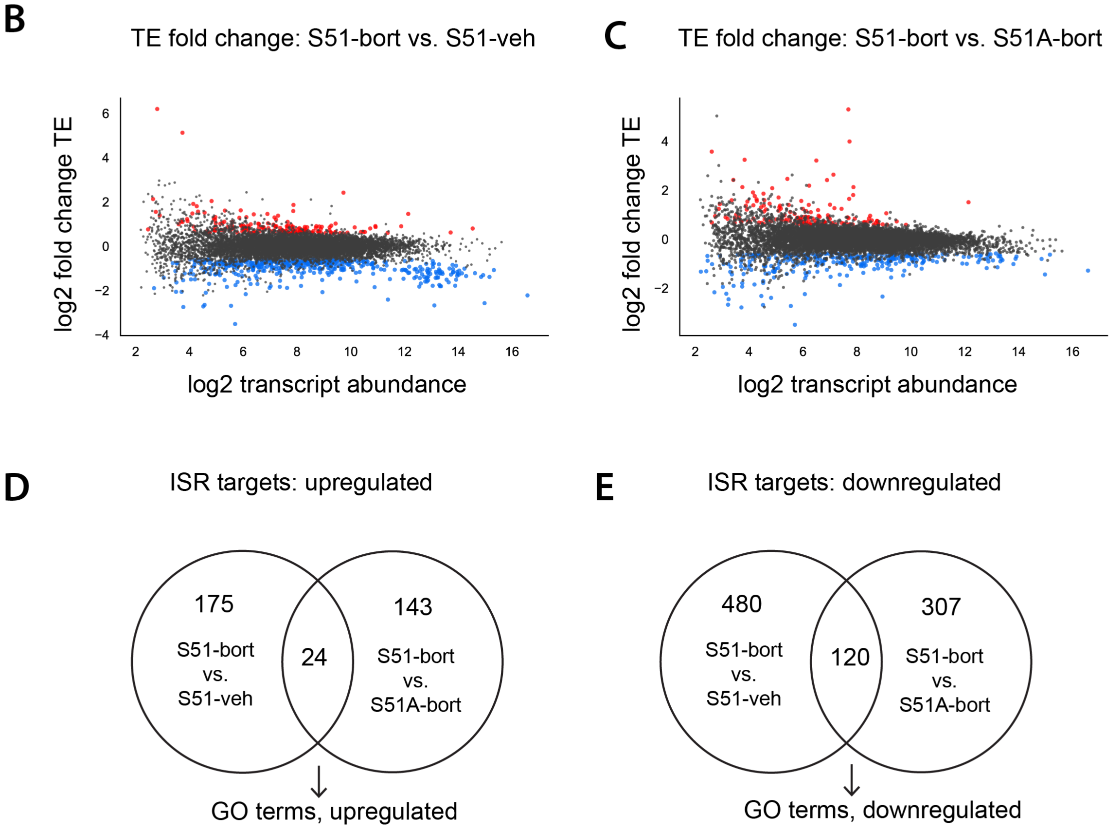

F

Biological process	**Cellular component**	**Biological process**	**Cellular component**
Positive regulation of transcription (p=7.0E-5)	**Centrosome (p=0.0010)**	Translation (p=3.02E-19)	Ribosome (p=7.17E-24)
Response to amino acid starvation (p=0.0180)	CHOP-ATF3 complex (p=0.0021)	Ribosomal small subunit assembly (p=1.50E-7)	Small ribosomal subunit (p=02.92E-16)
Unfolded protein response (p=0.00140)	CHOP-ATF4 complex (p=0.0021)	Insulin receptor signaling pathway (p=6.72E-7)	Cytosolic RNP complexes (p=1.64E-14)

G

Upregulated gene list

Map3k8, Atf5, Apobec1, Ppp1r15a, Atf3, Atf4, Zfp874a, Ddit3, Parp14, Thoc2l, Hap1, Cspp1, Asprv1, Impact, Fktn, Fabp4, Gm14403, Bbs4, Metrnl, Tmem68, Pard6a, Clk4, 9930104L06Rik, Fbxw7

* Centrosome associated proteins *

I first sought to confirm that confirm that aggresomes formed at the MTOC within our cells. Confocal microscopy targeting p62/SQSTM (aggresome) and γ-tubulin (MTOC) clearly demonstrated that the aggresome formed near or surrounding the MTOC in control cells recovering from proteotoxic stress (Figure 5.5, A). Moreover, in the rare ISR-null cells that did have p62-positive aggresomes, these aggresomes also formed near the MTOC (Figure 5.5, B). These aggresomes did often appear more diffuse, however.

Figure 5.5: The aggresome forms at the centrosomal microtubule organizing center (MTOC).
A. Aggresomes in S51 cells treated with bortezomib and allowed to recover for 8 hours visualized by immunofluorescence for p62/SQSTM and the MTOC visualized by staining for γ-tubulin.
B. S51A cells visualized during the recovery phase.

Figure 5.5: The aggresome forms at the centrosomal microtubule organizing center (MTOC).

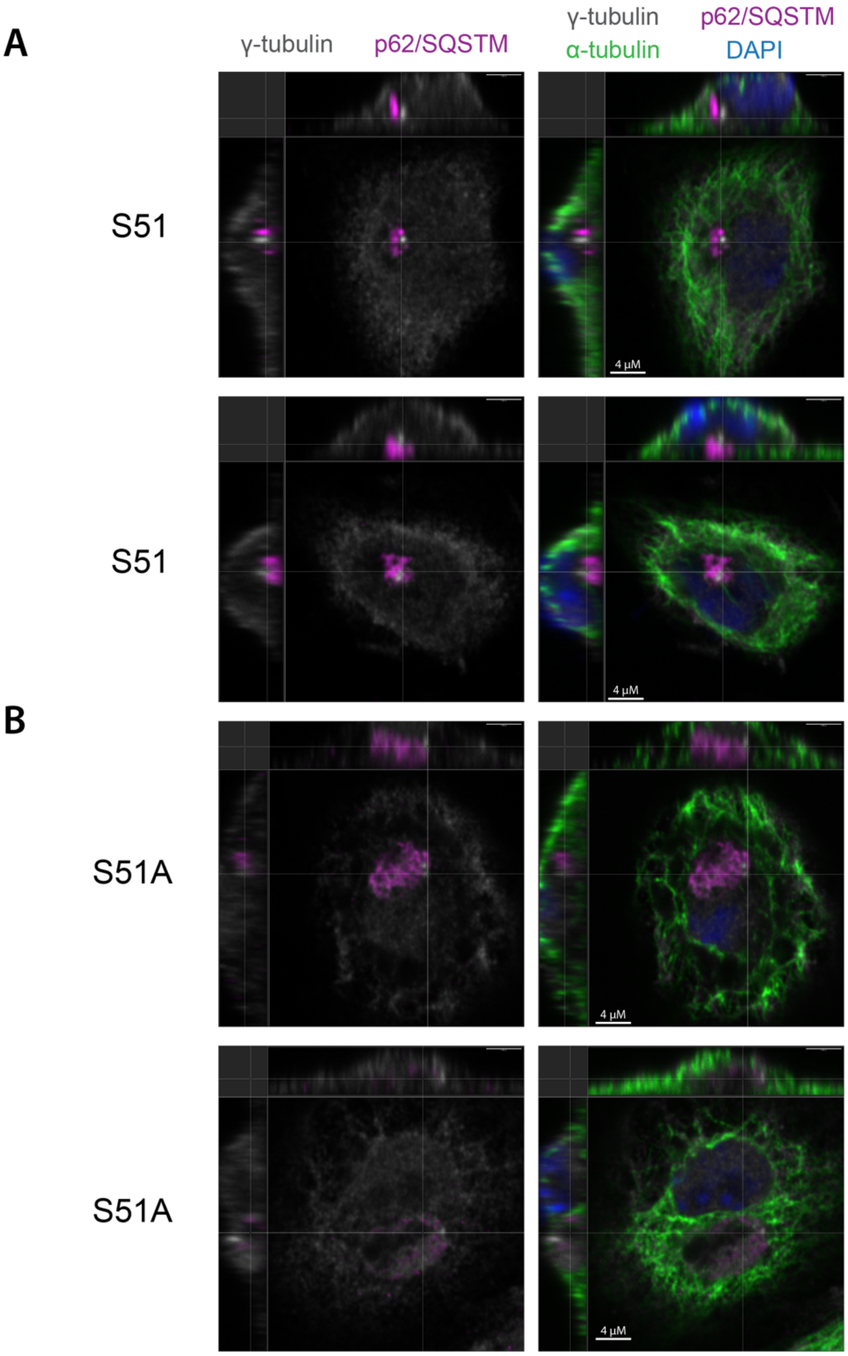

In the previous experiment I noticed that the MTOC staining intensity seemed to be different between control and ISR-null cells in the recovery phase, so I sought to quantify this directly. Using two MTOC markers, γ-tubulin and pericentrin, I evaluated MTOC size and found that the MTOC staining intensity and size with both markers appeared to increase in control, but not ISR-null, cells recovering form proteotoxic stress (Figure 5.6). To quantify these apparent MTOC changes, I performed volumetric analysis of the MTOC using Imaris, a software designed to reconstruct and analyze 3-dimensional images from confocal microscopy. I used the site of peak pericentrin staining to create a region of interest surrounding the MTOC, and for each single MTOC particle I could quantify the volume, pericentrin staining intensity, and γ-tubulin staining intensity (Figure 5.7, A). Quantification revealed that during the recovery phase the control cells' MTOCs more than doubled in size and staining intensity of the two MTOC markers, a change that was significantly lost in ISR-null cells (Figure 5.7, B).

Figure 5.6: The MTOC increases in size in response to proteotoxic stress, an effect that is dependent on the ISR pathway.

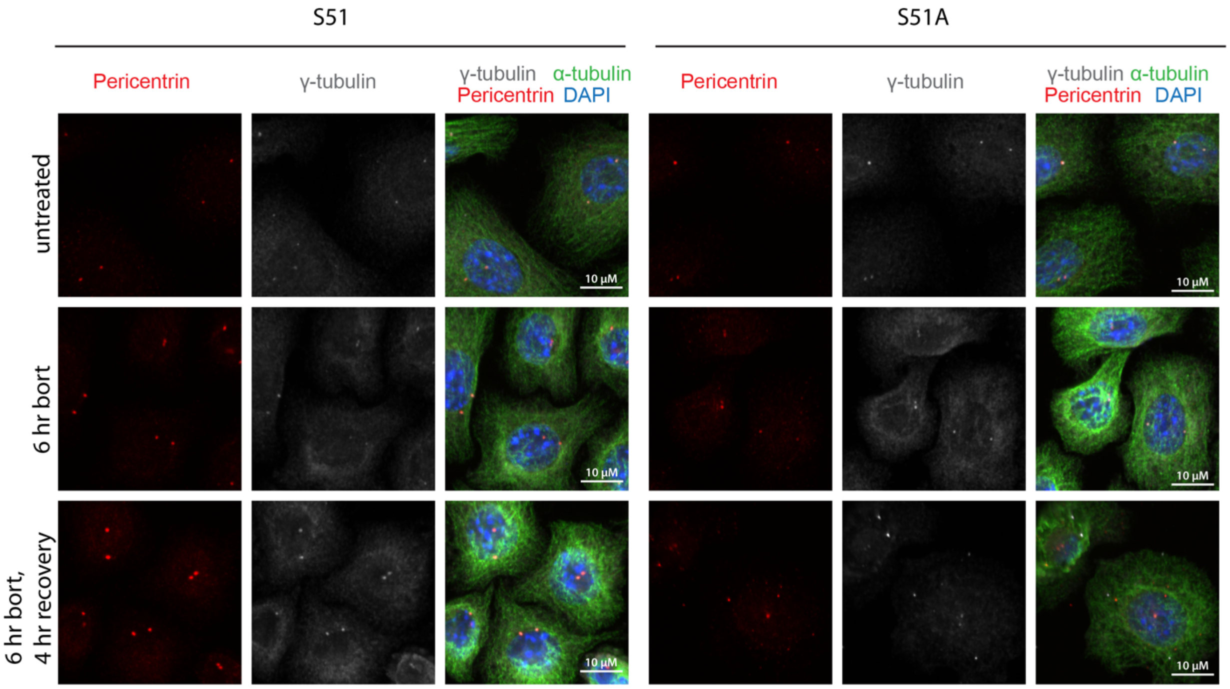

Figure 5.6: The MTOC increases in size in response to proteotoxic stress, an effect that dependent on the ISR pathway.
The MTOC is visualized using immunofluorescence against two markers, pericentrin and γ-tubulin.

Figure 5.7: Immunofluorescence quantification of MTOC markers during proteotoxic stress recovery.

A. The MTOC is visualized by immunofluorescence targeting pericentrin and γ-tubulin. This is used to create a volumetric region of interest which can be used to quantify the MTOC volume and staining intensity for MTOC markers.

B. Quantification of MTOC volume in S51 or S51A cells at rest, treated with bortezomib for 6 hours, or treated with 6 hours of bortezomib and allowed to recover for 4 hours.

C. Same as in B. but pericentrin total fluorescence intensity per MTOC is quantified.

C. Same as in B. but γ-tubulin total fluorescence intensity per MTOC is quantified.

Figure 5.7: Immunoflourescence quantification of MTOC markers during proteotoxic stress.

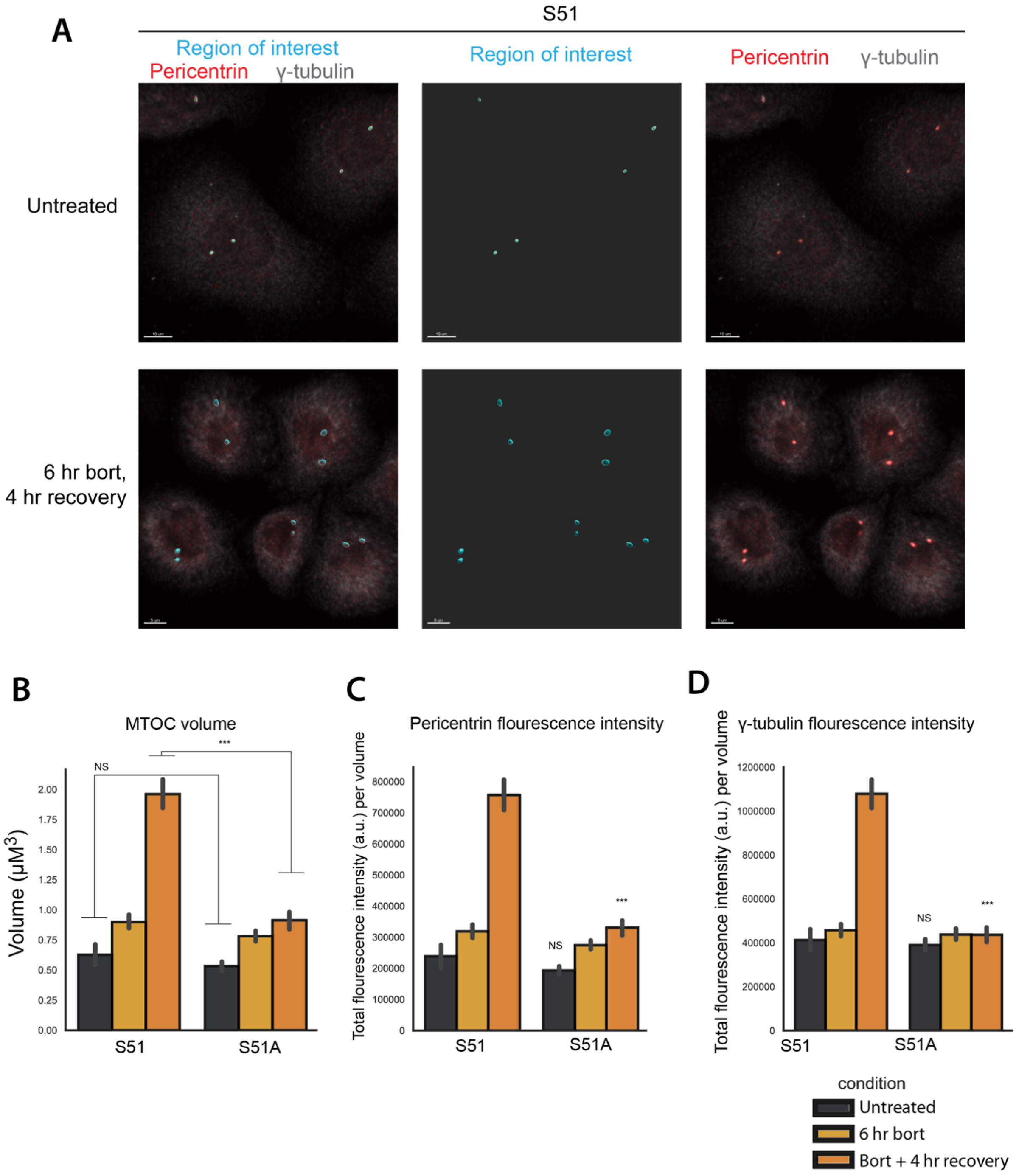

To better understand the relationship between the microtubule cytoskeleton and the aggresome in our cells, I investigated the effect of disrupting microtubule dynamics on proteostasis recovery. Microtubules are dynamic structures which grow out from the MTOC and shrink back (Alberts, 2015). To disrupt this process I treated cells with paclitaxel, a chemotherapy that prevents the depolymerization of microtubules essentially freezes microtubules in the cell. To ask if treatment with paclitaxel inhibits aggresome formation, cells were simultaneously treated with 200 nM of paclitaxel along with bortezomib, and, when bortezomib was washed out, paclitaxel was maintained in the media. Indeed inhibiting microtubule dynamics potently blocked aggresome formation following bortezomib treatment (Figure 5.8, A & B).

Figure 5.8: Inhibiting microtubule dynamics with paclitaxel blocks aggresome formation.
A. The aggresome is visualized using immunofluorescence for p62/SQSTM in cells allowed to recovery from bortezomib with or without microtubule stabilizing agent, paclitaxel.
B. Quantification of percentage of cells with aggresome present at 4 hours or 8 hours of recovery from bortezomib.

Figure 5.8: Inhibiting microtubule dynamics with paclitaxel blocks aggresome formation.

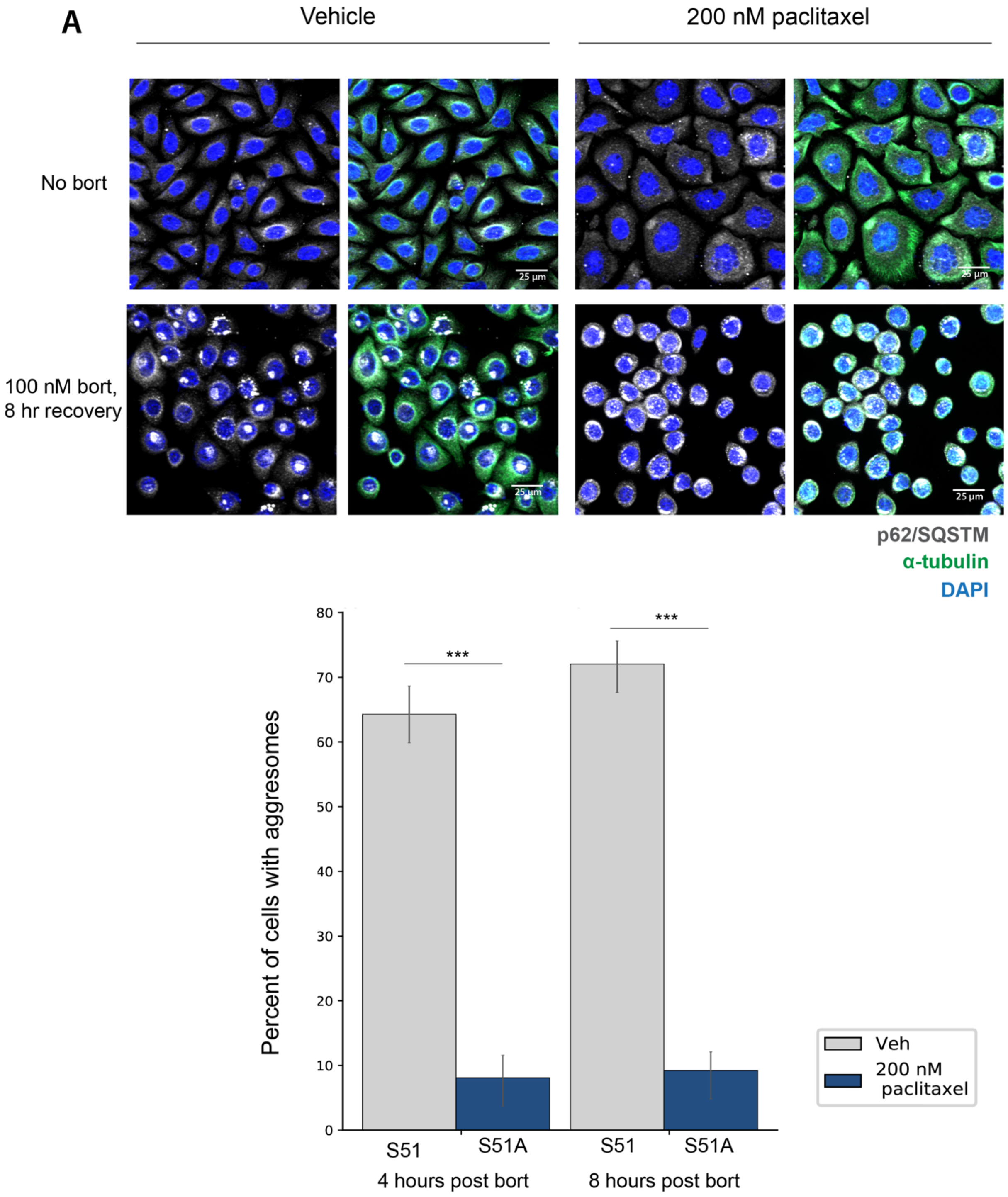

The importance of the microtubule cytoskeleton for aggresome formation has long been recognized (Johnston et al., 1998). Here I find an unexpected role for the integrated stress response in regulating this process through selective translation of centrosomal proteins. In cells lacking the integrated stress response, when challenged to clear protein aggregates, the cells fail to enlarge the MTOC and also do not localize protein aggregates as clearly to the MTOC region. This, in conjunction with the ribosome profiling results, strongly suggests that upregulating centrosomal proteins is a major role for the ISR in promoting proteostasis. Still unknown is the contribution of the individual centrosomal genes to this process. Critical future directions would be to knock down these proteins individually and evaluate aggresome formation. Additionally informative would be rescue experiments in which one or more of these proteins is induced in ISR-null cells during stress recovery. These experiments could identify major players within the gene list, although it is possible that a single gene is not dominant and the entire cohort needs to be targeted for selective translation to effectively form the aggresome. Multiple transcription factors also emerged from our ribosome profiling data set (CHOP, ATF3, ATF4, ATF5), and it would be interesting to know how these genes are regulating transcription in response to stress. One of these genes, ATF5, has been previously found to play a role at the centrosome (Madarampalli et al., 2015), so it would be additionally interesting to question whether ATF5's role in proteostasis is transcriptional or rather is a structural role at the MTOC.

Overall these data suggest a novel role for the integrated stress response in removing protein aggregates from the cell. While the pathway has been previously implicated in sensing protein aggregates (Abdel-Nour et al., 2019), to our knowledge this is the first time that the pathway has been so clearly implicated in the clearance of these protein aggregates. Moreover, the aggresome has been well appreciated as an important cytoprotective structure in cells challenged with protein aggregates, and this study has made the surprising connection that forming this structure requires the ISR pathway. These findings elevate the importance of the ISR as a pathway that guards proteostasis. Future work on this pathway could lead to novel therapeutic approaches to maintain proteostasis in human health, a goal that could lead to better outcomes in a diseases ranging from Cystic Fibrosis to Parkinson’s Disease.

Chapter 6:

High-throughput screen for chemical inhibitors of eIF2A-mediated translation

Part 1: Establishing eIF2A as a therapeutic target.

Translational regulation is increasingly recognized as an important and complex driver of cancer phenotypes. Although research into cancer-associated translation is still in its early days, the advent ribosome profiling, a technique to measure translation genome wide, has dramatically accelerated discoveries in this area (Ingolia et al., 2014; Ingolia et al., 2011). Previous work from our lab leveraging this technique helped to identify one translation initiation factor, eIF2A, as a promising target for future anticancer therapeutics (Sendoel et al., 2017). eIF2A is an alternative translation initiation factor that instructs ribosomes to translate stress-response proteins when protein synthesis rates are low (Starck et al., 2016).

Foundational work by Dr. Ataman Sendoel, a former postdoctoral researcher in the Fuchs lab, demonstrated that cancer cells within oncogenic lesions have grossly dysregulated translational landscapes as assessed by ribosome profiling. Notably, cancer cells target an increased number of putative stress-response genes with upstream open reading frames (uORFs) translated from transcript 5' untranslated regions (5' UTRs) (Sendoel et al., 2017). Previous ribosome profiling datasets from multiple laboratories found uORF translation to a surprisingly common process (Ingolia et al., 2014; Meijer & Thomas, 2002), and work from the Shastri and Walter laboratories identified eIF2A as an initiation factor that drives a subset of uORF translation with consequences for translation of downstream coding sequences (Starck et al., 2012; Starck et al., 2016).

Connecting these results, Dr. Sendoel hypothesized that eIF2A would possess oncogenic function by driving the changes we observed in the translational landscape of cancer. To test this, clonal, isogenic, primary squamous cell carcinoma cell lines (HRas-

G12V;TGFbetaRII-null) were generated with eIF2A knocked out (eIF2A-KO), plus isogenic controls. Consistent with the hypothesis, eIF2A-KO SCC lines formed tumors significantly less efficiently than controls when implanted as allografts into athymic nude mice, and this effect was rescued with re-expression of eIF2A (Fig. 1, A & B). To support the oncogenic role of eIF2A, Dr. Sendoel also tested the effect of genetic loss of function of the protein in a second cancer model. In this experiment we found shRNA-targeting eIF2A delivered by in-utero lentiviral injection to be down-regulated in neonatal skin transformed by expression of the oncogene, Sox2, relative to control skin, in which eIF2A-shRNA was tolerated to a greater extent (Fig. 1, C)

With these results in mind, and encouraged by data from human head & neck SCC, in which we found eIF2A to be frequently amplified and associated with poor survival (Fig. 1, D), we sought to identify eIF2A target genes with the hope of developing reporters that could be used to screen for small-molecule inhibitors of this oncogenic process.

Figure 6.1: Establishing eIF2A as a therapeutic target

A. CRISPR-Cas9 knockout of eIF2A decreases tumor initiation efficiency as assessed by limiting dilution assay.

B. Reconstitution of eIF2A expression in knockout cells rescues tumor growth.

C. Targeting eIF2A for knockout with CRISPR-Cas9 and lentivirally-delivered sgRNA is more tolerable to wild-type epidermis relative to transformed, Sox2-expressing epidermis.

D. EIF2A mRNA upregulation correlates with decreased overall survival and disease-free survival in patients with head and neck SCC. Data was acquired from TCGA and stratified according to EIF2A mRNA expression z-score >1.75 (27% of patients) verses remaining.

Figure 6.1: Establishing eIF2A as a therapeutic target.

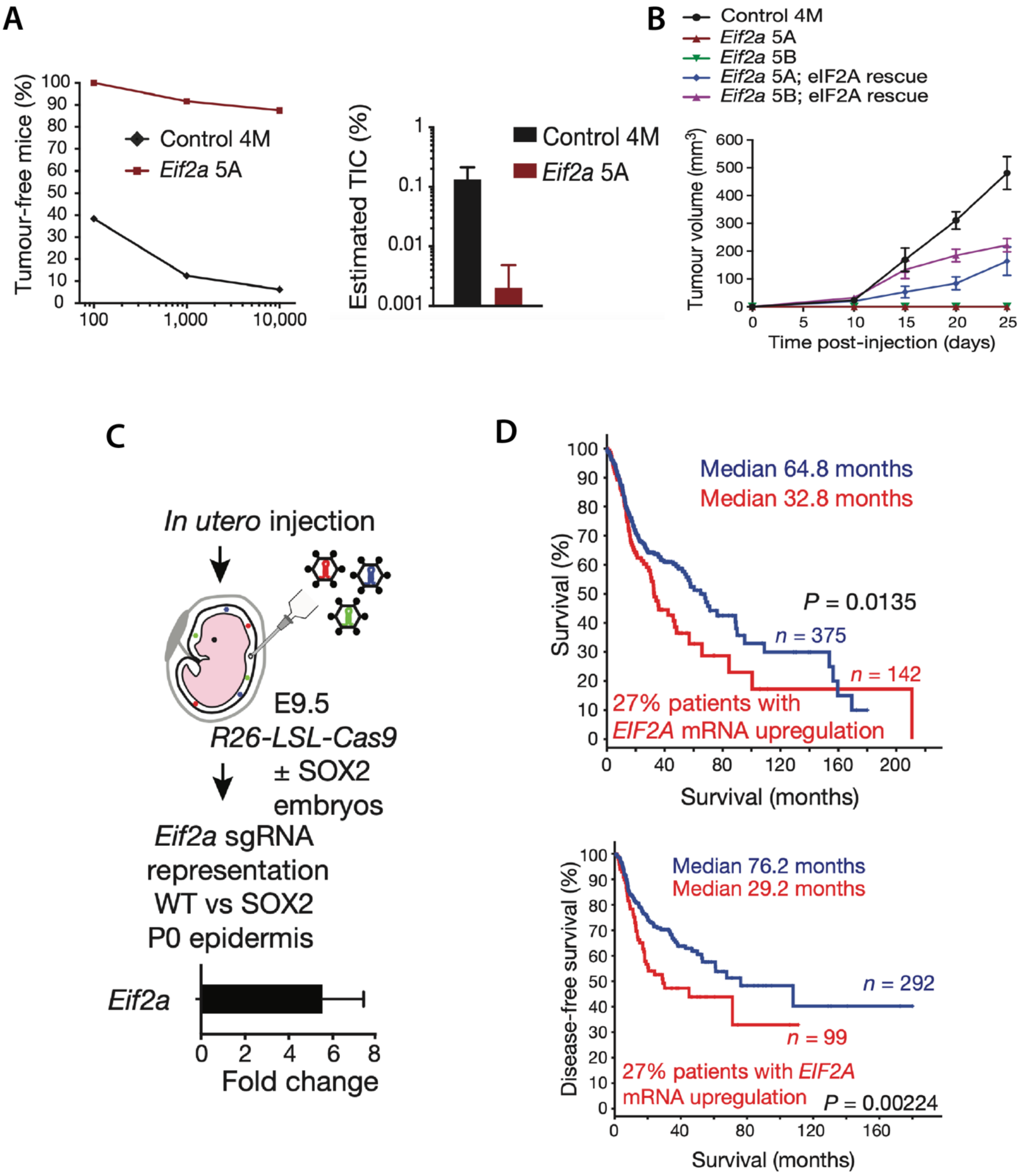

Part 2: Developing eIF2A reporter cell lines.

Translational targets of EIF2A were determined using an *in vitro* model of cellular stress that induces translation of uORF-containing transcripts. The experimental approach was to leverage pulsed-SILAC (stable isotope labelling with amino acids in cell culture) along with the chemical stressor, sodium arsenite. Dr. Sendoel cultured eIF2A-KO and control cells in "light" isotope media and then added sodium arsenite while simultaneously switching the cells to "heavy" isotope media. Cells were subsequently lysed and analyzed by quantitative mass-spectrometry to identify proteins only upregulated by stress in the presence of eIF2A (Fig. 2, A) (Sendoel et al., 2017). At this point I began my collaboration with Dr. Sendoel, and we compared this dataset with previous ribosome profiling results which identified proteins with uORF translation, and selected a panel of genes with eIF2A-dependent translation and uORFs which we hypothesized engendered these 5' UTRs with the best potential to develop a novel eIF2A reporter assay (Fig. 2, B).

Figure 6.2: eIF2A targets uORF-containing genes for translation during stress
A. pulsed-SILAC quantitation of the proteome following stress reveals upregulated proteins that are dependent upon eIF2A.
B. eIF2A-targeted uORF genes (as assessed by ribosome profiling) are upregulated at the protein level during arsenite stress.

Figure 6.2: eIF2A targets uORF-containing genes for translation during stress.

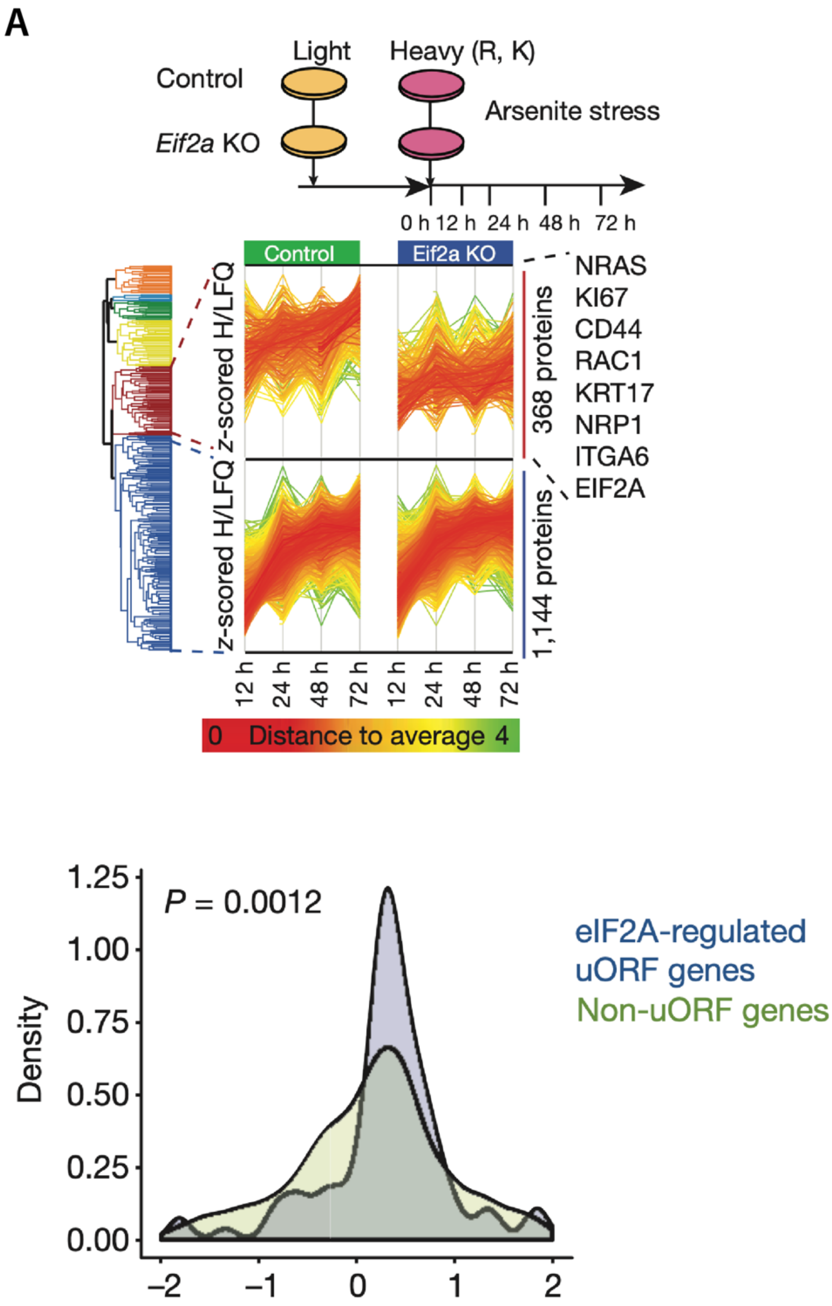

EIF2A reporters were first generated by cloning the 5' UTRs of our selected genes and fusing this regulatory sequence onto the 5' end of the bioluminescent reporter, firefly luciferase. The 5' UTR of HBB, a housekeeping gene not targeted by eIF2A, was fused to the 5' end of an orthogonal reporter, renilla luciferase, for use as an internal control (Fig. 3, A). Cells were transiently transfected with these reporters and stress was induced with sodium arsenite. A reporter with the 5' UTR of one gene, Atf4, was found to perform best, with robust stress-induced translation that was partially eIF2A-dependent. This reporter was selected for further optimization.

I next modified the eIF2A-reporter assay for high throughput applications by cloning both the Atf4-firefly-luciferase and HBB-renilla-luciferase reporters (hereafter referred to as Atf4-*firefly* and HBB-*renilla*, respectively) into a single lentiviral vector that could be used to generate cell lines stably expressing the reporter genes. I iteratively optimized the new dual-reporter by testing different backbones, promoters, and transgene orientations, and settled on a plasmid that performed well by transient transfection (Fig. 3, A). Dr. Sendoel's lab at the University of Zurich took the best construct, generated lentiviral particles containing this sequence, transduced primary SCC cells, and generated clones using G418 followed by single cell cloning (Fig. 3, B). Both Dr. Sendoel and I screened a number of clones for robust reporter activity and selected one clone for follow up studies (Fig. 3, C). To further support that our assay was successfully reporting on eIF2A activity, Dr. Sendoel also transduced eIF2A-KO cells and compared the reporter activity from nonclonal, G418-selected eIF2A-KO reporter lines to reporter activity from control lines and found that targeting eIF2A with CRISPR-Cas9 partially diminished reporter activity, consistent with our previous results (Fig. 3, D).

Figure 6.3: Developing and validating eIF2A-reporter cell lines.
A. Dual-reporter lentiviral construct containing eIF2A-targeted Atf4-*firefly* and housekeeping control HBB-*renilla* with P2A-Neomycin resistance fused for antibiotic selection.
B. Strategy for testing and selecting clonal eIF2A reporter cell lines.
C. Clonal eIF2A-reporter cell lines were screened for Atf4-*firefly* induction upon stress.
D. Comparison of stress-induced Atf4-*firefly* induction in nonclonal control and eIF2A KO SCC cells.

Figure 6.3: Developing and validating eIF2A-reporter cell lines.

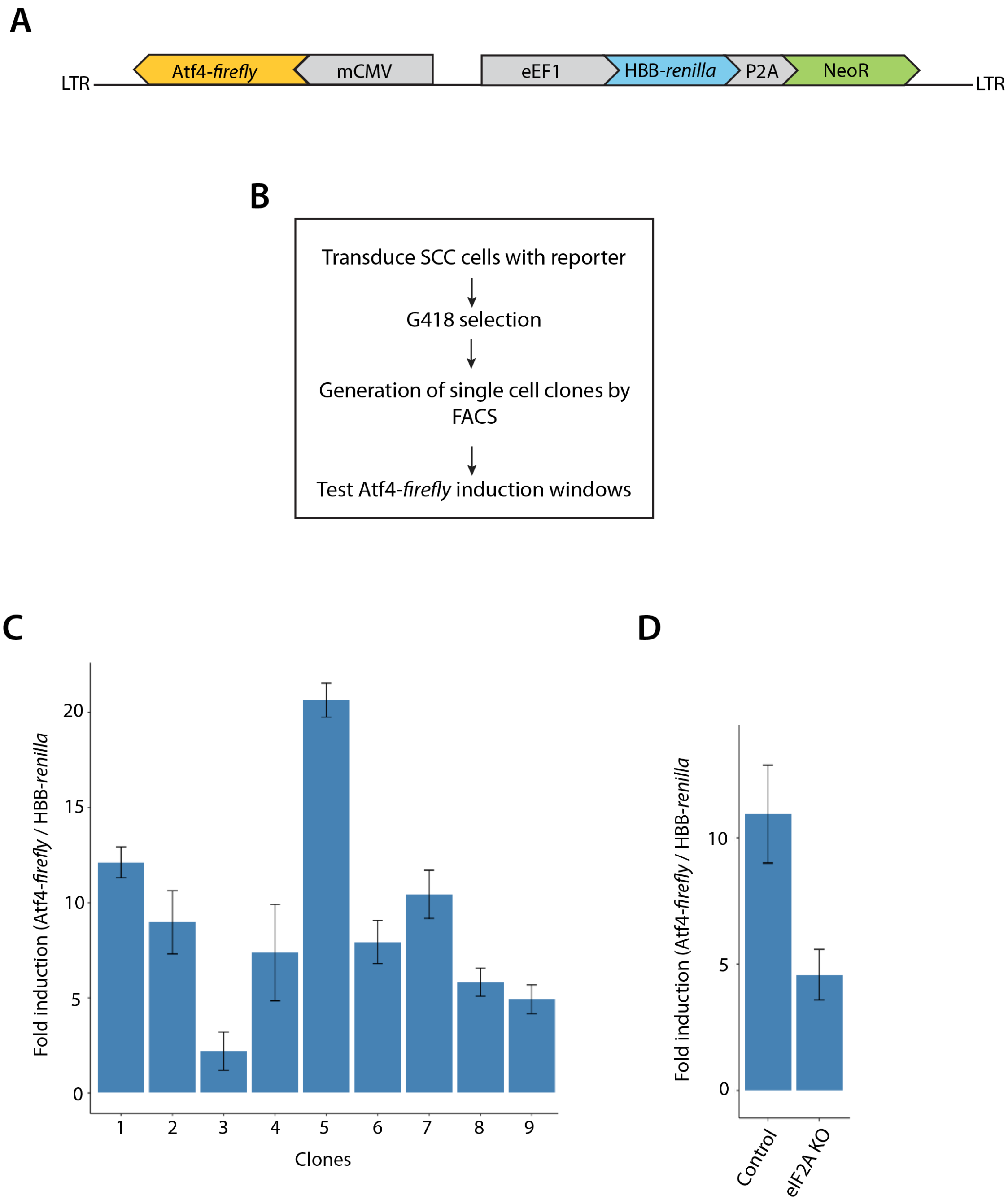

Part 3: Scaling and validating assay in high-throughput format for screening.

In collaboration with the Rockefeller University High Throughput Screening and Spectroscopy Center, I prepared to use the eIF2A-reporter cell line for high-throughput screening. First, I performed a series of experiments to optimize the assay protocol for 384 well plates. I titrated cell number and determined that plating 8000 cells per well yielded the best reporter activity (Fig 4, A). I subsequently tested a series of sodium arsenite concentrations and treatment schedules and found that incubating cells in 30 μM of arsenite for 7 hours consistently produced the highest Atf4-*firefly* induction window (Fig. 4, B).

Figure 6.4: Optimizing eIF2A-reporter assay for high-throughput screening.
A. Titrating optimal number of cells plated in each well of 384-well plates.
B. Optimal combination of arsenite concentration and timepoint was determined to be 30 μM for 7 hours.

Figure 6.4: Optimizing eIF2A-reporter assay for high-throughput screening.

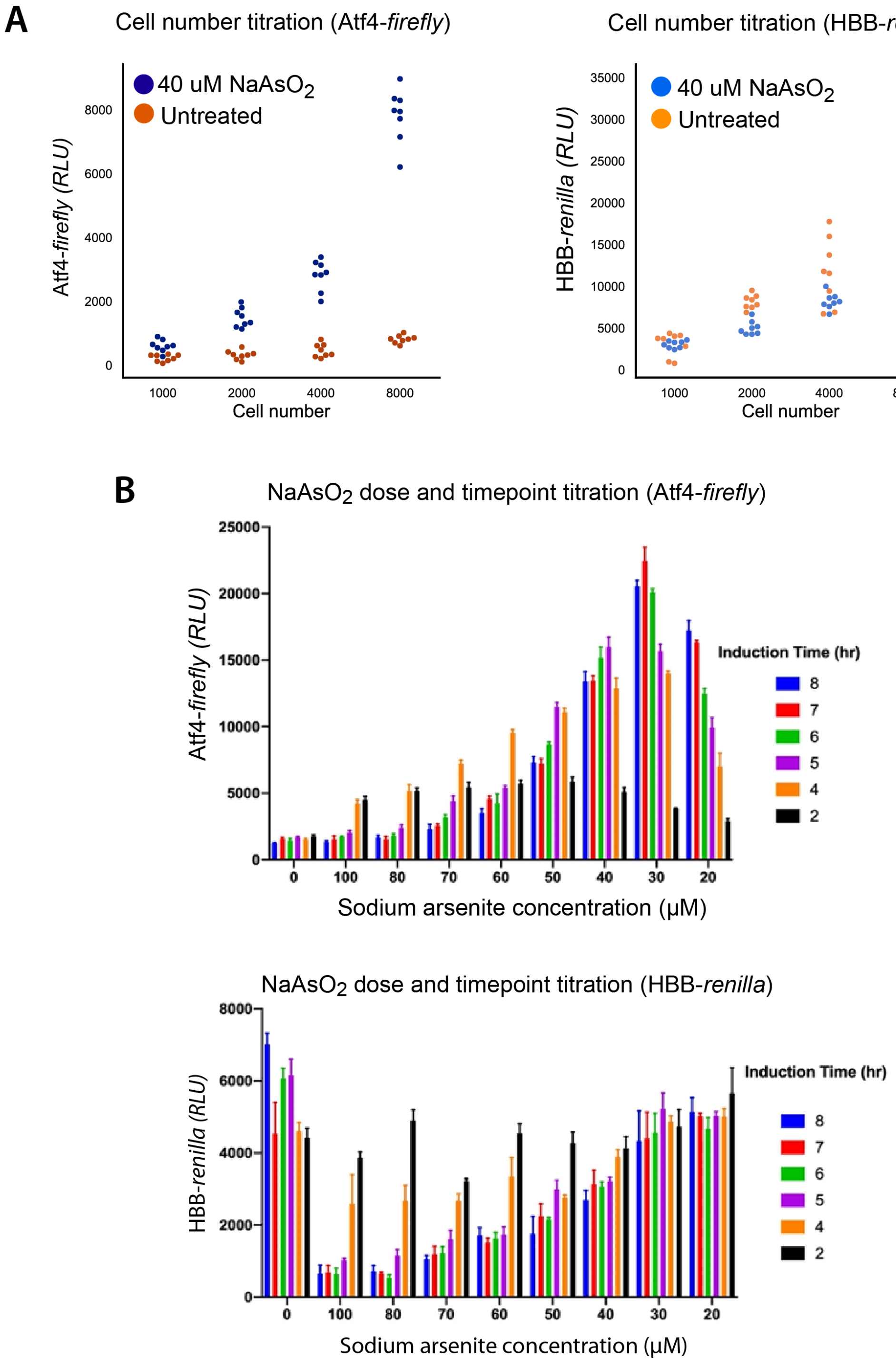

I went on to validate assay robustness and reproducibility using a full 384-well plate "Z-prime" assay. In this experiment I alternated columns with or without sodium arsenite and evaluated the induction window and variability to generate a Z' statistic (Z' = 1-(3*(SD low+ SD High)/(avg high - avg low))). Over two assays I found assay results to be repeatable and Z' statistics for Atf4-*firefly* to be 0.54 and 0.61, which met the goal of 0.5 (Fig. 5, A&B). I further tested the performance of the assay in the presence of compounds curated in the Millipore Sigma LOPAC, "library of pharmaceutically active compounds". Results were consistent between two runs, and I found only few compounds inhibiting reporter activity, supporting that the assay was performing robustly and specifically enough to proceed with the primary screen (Fig 6, A-C).

Figure 6.5: eIF2A-reporter assay scaled-up and statistically validated by Z-prime assay.
A. Whole-plate reporter test run with Z-prime statistic calculated.
B. Same as in A. but repeated on a separate day.

Figure 6.5: eIF2A reporter assay scaled-up and statistically validated by Z-prime assay.

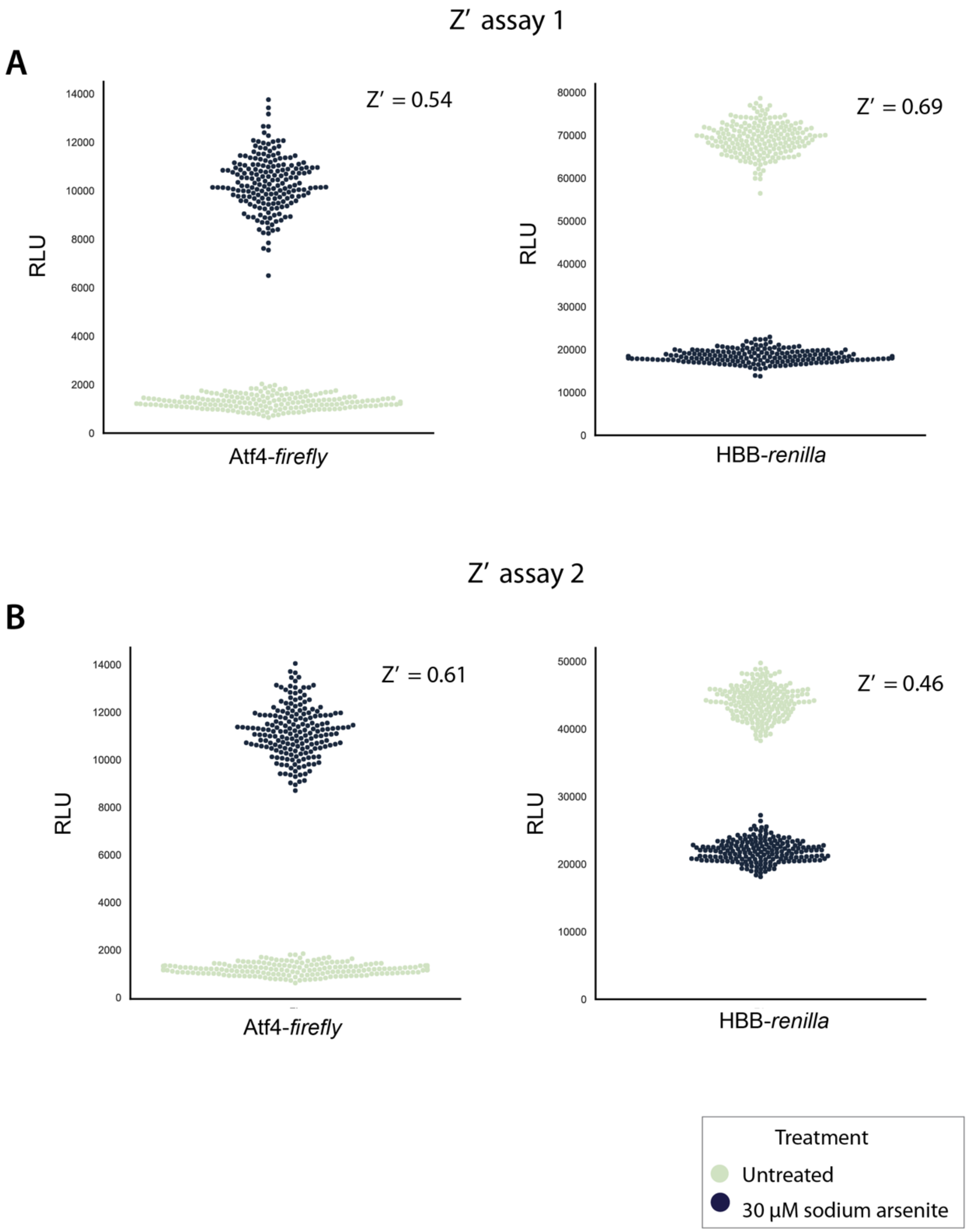

Figure 6.6: Testing assay repeatability with pilot-screen of known drugs.
A. Representative dataset of Atf4-*firefly* from one day of screening known drugs in "library of pharmaceutically active compounds" (LOPAC, Millipore Sigma).
B. Representative dataset of HBB-*renilla* from say day as in A.
C. Correlation plot of Atf4-*firefly* % NPI from two separate days of pilot screen.

Figure 6.6: Testing assay repeatability with pilot-screen of known drugs.

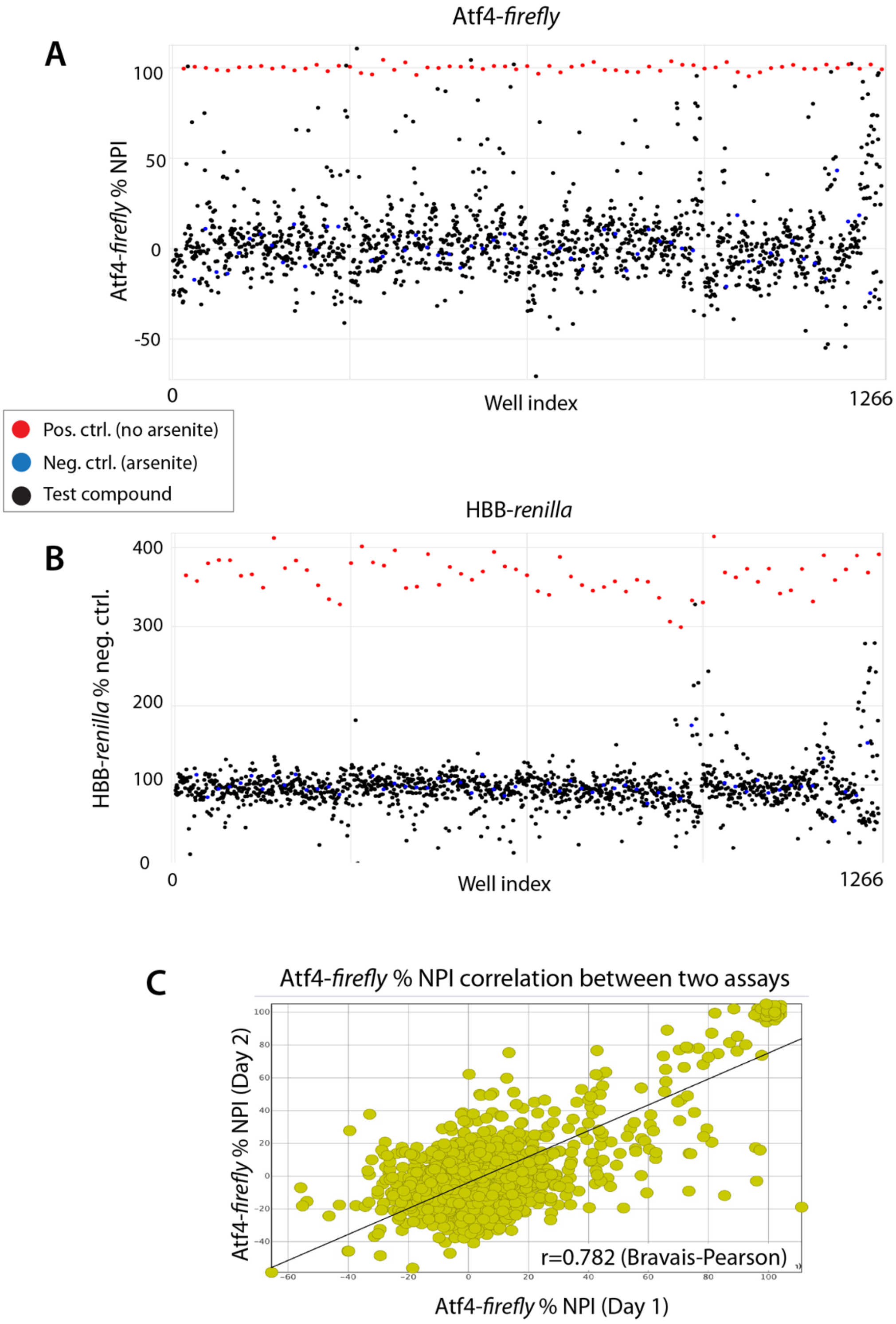

Part 4: Primary screen results.

I proceeded with high-throughput screening using the library of small molecules collected by the Rockefeller University High-throughput and Spectroscopy Resource Center. Compound plates were screened with a goal of screening over 50,000 small molecules in total. The Rockefeller compound library contains over 400,000 compounds, and Dr. Fraser Glickman, director of this core facility, selected plates for screening by curating a list of the plates with the highest average scores for "druglikeness" as assessed bioinformatically.

The screen progressed as follows, screening was gradually ramped up until I could consistently run 16 plates per day, which corresponded to over 5000 compounds (n=1 per compound). I repeated any plates that failed quality control as assessed by a Z' value on two control columns. After screening 20,000 compounds, the screen was paused, and I validated a selection of compounds that appeared as "hits" in the beginning of the screen. These compounds were mostly validated in dose-response format, which supported that the screen was working reproducibly, so I proceeded to finish screening the collection. Data from a single representative day of screening >5000 compounds is shown (Fig. 7, A & B).

Figure 6.7: Representative primary screen data from single day of screening.
A. Atf4-*firefly* normalized percent inhibition (Atf4-*firefly* % NPI) from representative day of screening > 5000 compounds.
B. HBB-*renilla* percent negative control (% neg. ctrl.) from same dataset as in A.

Figure 6.7: Representative primary screen data from single day of screening.

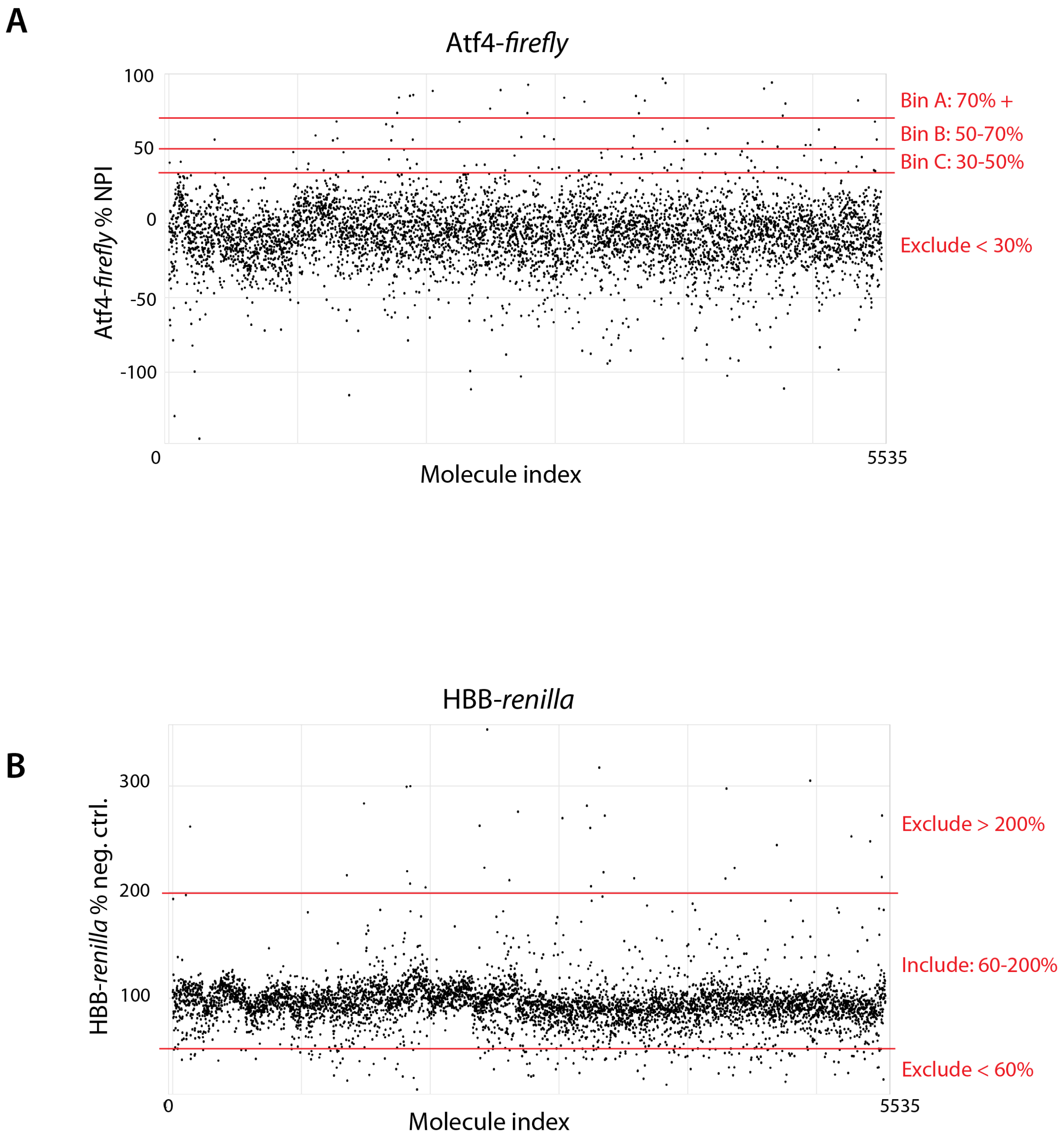

Part 5: Confirmation and validation of primary screen results and final hit selection.

Following the completion of the primary screen, compounds were selected for follow up with assistance of the Tri-Institutional Drug Discovery Institute (Tri-I TDI). We used a multiple-filter strategy to first select potential hits. For the first filter, included compounds had an Atf4-*firefly* "normalized percent inhibition" (Atf4-*firefly* % NPI) value of 30% or greater. Compounds were additionally binned into three groups with 30-50%, 50-70%, and >70% Atf4-*firefly* % NPI with compounds having greater values selected with higher confidence. For the second filter, included compounds would have an HBB-*renilla* "percent negative control" (HBB-*renilla* % neg. ctrl) corresponding the arsenite-treated of 60-200%. The rationale for this filter was that compounds causing additional decrease of HBB-*renilla* % neg. ctrl to below 60% were likely to be cytotoxic, and compounds rescuing HBB-*renilla* % neg. ctrl to levels greater than 200% would potentially be blocking the effect of sodium arsenite or inhibiting upstream activators of the integrated stress response rather than eIF2A downstream.

Following primary hit selection, a final hit list was curated with the help of collaborating chemists at the Tri-I TDI. To proceed with hit curation as methodically as possible, four chemists voted on their confidence in a compound, with a summing of votes and ranking followed by group discussion and decision. The criteria for selection were as follows: potency from primary screen, drug-like properties (eg. MW<500 and ClogD "druglikeness" score of 1-4), low potential as a pan-assay interference compound, lack of potentially reactive intermediates (eg. aldehydes, nitro-, and aliphatic cyanides), lack of poor stability groups (eg. esters), and favorable clustering that suggested potential structure-activity relationships.

Using the following criteria we selected 200 compounds for follow up triplicate confirmation. Out of these 122 compounds were confirmed, and these were selected for validation, and dose-response plates were generated. I performed two dose-response validation assays with separate orthogonal stressors. I first validated compounds' dose-responses with sodium arsenite, as in the primary screen (Fig 8, A & B - representative dose-response plots). I then repeated the validation experiment with tunicamycin, a chemical inducer of ER-stress. I selected this orthogonal stressor because ER-stress activates the eIF2α-kinase, Perk, whereas sodium arsenite activates a separate eIF2α-kinase, HRI, and I sought to eliminate potential HRI-binding compounds that may have had a positive result in the primary screen. Dose response plots could then be compared between the two validation assay to select hits that had plausible dose-response relationships in both of the validation assays. Representative dose response plots from a compound selected for follow up (Fig. 8, A) and a compound excluded from follow up due to negative result in the tunicamycin validation experiment (Fig. 8, B) are shown.

At this point I again consulted with collaborators at the Tri-I TDI, and selected a limited number of final hits. We assessed dose response plots from both Atf4-*firefly* and HBB-*renilla* in both the sodium arsenite and tunicamycin validation experiments. We again used two filters, selecting hits with plausible dose response relationships for Atf4-*firefly* with both stressors (plausible meaning a steep slope and EC50 < 20uM), and eliminated compounds with dose-response relationships for HBB-*renilla* that suggested that the compounds were either cytotoxic or targeting upstream proteins, as described previously. With these criteria we selected 29 hits, from which we continue working to select lead compounds.

Figure 6.8: Representative data from validation assays.

A. Dose-response plots of Atf4-*firefly* % NPI and HBB-*renilla* % neg. ctrl. of a compound selected for follow up based on the compound's effect on Atf4-*firefly* % NPI in both sodium arsenite and tunicamycin validation assays and a lack of effect on HBB-*renilla* % neg. ctrl. in either assay.

B. Dose-response plots of compound excluded from analysis due to the compound's lack of effect on Atf4-*firefly* % NPI in tunicamycin validation assay.

Figure 6.8: Representative data from validation assays.

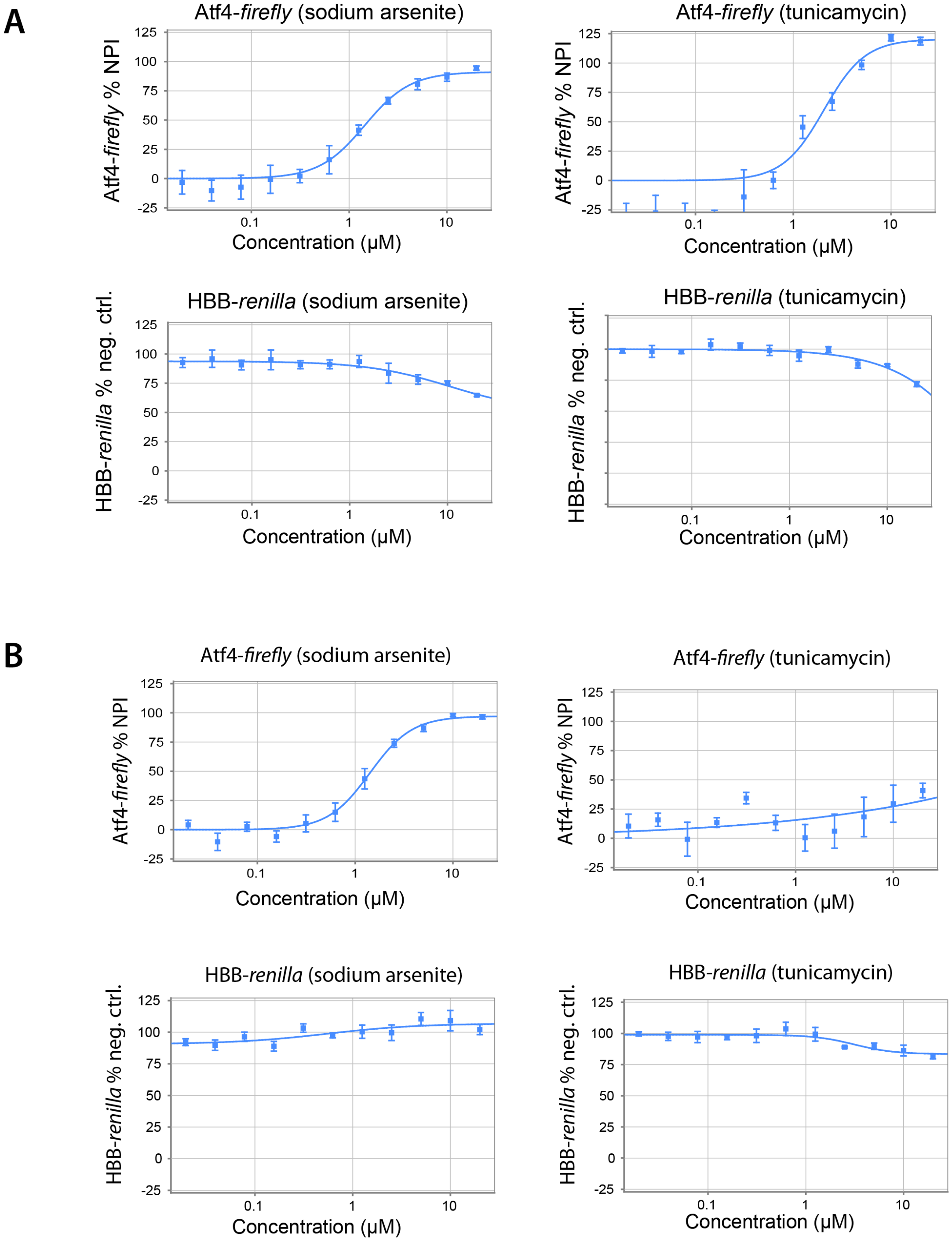

Discussion

I began this investigation into the integrated stress response with the hypothesis that the pathway would be oncogenic *in vivo*. By creating a primary SCC cell line with the entire pathway ablated, I was able to test this and other hypotheses in a direct manner **(for a summary of major findings and relations to published literature, see table 1 at the end of discussion).** The ISR turned out not to be required for tumor formation in this model, and in fact seemed to act as a tumor suppressor pathway, with ISR-null SCC cells forming tumors more easily at low cell numbers than controls. This is an important finding for the field because it conflicts with some, but not all, research into the pathway in cancer, and it highlights the complexity and potential for context specificity of this pathway in this disease. One particularly compelling and conflicting study used a mouse-genetics approach to ablate the pathway in lung adenocarcinoma cells and found that the ISR was oncogenic in this context (Ghaddar et al., 2021). The diverging results from this study and ours suggest the possibility that the pathway has different roles depending on the cancer type, and perhaps different roles at different times within the same cancer.

This is not necessarily surprising, because the ISR functions as a cellular decision maker during stress. The proteins that have been consistently identified as ISR targets include both proteins with a primarily adaptive role (Atf4, BiP) and also proteins with a role in inducing apoptosis (CHOP) (Pakos-Zebrucka et al., 2016). This has led to the conclusion in the field that the ISR is cytoprotective at low levels of pathway activation but promotes apoptosis when pathway activation is high or sustained for a certain amount of time (Ohoka et al., 2005). It is possible that different cell types within different microenvironments undergo different levels and kinetics of ISR activation which lead to the pathway having context specific tumor suppressive or oncogenic roles. Critical to better understanding this will be the development of better tools to measure ISR activity *in vivo*. This would include immunofluorescence-capable antibodies (p-eIF2α, Atf4) and fluorescent reporters, present versions of which have been unreliable in our hands.

Another open question relates to the diverging phenotypes of ISR-null and EIF2A KO cells (Sendoel et al., 2017). It was surprising to find that EIF2A, an effector of alternative translation, is required for tumorigenesis in this model, but p-eIF2α, the upstream activator of alternative translation, is not. I have two alternative hypotheses regarding this apparent paradox. One hypothesis is that there are other translational control pathways which could potentially activate EIF2A-driven translation, mTOR for instance. Another possibility is that it is different for a cell to have no ability to activate the ISR (eIF2α-S51A) verses a situation in which the pathway is allowed to become activated but alternative translation cannot be carried out (EIF2A KO). In this second scenario it is possible that p-eIF2α is switching the cell into a stress response with repressed housekeeping gene translation, but without EIF2A the cells are not translating these stress response proteins. I hypothesize that this situation may be more toxic to cancer cells than if the pathway was never activated in the first place, allowing translation of growth and housekeeping genes to continue.

In the course of characterizing the cancer phenotype of the ISR-null cell lines, I made a few surprising observations which became the focus of follow up work. First, I noticed that ISR-null SCC cells were slow or defective in multiple processes mediated by the cytoskeleton. This was most clearly evident in the multiple hour delay in cell spreading in ISR-null SCC cells compared to controls, which suggested the possibility of a previously undiscovered role for the ISR pathway in regulating the cytoskeleton. I also observed that ISR-null SCC cells were profoundly delayed in clearing protein aggregates. Even more intriguingly, I noticed that the process of clearing protein aggregates was accompanied by a major change in cell morphology in control cells, in which they unspread and became temporarily compact. The ISR-null cells on the other hand, became more flat, formed elongated processes connected to large focal adhesions, and become filled with cytosolic vacuoles.

Connecting these two findings I pursued the hypothesis that the ISR drives a cytoskeletal rearrangement to promote the clearance of protein aggregates. An important clue to the source of this potential connection was the finding that ISR-null cells failed to form the aggresome structure. The aggresome is a cytoprotective, non-membrane-bound organelle which forms on demand to sequester and catabolize protein aggregates (Johnston et al., 1998). Although there is more to learn about the regulation of this structure, it is appreciated that aggresome formation requires an intact microtubule cytoskeleton. Seeking the most simple explanation, which would be a single underlying mechanism regulating both the cytoskeleton and aggresome formation, I hypothesized that ISR-driven selective translation of cytoskeletal regulators could explain both of these findings.

Pursuing this hypothesis, ribosome profiling was performed with the goal of finding ISR-targets that could drive both the cytoskeletal differences and aggresome formation. I considered using this experiment to analyze the translatome during the stimuli of cell plating or bortezomib treatment. I chose to perform ribosome profiling following proteotoxic stress, however, because this was a more potent activator of ISR activity and led to an especially robust difference in cell morphology. When data was analyzed, I focused on ISR targets that fell into a family of cytoskeleton regulators, and I was excited to find a significantly enriched group of proteins within the centrosome. This was a promising finding, because it could potentially explain many of the results. For one, the centrosome is a major regulator of cell polarity (Musch, 2004), and ISR-null cells did not polarize as quickly as controls after plating. Moreover, the centrosome serves as the major microtubule organizing center within the cell, and is the site of aggresome formation following proteotoxic stress (Musch, 2004; Woodruff et al., 2017).

Consistent with this hypothesis was the finding that the MTOC increases in size during protein aggregate stress recovery at a timepoint that correlated with aggresome formation. Moreover, this effect was dependent upon the ISR. After confirming that intact microtubule dynamics are required for aggresome formation in our cells, I believe these results support the hypothesis that the ISR remodels or expands the MTOC in response to proteotoxic stress and that this effect is required for efficient recovery. Confirming this hypothesis will require further experiments targeting the specific ISR-regulated centrosomal proteins, knockdown and rescue experiments, for example. Results supporting this hypothesis would be a gene whose knockdown prevents aggresome formation in control cells and whose induced expression rescues aggresome formation in ISR-null cells.

Stepping back, questions arise regarding the significance of the ISR regulating both tumorigenesis and proteostasis. It has recently become appreciated that cancer incidence may anticorrelate with the incidence of neurodegenerative diseases. Alzheimer’s disease in particular has been repeatedly found to anticorrelate with cancer risk (Panegyres & Chen, 2021; Shi et al., 2015). Although the underlying causes of this relationship remain to be completely understood, some cellular pathways have been found to possess dual roles in cancer and proteostasis that may partially explain this effect. One pathway in particular, the heat-shock response, protects proteostasis in normal cells but is coopted by cancer cells for survival (Dai et al., 2007). Seminal work by Dr. Susan Lindquist and colleagues established that activity of HSF1, a master regulator of the heat shock response that drives transcription of a variety of cytoprotective chaperone proteins, is elevated in cancer, promoting cancer cell survival (Dai et al., 2007; Santagata et al., 2011). One could speculate that natural variation in the heat-shock response genes among individuals could thus play a role in the balance of neurodegeneration and cancer risk. For example, someone with higher HSF1 function may be less prone to neurodegenerative diseases such as Alzheimer's Disease, but then more prone to cancer. The dependency of cancer cells on the heat-shock response also suggests that dysregulated proteostasis may be an important hallmark of cancer cells.

This current study places the ISR alongside the heat-shock response as a pathway that regulates both cancer and proteostasis, albeit with a different pattern. In this case the ISR, which promotes proteostasis, also acts as a tumor suppressor pathway in SCC cells. This leads me to speculate that the ISR may play an important cellular role of balancing the oncogenic function of the proteostasis-promoting heat-shock response that becomes activated in cancer. That is, if proteotoxic stress is indeed an early hallmark of transformed cells, both the ISR and the heat-shock response may become simultaneously activated, and the ISR could play an important tumor-suppressive role to prevent oncogenesis in these cells with enhanced HSF1 activity.

Future work is required to better understand this relationship. A limitation of this study is that reagents to detect subtle changes in proteostasis *in vivo* are currently limited. Detecting ubiquitinated, unfolded proteins requires cell fractionation and isolation of aggregated proteins. This method requires a large amount of input material and is not suitable for analyzing the state of the proteome in cell populations *in vivo*. Other potential approaches could utilize immunofluorescence for anti-ubiquitin antibodies, or reagents that bind to fibrillar proteins such as the "proteostat" reagent (Enzo Life Sciences), but my initial attempts to use these reagents have been limited by high background that is difficult to differentiate from nonspecific signal. A biosensor approach could be an alternative, in which a cellular chaperone protein regulates the fluorescence of a fluorophore in a manner that is dependent upon the chaperone being bound to or free from certain cellular protein aggregates. Similar approaches have been used to analyze difficult to measure cellular processes such as the GTP/GDP-binding status of Rho proteins (Hodgson et al., 2010), but to my knowledge this approach has not been used to investigate the state of proteostasis in transformed cells.

Additionally intriguing future questions could tackle how the ISR restricts oncogenesis as well as how centrosomal function changes during proteotoxic challenges. As a stress-response pathway, the ISR can promote survival or apoptosis, depending on the intensity and duration of the stress (Pakos-Zebrucka et al., 2016). It is possible that proteotoxic challenges or other stresses are inducing apoptotic signals in transformed cells, explaining the tumor suppressive function. It is additionally possible that ISR activity promotes cell-cell adhesion in a way that promotes differentiation, thus restricting oncogenesis. This possibility is supported by the role of the ISR in cytoskeletal dynamics as well as the different morphologies of early, ISR-null tumors.

An additional open question raised by this work relate the state of the centrosome during proteotoxic stress. If the ISR is required to protect microtubule dynamics during stress, it is possible that unfolded proteins negatively impact the centrosome. Unfolded protein aggregates are known to sequester other cellular proteins, such as p62 and the disaggregase p97/VCP, contributing to their toxic role in cells (Donaldson et al., 2003; Olzscha et al., 2011; Yang et al., 2014). I hypothesize that unfolded proteins may also inhibit the function of centrosomal or pericentrosomal proteins, some of which are low-complexity proteins which may have affinity for such cellular aggregates (Woodruff et al., 2017). In fact one study found that proteotoxic stress does indeed inhibit centrosome function (Didier et al., 2008), perhaps highlighting the underlying challenge that the ISR has evolved to mitigate.

The second major goal of this project was to build a drug discovery platform with the goal of discovering ISR inhibitors, and specifically EIF2A inhibitors. These efforts pair with investigations of the basic biology of the pathway, because as we uncover more information about the function of this pathway in cancer and proteostasis, we can be better informed on how to advance potential novel compounds towards the most relevant disease processes. I focused my efforts on EIF2A based on our findings that this protein is required for oncogenesis, but I anticipate that new ISR-inhibitors could have a disease modifying role in a variety of disease processes.

Because the biochemical mechanisms of EIF2A's function are poorly understood, Dr. Sendoel and I designed a phenotypic screen to assay for EIF2A activity. The strength of this approach is that we could target this incompletely understood protein based on our understanding of its functional role in the stress response, but a weakness is that compounds identified as hits may target other proteins in the pathway. We set up the assay using an Atf4-driven firefly luciferase transgene, which we found to be a robust reporter of ISR activity. We employed a second reporter, HBB-*renilla* luciferase to report on housekeeping gene translation. When we performed a primary screen of over 50,000 compounds, we measured activity of both reporters, and we selected as hits the compounds that selectively inhibited stress-induced Atf4-FL translation without impacting HBB-RL, with the idea that this strategy would narrow in on compounds targeting downstream effectors of alternative translation (eg. EIF2A) rather than upstream regulators of ISR pathway activity (eg. Perk, eIF2B, etc.).

Using this approach, and in collaboration with the Tri-Institutional Drug Discovery Institute, we selected a list of hits which we further narrowed down with a second assay in which we induced stress with one of two stressors, sodium arsenite (as used in the primary screen and activates HRI) or tunicamycin (which induces ER stress and activates Perk, a different eIF2α kinase). I ran this assay with serial dilutions of our hits, and we selected our final list of hits based on the following characteristics: an inhibitory effect on the Atf4-*firefly* signal induced by both arsenite and tunicamycin, a plausible dose-response curves, and favorable drug-like characteristics as determined by a team of collaborating chemists. Using this criteria we narrowed down to a final hit list of 29 compounds.

Now, in collaboration with Drs. Ataman Sendoel and Nicola Guzzi, we will move forward with further phenotypic assays to understand how these compounds are functioning in the stress response, and EIF2A KO cells will be used to make sure that the compounds are not having the same ISR-inhibiting effects in cells lacking the target. Long term goals include demonstrating drug binding to EIF2A, developing a biochemical EIF2A activity assay, and performing structure-activity relationship experiments using modified compounds. If this effort succeeds in identifying EIF2A inhibiting compounds, the lab will be well poised to evaluate the effect of these compounds on an SCC tumor model which we know relies on EIF2A for function.

Finally, although the screen was not focused on compounds that stimulate the ISR, I did identify compounds that seemed to boost ISR activity during stress. It would be interesting to see how these putative ISR-potentiators influence proteostasis. Because loss of ISR activity impairs the recovery of proteostasis, it is possible that boosting ISR activity could improve proteostasis. As this work has focused on both improving our understanding of ISR biology as well as our ability to manipulate it with drugs, an exciting future direction would be to gradually build towards an arsenal of ISR-inhibitors and potentiators which could be used for different disease conditions. Perhaps on the one hand an EIF2A inhibitor could be useful for treating certain cancers, and a ISR-potentiating compound could improve proteostasis in diseases like Parkinson's Disease which have their root in the buildup of toxic, cytoplasmic protein aggregates. I hope that the results presented in this dissertation lay groundwork for both a better understanding of the ISR in human health and disease as well as an improved ability to manipulate the pathway for therapeutic benefit.

Table 1: Summary of major findings and relation to published literature.

Finding	Figures	Contribution	Citations (if applicable)
ISR-null cells proliferate normally in culture.	1.4	Replicates previous finding	(Scheuner et al, 2001)
ISR-null cells cannot shut down translation in response to stress.	1.5	Replicates previous finding	(Scheuner et al, 2001)
ISR-null cells cannot form stress-granules following sodium arsenite treatment.	1.5	Replicates previous finding	(Buchan & Parker, 2009; Sidrauski et al., 2015)
ISR-null cells are more sensitive to ER-stress than controls.	1.5	Replicates previous finding	(Scheuner et al, 2001; Salaroglio et al., 2017).
The ISR acts as a tumor suppressor upon SCC tumorigenesis, but ISR-null tumors appear similar to controls later on.	2.1-2.3	Contradicts finding in different cancer model	(Ghaddar et al., 2021; Nguyen et al., 2018)
ISRIB has minimal effect on SCC growth.	2.4	Contradicts finding in different cancer model	(Nguyen et al., 2018)
ISR-null cells are delayed in motility (spreading, establishment of polarity, and formation of epithelial sheet).	3.1-3.3	Novel finding	
The ISR is required for clearing protein aggregates.	4.1-4.5	Extends previous finding	(Abdel-Nour et al., 2019)
HRI responds to protein aggregates.	4.6	Replicates previous finding	(Abdel-Nour et al., 2019)
ISR-null cells do not efficiently form the aggresome.	4.7-4.8	Novel finding	

Finding	Figures	Contribution	Citations (if applicable)
Recovery from protein aggregate stress is accompanied by a change in cell morphology that is ISR-dependent.	4.9	Novel finding	
ISR-null cells with protein aggregates lose migratory capacity.	4.10	Novel finding	
The ISR targets the translation of centrosomal proteins as a response to proteotoxic stress.	5.1-5.4	Novel finding	
The aggresome forms at the centrosomal microtubule organizing center.	5.5	Replicates previous finding	(Johnston, J. A et al., 1998)
The ISR drives an increase in centrosome size in response to proteotoxic stress.	5.6-5.7	Novel finding	
Microtubule dynamics are required for aggresome formation.	5.8	Replicates previous finding	(Johnston, J. A et al., 1998)

Materials and methods

CRISPR cloning

Lentiviral particles containing the gene replacement construct, pLKO-PGK-eIF2α-mycTag-P2A-NeoR were prepared by transfecting the lentiviral plasmid along with packaging plasmids into HEK293T cells, and viral supernatant was collected 48 hours post transfection. This construct was integrated into the genome of a clonal, parental primary SCC mouse line by incubating 100 μL with 0.1 mg/mL polybrene for 8 hours. 48 hours later cells with the integrated construct were selected with 0.5 mg/mL Neomycin selection for 2 days. Following selection the endogenous allele was targeted for deletion using CRISPR-Cas9 RNP particles. The replacement allele had a synonymous mutation in the PAM site rendering it resistant to this CRIPSR construct. CRISPR-Cas9 RNP particles targeting the endogenous allele were prepared as follows: eIF2α gRNA (target sequence: ATATTCCAACAAGCTGACAT) was designed using Guidescan software (Perez et al., 2017) and complexed with ATTO550-tracrRNA and Cas9. All reagents were acquired from IDTdna's "AltR system". Duplexed gRNA:tracrRNA was prepared by mixing 1 μM of each component in IDTdna duplex buffer, heated to 95° C in a thermocycler and annealed by gradually lowering the temperature to 25° C at a rate of 0.1° C/second. Duplexed gRNA:tracrRNA was complexed with Cas9 by mixing 1 μM of the duplex with 1 μM Cas9 in OptiMEM (ThermoFisher) and incubating at room temperature for 5 minutes.

RNP complexes then were transfected into 60% confluent 12 well plates using RNAiMAX as follows: 30 μL of 1 μM RNP complexes were mixed with 4.8 μL RNAiMAX in 335 μL of optiMEM and RNP-lipid complexes were allowed to form for 15 minutes at room temperature. At the end of the incubation 400 µL of complexes were added dropwise to cells, and media was changed 16 hours later. 48 hours after transfection single cells were isolated using fluorescence activated cell sorting (FACS) as follows: Cells were dissociated with trypsin (Gibco) and resuspended in 500 µL of FACS buffer (PBS supplemented with 5% FBS and 5 uM EDTA), and single, ATTO-550 positive cells were sorted using BD FACSAria cell sorter into wells of 96-well plates containing 100 µL of 50-50 mixture of fresh media and conditioned media. Clones that grew to confluency were transferred to 12 well plates, and following growth to confluency in 12 well plates, cells were dissociated with trypsin and frozen in freezing media supplemented with 10% FBS and 10% DMSO. At this stage a small aliquot of cells (75% of the plate) was lysed in 200 µL of QuickExtract DNA Extraction solution (Lucigen) and gDNA was prepared by heating to 65° C for 10 minutes followed by heat inactivation at 95° C for 2 minutes. These gDNA samples were used for further analysis. For HRI KO cells the protocol was exactly the same except that gRNA targeting HRI (target seq: ATTTAAACACCTGTTTGGAG) was used.

Cell culture

Primary murine SCC cells were generated and cultured in E medium supplemented with 15% FBS and 50 mM CaCl2 as previously described (Yang et al., 2015). Cells were passaged 3 times per week and passage numbers were maintained counting from the point of cell line generation. Frozen cell stocks were generated by freezing cells in complete media supplemented with 10% additional FBS and 10% DMSO.

NGS analysis of CRISPR outcomes

Knockout of the endogenous allele was evaluated using primers targeting a 300 basepair region of genomic DNA with the targeted locus in the middle of the amplicon. Primers had 5' overhangs with sequences compatible with the Illumina Nextera XT index primers (R: overhang: GTCTCGTGGGCTCGGAGATGTGTATAAGAGACAG, L overhang: TCGTCGGCAGCGTCAGATGTGTATAAGAGACAG). Amplicons were generated with 1 µL of input gDNA and the NEB phusion kit according to manufacturer's instructions, and amplicons were isolated using Agencout Ampure XP beads (Beckman Coulter). A second barcoding PCR was performed using Nextera XT index primers as follows: 2 µL of cleaned amplicons were used as input, primers were added so that each isolated clone had a unique combination of left and right barcodes, and barcodes were added using a 8 cycle PCR reaction with 55° C annealing temp, again with the NEB Phusion kit, and the barcoded amplicons were cleaned and primer dimers were removed using Ampure XP beads. Amplicons were normalized to the same concentration, pooled, and sequenced using a single Illumina MiSeq Nano lane using the 250 basepair, paired end kit. Demultiplexed reads were analyzed and screened for indels using the RGEN Cas Analyzer (http://www.rgenome.net). A KO clone was confirmed if the only reads detected in that sample were indels that would create a frameshift.

Western blotting

Cells were lysed with RIPA (20 mM Tris- HCl, pH 8.0, 150 mM NaCl, 1 mM EDTA, 1 mM EGTA, 1% Triton X-100, 0.5% deoxycorate, 0.1% SDS) containing protease inhibitors (Complete mini, Roche) and phosphatase inhibitors (PhosStop). Lysates were clarified by centrifugation and protein concentration of supernatants was evaluated using BCA assay (Pierce). Protein lysates were normalized, mixed with LDS (ThermoFisher) and β-mercaptoethanol (Thermofisher), and denatured at 95° C for 5 minutes. Protein was separated by gel electrophoresis using 4–12% or 12% NuPAGE Bis-Tris gradient gels (Life Technologies) and transferred to nitrocellulose membranes (GE Healthcare, 0.45 μm). Membranes were blocked with 2% BSA in TBS supplemented with 0.1% Tween 20, and primary antibodies were stained overnight in blocking buffer at 4° C or overnight at room temperature, and HRP-conjugated secondary antibodies were stained for 1 hour at room temperature. Membranes were washed and then incubated with ECL plus chemiluminescent reagent (Pierce) for 30 seconds. Chemiluminescent signal was evaluated using CL-XPosure Film (ThermoFisher).

Proliferation and cell viability assays

For proliferation assays 2500-5000 cells were plated per well in clear-bottom, black optical 96 well plates (Nunc) and allowed to attach overnight. A baseline plate was collected the next day as a zero hour sample, and then plates were collected at 24, 48, and 72 hours after this timepoint. At the time of collection media was washed and cells were fixed in 4% PFA in PBS for 10 minutes at room temperature. After fixation, PFA was washed with PBS and cells were stored in PBS at 4° C until the end of the experiment. Following collection of the final plate, nuclei were stained in all samples using 1 ug/mL DAPI in PBS for 5 minutes at room temperature. DAPI was washed and replaced with PBS, and nuclei were imaged on a Biotek Cytation 5 high content imager, and cells were counted using Gen5 software.

Cell viability was measured with Promega Cell Titer Glo as follows. 5000-10000 cells were plated in each well of white, opaque bottom 96 well plates (Nunc) and allowed to attach overnight. Cells were treated with compounds the following day and with serial dilutions of bortezomib or tunicamycin (both acquired from Millipore Sigma) and incubated for 24 and 48 hours, respectively. At the end of drug treatment, media was washed and replaced with 75 µL of fresh media. 75 µL of cell titer glo buffer and substrate were mixed into wells and the plate was incubated at room temperature for 10 minutes. Luminescence was measured on a Biotek Cytation 5 high content imager, and percent cell viability was calculated by normalizing sample luminescence to an untreated sample.

Measurement of translation rates

Cells were plated to 75% confluency in clear-bottom, black optical 96 well plates (Nunc) and allowed to attach overnight. The next day cells were treated with sodium arsenite, ISRIB, or a combination, and incubated at 37° C for 15 minutes. At this time 20 µM OP-puromycin was supplemented to the media, and cells were incubated for 30 more minutes. Cells were then fixed in 4% PFA in PBS for 10 minutes at room temperature, permeabilized in 0.3% triton X-100 in PBS for 10 minutes, blocked in 3% BSA in PBS for 30 minutes, and OP-puromycin was conjugated to alexafluor 647-azide per manufacturers instructions (ThermoFisher). Following click-it reaction, cells were washed and 1 µg/mL DAPI was added as a counter stain. Cells were washed, placed in PBS, and cellular fluorescence was measured on a Biotek Cytation 5 high content imager. Mean cellular fluorescence was calculated in Gen5 software.

Tumor allografting

Squamous cell carcinoma allografts were generated by intradermally injecting 1e5 SCC cells suspended in a 50:50 mix of PBS and growth-factor reduced Matrigel (Corning, 356231) in an injection volume of 50 µL. Grafts were generated in the flanks of 6-8 week old female nude mice. Tumor dimensions were measured every 5 days using electronic calipers and tumor volume was calculated using the formula V = 0.5 × length × width2. For limiting-dilution assays, 1e2, 1e3, 1e4, or 1e5 cells were implanted in a 50 µL injection volume and tumors were allowed to form for 4 weeks. Tumor formation was assessed by visually inspecting injection sites for neoplastic growth, and tumor-initiating cell frequency was estimated using extreme limiting-dilution analysis (Hu & Smyth, 2009).

Immunofluorescence/histology

For immunofluorescence of tumors, samples were fixed in 4% PFA for 1 hour at room temperature , dehydrated in 30% sucrose overnight at 4 C, and mounted into OCT blocks and frozen. 14 µm thick sections were cut using a Leica cryostat deposited onto SuperFrost Plus slides (VWR). For immunofluorescence of cells in culture, samples were fixed with 4% PFA for 10 minutes at room temperature. Samples were permeabilized with 0.3% Triton-X100 in PBS and blocked using 2.5% normal donkey serum, 2.5% normal goat serum, 1% BSA, 2% fish gelatin, and 0.3% Triton X-100 in PBS. Primary antibodies were applied in blocking buffer overnight at 4° C. Samples were washed with 0.1% Triton X-100 and secondary antibodies with Alexa 488, Alexa 594, and Alexa 647 were applied for 1 hour at room temperature in blocking buffer containing 1 µg/mL DAPI. Slides were washed with 0.1% triton and mounted using Prolong Diamond Antifade Mountant with

DAPI (ThermoFisher). For histology samples were fixed in 4% PFA overnight at 4 C, and then samples were dehydrated with sequential washes in 70%, 80%, 90% and 100% ethanol. Samples in 100% ethanol were submitted to Histowiz for mounting, sectioning, H&E staining, and imaging.

Microscopy and image analysis

Microscopy of tumors and 40X images of aggresomes and spreading cells were performed using an Axio Observer Z1 epifluorescence microscope equipped with a Hamamatsu ORCA-ER camera (Hamamatsu Photonics), and with an ApoTome.2 (Carl Zeiss) slider using a 20X air, 40X oil, or 63X oil objective. 63X confocal microscopy images were collected on an Andor Dragonfly spinning disk imaging system with a Leica DMi8 Stand and cMOS Zyla camera. Images were analyzed in FIJI or Imaris. For fluorescence intensity measurements of tumors GFP masks were generated and signal was measured within the mask. Aggresomes were manually counted as discrete p62-positive juxtanuclear puncta on maximum intensity Z-projections. Cell dimensions were calculated using the length measuring tool, and cell spreading was evaluated manually by observing for spread morphology. RGB images were generated with FIJI and saved as TIFF files. For 3-dimensional reconstructions and volumetric analyses of microtubule organizing centers, Imaris was used to generate 3D images, and volumes were generated to create 3D volumes encompassing the discrete puncta of pericentrin staining. Volume as well as summed pericentrin and γ-tubulin fluorescence intensity were measured within these volumes

Cell fractionation

Cells were lysed in RIPA buffer (20 mM Tris- HCl, pH 8.0, 150 mM NaCl, 1 mM EDTA, 1 mM EGTA, 1% Triton X-100, 0.5% deoxycorate, 0.1% SDS) containing protease inhibitors (Complete mini, Roche) and phosphatase inhibitors (PhosStop), and lysed for 10 minutes at room temperature. Membrane fraction was pelleted by centrifuging at 1000 xg for 10 minutes at 4° C. The supernatant (cytosolic fraction) was transferred to new tubes which were centrifuged at 20,000 xg for 30 minutes at 4° C. The supernatant (RIPA-soluble fraction was transferred to a new tube, and the pellets (RIPA-insoluble fractions) were washed with 300 µL of RIPA buffer, centrifuged 20,000 xg for 10 minutes at 4° C, and then resuspended in 30 µL of 1X LDS-βME by vortexing vigorously and boiling at 98° C for 10 minutes. The protein concentration of the RIPA-soluble fraction was measured with a BCA assay (Pierce). RIPA-soluble fractions were mixed into 1X LDS-βME and protein concentration was normalized. The insoluble fractions were normalized by adding 1X LDS-BMe so that the same volume corresponds to the same volume of insoluble-fraction lysate (eg. Insoluble fraction from 100 ug of cell lysate). Samples were run on western blots as previously described and probed for ubiquitin signal.

Antibodies and counterstains

The following antibodies and dilutions were used for western blotting. 1/1000 β-Actin (Cell Signaling Technologies, 3700); 1/1000 p-eIF2α (Invitrogen, 44-728G); 1/5000 p-eIF2α (Cell Signaling Technologies, 3597); 1/1000 p62/SQSTM (Cell Signaling Technologies, 5114); 1/1000 Atf4 (Cell Signaling Technologies, 11815); 1/1000 ubiquitin (Cell Signaling Technologies, 3393S); 1/1000 K48-linked polyubiquitin (Cell Signaling Technologies, 8081); 1/1000 Myc-tag (Abcam, ab32); 1/5000 α-tubulin (Millipore Sigma, T5168). For immunofluorescence the following antibodies and dilutions were used. 1/500 α6-integrin (BD Bioscience, 555734); 1/500 GFP (Abcam, ab13970); 1/500 E-Cadherin (Cell Signaling Technologies, 3195); 1/100 G3BP (BD Bioscience 611126); 1/500 Vinculin (Millipore Sigma, V9131); 1/100 Phospho-Myosin Light Chain 2 (Ser19) (Cell Signaling Technologies, 3675); 1/250 p62/SQSTM (Cell Signaling Technologies, 7695); 1/500 LaminB1 (Santa Cruz, 374015); 1/500 α-tubulin (BD Biosciences, MCA77G); 1/500 γ-tubulin (Millipore Sigma, T6557); 1/250 Pericentrin (Abcam, ab4448). Nuclei were counterstained with 1 μg/mL DAPI (ThermoFisher) and F-Actin was stained with 1/400 Rhodamine or AlexaFluor-488-conjugated phalloidin (ThermoFisher).

Electron microscopy

Cells were fixed in a solution containing 4% PFA, 2% glutaraldehyde, and 2 mM CaCl2 in 0.1 M sodium cacadylate buffer (pH 7.2) for 1 hour at room temperature, and then placed at 4° C. Cells were next postfixed in 1% osium tetroxide and processed for Epon embedding; ultrathin sections (60-65 nm) were then counterstained with uranyl acetate and lead citrate, and images were acquired using a Tacnai G2-12 transmission electron microscope equipped with an AMT BioSprint29 digital camera.

Ribosome profiling and analysis

To perform ribosome profiling we closely followed the a recently published protocol (McGlincy & Ingolia, 2017). In short cells were lysed in polysome buffer supplemented with 0.1 mg/mL cyclohexamide. Lysates were treated with 500 U of RNAse I (Epicentre) per 25 µg of RNA (quantified by Qubit fluorimetry – ThermoFisher), and ribosome protected fragments were isolated using sephacryl S400 columns (GE Healthcare) in TE buffer. Ribosomes and ribosome protected fragments (RPFs) were dissociated in Trizol (Invitrogen) and RNA was collected with protected fragments were purified using Zymo Research DirectZol MiniPrep columns. RPFs were purified by running total RNA on a 15 % TBE-Urea gel (ThermoFisher) and cutting the region corresponding to 17 to 34 nucleotides. RNA was purified and precipitated, dephosphorylated with PNK (NEB), and ligated to preadenylated barcoded linker oligonucleotides, and then unligated linker was digested away with 25 U Yeast 5’-deadenylase (NEB) and 5 U RecJ exonuclease (Epicentre). Up to 8 libraries were pooled, and rRNA was depleted using the Lexogen Ribocop V2 kit, and reverse transcription of RPF-linker fragments was performed in presence of 20U Superase-IN (Invitrogen) and 200U Protoscript II (NEB). cDNAs were circularized using 100U CircLigase I ssDNA ligase (Epicentre), and cDNA concentration was quantified by QPCR of cDNA compared to a standard curve of a reference sample. Libraries were amplified with Illumina-compatible barcoded primers and a 10 cycle PCR. DNA of the correct size (~160 bp) was isolated on TBE-PAGE gel, precipitated, and resuspended in TE buffer. Total mRNA samples were prepared in parallel, and mRNA was selected by rRNA depletion, and libraries were prepared using Illumina Ribozero kit.

Ribosome profiling and total RNA libraries were pooled and sequenced on a Novaseq using the S1, 1x100 bp kit. Reads were demultiplexed, trimmed using FastX trimmer, and aligned to the mm10 reference genome using bowtie2. Sequences were counted in bins of 5’ UTR, CDS, and 3’ UTR as defined using plastid (https://plastid.readthedocs.io/en/latest/) . Count data was analyzed using DESeq2 (Love et al., 2014), an R package designed for statistical analysis of gene counts generated from Illumina-based sequencing. For expression analysis of ribosome profiling data only reads in the CDS were included and reads coming from the first 15 codons (45bp) and last 5 codons (15bp) were excluded. Additionally, only reads of size between 20-23bp or 26-32bp were counted. Gene lists were generated as described in the main text, first by filtering genes with significant differences in RPF-read counts, and then genes that changed specifically at the translation level were identified as the subset of filtered genes with translational efficiency (TE=normalized RPF/normalized total RNA) fold changes greater than 1.5.

EIF2A reporter assay

Lentivirus was used to transduce primary SCC cells were transduced with the Atf4-firefly/HBB-renilla dual reporter. Cells were selected with 0.5 mg/mL Neomycin for 5 days. Clones were generated using FACS as previously described. After selecting the clone with the highest induction of Atf4-firefly upon stress, EIF2A-reporter assays were performed as follows. Cells were plated in 96 or 384 well plates with 15,000 or 8,000 cells per well, respectively. Cells were allowed to attach overnight, and stress was induced using 30 μM sodium arsenite or 100 ng/mL tunicamycin. 7 hours later reporter activity was evaluated using Promega dual-glo kit following manufacturer’s instructions. Briefly, firefly luciferase detection reagent and lysis buffer was added to wells, cells were lysed and incubated at room temperature for 15 minutes, and luminescence was read on a Biotek Cytation 5 plate reader. Then a buffer to inactivate firefly luciferase and activate renilla luciferase was added, the plate was again incubated for 15 minutes and luminescence was read on a plate reader.

High-throughput screening

Compounds from Rockefeller University’s high-throughput screening library were added to wells of 384 well plates containing 10 µL of media. 8000 cells per well were then added in 10 µL, giving a final compound concentration of 10 µM. The following day sodium arsenite was added in 5 uL of media for a final concentration of 30 uM. 7 hours later the dual glo assay was performed as described above. All liquids were dispensed using Multidrop (ThermoFisher), and luminescence was evaluated using a Biotek Synergy Neo2 plate reader.

References

Abdel-Nour, M., Carneiro, L. A. M., Downey, J., Tsalikis, J., Outlioua, A., Prescott, D., Da Costa, L. S., Hovingh, E. S., Farahvash, A., Gaudet, R. G., Molinaro, R., van Dalen, R., Lau, C. C. Y., Azimi, F. C., Escalante, N. K., Trotman-Grant, A., Lee, J. E., Gray-Owen, S. D., Divangahi, M., Chen, J. J., Philpott, D. J., Arnoult, D., & Girardin, S. E. (2019). The heme-regulated inhibitor is a cytosolic sensor of protein misfolding that controls innate immune signaling. *Science*, *365*(6448). https://doi.org/10.1126/science.aaw4144

Al-Hajj, M., Wicha, M. S., Benito-Hernandez, A., Morrison, S. J., & Clarke, M. F. (2003). Prospective identification of tumorigenic breast cancer cells. *Proc Natl Acad Sci U S A*, *100*(7), 3983-3988. https://doi.org/10.1073/pnas.0530291100

Alberts, B. (2015). *Molecular biology of the cell* (Sixth edition. ed.). Garland Science, Taylor and Francis Group.

Anand, A., Sharma, A., Ravins, M., Biswas, D., Ambalavanan, P., Lim, K. X. Z., Tan, R. Y. M., Johri, A. K., Tirosh, B., & Hanski, E. (2021). Unfolded protein response inhibitors cure group A streptococcal necrotizing fasciitis by modulating host asparagine. *Sci Transl Med*, *13*(605). https://doi.org/10.1126/scitranslmed.abd7465

Armstrong, R. A., Lantos, P. L., & Cairns, N. J. (2001). Spatial correlations between the vacuolation, prion protein deposits, and surviving neurons in the cerebral cortex in sporadic Creutzfeldt-Jakob disease. *Neuropathology*, *21*(4), 266-271. https://doi.org/10.1046/j.1440-1789.2001.00406.x

Ashraf, G. M., Greig, N. H., Khan, T. A., Hassan, I., Tabrez, S., Shakil, S., Sheikh, I. A., Zaidi, S. K., Akram, M., Jabir, N. R., Firoz, C. K., Naeem, A., Alhazza, I. M., Damanhouri, G. A., & Kamal, M. A. (2014). Protein misfolding and aggregation in Alzheimer's disease and type 2 diabetes mellitus. *CNS Neurol Disord Drug Targets*, *13*(7), 1280-1293. https://doi.org/10.2174/1871527313666140917095514

Back, S. H., Scheuner, D., Han, J., Song, B., Ribick, M., Wang, J., Gildersleeve, R. D., Pennathur, S., & Kaufman, R. J. (2009). Translation attenuation through eIF2alpha phosphorylation prevents oxidative stress and maintains the differentiated state in beta cells. *Cell Metab*, *10*(1), 13-26. https://doi.org/10.1016/j.cmet.2009.06.002

Bence, N. F., Sampat, R. M., & Kopito, R. R. (2001). Impairment of the ubiquitin-proteasome system by protein aggregation. *Science*, *292*(5521), 1552-1555. https://doi.org/10.1126/science.292.5521.1552

Berlanga, J. J., Herrero, S., & de Haro, C. (1998). Characterization of the hemin-sensitive eukaryotic initiation factor 2alpha kinase from mouse nonerythroid cells. *J Biol Chem*, *273*(48), 32340-32346. https://doi.org/10.1074/jbc.273.48.32340

Bian, Y., Terse, A., Du, J., Hall, B., Molinolo, A., Zhang, P., Chen, W., Flanders, K. C., Gutkind, J. S., Wakefield, L. M., & Kulkarni, A. B. (2009). Progressive tumor formation in mice with conditional deletion of TGF-beta signaling in head and neck epithelia is associated with activation of the PI3K/Akt pathway. *Cancer Res*, *69*(14), 5918-5926. https://doi.org/10.1158/0008-5472.CAN-08-4623

Bjorkoy, G., Lamark, T., Brech, A., Outzen, H., Perander, M., Overvatn, A., Stenmark, H., & Johansen, T. (2005). p62/SQSTM1 forms protein aggregates degraded by autophagy and has a protective effect on huntingtin-induced cell death. *J Cell Biol*, *171*(4), 603-614. https://doi.org/10.1083/jcb.200507002

Borghi, N., Sorokina, M., Shcherbakova, O. G., Weis, W. I., Pruitt, B. L., Nelson, W. J., & Dunn, A. R. (2012). E-cadherin is under constitutive actomyosin-generated tension that is increased at cell-cell contacts upon externally applied stretch. *Proc Natl Acad Sci U S A*, *109*(31), 12568-12573. https://doi.org/10.1073/pnas.1204390109

Buchan, J. R., & Parker, R. (2009). Eukaryotic stress granules: the ins and outs of translation. *Mol Cell*, *36*(6), 932-941. https://doi.org/10.1016/j.molcel.2009.11.020

Buckley, C. D., Tan, J., Anderson, K. L., Hanein, D., Volkmann, N., Weis, W. I., Nelson, W. J., & Dunn, A. R. (2014). Cell adhesion. The minimal cadherin-catenin complex binds to actin filaments under force. *Science*, *346*(6209), 1254211. https://doi.org/10.1126/science.1254211

Caviston, J. P., & Holzbaur, E. L. (2006). Microtubule motors at the intersection of trafficking and transport. *Trends Cell Biol*, *16*(10), 530-537. https://doi.org/10.1016/j.tcb.2006.08.002

Chen, X., Mitsutake, N., LaPerle, K., Akeno, N., Zanzonico, P., Longo, V. A., Mitsutake, S., Kimura, E. T., Geiger, H., Santos, E., Wendel, H. G., Franco, A., Knauf, J. A., & Fagin, J. A. (2009). Endogenous expression of Hras(G12V) induces developmental defects and neoplasms with copy number imbalances of the oncogene. *Proc Natl Acad Sci U S A*, *106*(19), 7979-7984. https://doi.org/10.1073/pnas.0900343106

Ching, J. K., Elizabeth, S. V., Ju, J. S., Lusk, C., Pittman, S. K., & Weihl, C. C. (2013). mTOR dysfunction contributes to vacuolar pathology and weakness in valosin-containing protein associated inclusion body myopathy. *Hum Mol Genet*, *22*(6), 1167-1179. https://doi.org/10.1093/hmg/dds524

Chou, A., Krukowski, K., Jopson, T., Zhu, P. J., Costa-Mattioli, M., Walter, P., & Rosi, S. (2017). Inhibition of the integrated stress response reverses cognitive deficits after traumatic brain injury. *Proc Natl Acad Sci U S A*, *114*(31), E6420-E6426. https://doi.org/10.1073/pnas.1707661114

Costa-Mattioli, M., Gobert, D., Harding, H., Herdy, B., Azzi, M., Bruno, M., Bidinosti, M., Ben Mamou, C., Marcinkiewicz, E., Yoshida, M., Imataka, H., Cuello, A. C., Seidah, N., Sossin, W., Lacaille, J. C., Ron, D., Nader, K., & Sonenberg, N. (2005). Translational control of hippocampal synaptic plasticity and memory by the eIF2alpha kinase GCN2. *Nature*, *436*(7054), 1166-1173. https://doi.org/10.1038/nature03897

Costa-Mattioli, M., Gobert, D., Stern, E., Gamache, K., Colina, R., Cuello, C., Sossin, W., Kaufman, R., Pelletier, J., Rosenblum, K., Krnjevic, K., Lacaille, J. C., Nader, K., & Sonenberg, N. (2007). eIF2alpha phosphorylation bidirectionally regulates the switch from short- to long-term synaptic plasticity and memory. *Cell*, *129*(1), 195-206. https://doi.org/10.1016/j.cell.2007.01.050

Costa-Mattioli, M., & Walter, P. (2020). The integrated stress response: From mechanism to disease. *Science*, *368*(6489). https://doi.org/10.1126/science.aat5314

Dai, C., Whitesell, L., Rogers, A. B., & Lindquist, S. (2007). Heat shock factor 1 is a powerful multifaceted modifier of carcinogenesis. *Cell*, *130*(6), 1005-1018. https://doi.org/10.1016/j.cell.2007.07.020

Davoli, T., & de Lange, T. (2011). The causes and consequences of polyploidy in normal development and cancer. *Annu Rev Cell Dev Biol*, *27*, 585-610. https://doi.org/10.1146/annurev-cellbio-092910-154234

Dechecchi, M. C., Tamanini, A., & Cabrini, G. (2018). Molecular basis of cystic fibrosis: from bench to bedside. *Ann Transl Med*, *6*(17), 334. https://doi.org/10.21037/atm.2018.06.48

Dever, T. E., Feng, L., Wek, R. C., Cigan, A. M., Donahue, T. F., & Hinnebusch, A. G. (1992). Phosphorylation of initiation factor 2 alpha by protein kinase GCN2 mediates gene-specific translational control of GCN4 in yeast. *Cell*, *68*(3), 585-596. https://doi.org/10.1016/0092-8674(92)90193-g

Didier, C., Merdes, A., Gairin, J. E., & Jabrane-Ferrat, N. (2008). Inhibition of proteasome activity impairs centrosome-dependent microtubule nucleation and organization. *Mol Biol Cell*, *19*(3), 1220-1229. https://doi.org/10.1091/mbc.e06-12-1140

DiNapoli, S. E., Martinez-McFaline, R., Gribbin, C. K., Wrighton, P. J., Balgobin, C. A., Nelson, I., Leonard, A., Maskin, C. R., Shwartz, A., Quenzer, E. D., Mailhiot, D., Kao, C., McConnell, S. C., de Jong, J. L. O., Goessling, W., & Houvras, Y. (2020). Synthetic

CRISPR/Cas9 reagents facilitate genome editing and homology directed repair. *Nucleic Acids Res*, *48*(7), e38. https://doi.org/10.1093/nar/gkaa085

Donaldson, K. M., Li, W., Ching, K. A., Batalov, S., Tsai, C. C., & Joazeiro, C. A. (2003). Ubiquitin-mediated sequestration of normal cellular proteins into polyglutamine aggregates. *Proc Natl Acad Sci U S A*, *100*(15), 8892-8897. https://doi.org/10.1073/pnas.1530212100

Doudna, J. A., & Charpentier, E. (2014). Genome editing. The new frontier of genome engineering with CRISPR-Cas9. *Science*, *346*(6213), 1258096. https://doi.org/10.1126/science.1258096

Faustino-Rocha, A., Oliveira, P. A., Pinho-Oliveira, J., Teixeira-Guedes, C., Soares-Maia, R., da Costa, R. G., Colaco, B., Pires, M. J., Colaco, J., Ferreira, R., & Ginja, M. (2013). Estimation of rat mammary tumor volume using caliper and ultrasonography measurements. *Lab Anim (NY)*, *42*(6), 217-224. https://doi.org/10.1038/laban.254

Fiore, V. F., Krajnc, M., Quiroz, F. G., Levorse, J., Pasolli, H. A., Shvartsman, S. Y., & Fuchs, E. (2020). Mechanics of a multilayer epithelium instruct tumour architecture and function. *Nature*, *585*(7825), 433-439. https://doi.org/10.1038/s41586-020-2695-9

Garcin, C., & Straube, A. (2019). Microtubules in cell migration. *Essays Biochem*, *63*(5), 509-520. https://doi.org/10.1042/EBC20190016

Ghaddar, N., Wang, S., Woodvine, B., Krishnamoorthy, J., van Hoef, V., Darini, C., Kazimierczak, U., Ah-Son, N., Popper, H., Johnson, M., Officer, L., Teodosio, A., Broggini, M., Mann, K. K., Hatzoglou, M., Topisirovic, I., Larsson, O., Le Quesne, J., & Koromilas, A. E. (2021). The integrated stress response is tumorigenic and constitutes a therapeutic liability in KRAS-driven lung cancer. *Nat Commun*, *12*(1), 4651. https://doi.org/10.1038/s41467-021-24661-0

Giannone, G., Dubin-Thaler, B. J., Dobereiner, H. G., Kieffer, N., Bresnick, A. R., & Sheetz, M. P. (2004). Periodic lamellipodial contractions correlate with rearward actin waves. *Cell*, *116*(3), 431-443. https://doi.org/10.1016/s0092-8674(04)00058-3

Guasch, G., Schober, M., Pasolli, H. A., Conn, E. B., Polak, L., & Fuchs, E. (2007). Loss of TGFbeta signaling destabilizes homeostasis and promotes squamous cell carcinomas in stratified epithelia. *Cancer Cell*, *12*(4), 313-327. https://doi.org/10.1016/j.ccr.2007.08.020

Gupton, S. L., & Waterman-Storer, C. M. (2006). Spatiotemporal feedback between actomyosin and focal-adhesion systems optimizes rapid cell migration. *Cell*, *125*(7), 1361-1374. https://doi.org/10.1016/j.cell.2006.05.029

Halbleib, J. M., & Nelson, W. J. (2006). Cadherins in development: cell adhesion, sorting, and tissue morphogenesis. *Genes Dev*, *20*(23), 3199-3214. https://doi.org/10.1101/gad.1486806

Hanahan, D., & Weinberg, R. A. (2000). The hallmarks of cancer. *Cell*, *100*(1), 57-70. https://doi.org/10.1016/s0092-8674(00)81683-9

Hanahan, D., & Weinberg, R. A. (2011). Hallmarks of cancer: the next generation. *Cell*, *144*(5), 646-674. https://doi.org/10.1016/j.cell.2011.02.013

Harding, H. P., Novoa, I., Zhang, Y., Zeng, H., Wek, R., Schapira, M., & Ron, D. (2000). Regulated translation initiation controls stress-induced gene expression in mammalian cells. *Mol Cell*, *6*(5), 1099-1108. https://doi.org/10.1016/s1097-2765(00)00108-8

Harding, H. P., Zeng, H., Zhang, Y., Jungries, R., Chung, P., Plesken, H., Sabatini, D. D., & Ron, D. (2001). Diabetes mellitus and exocrine pancreatic dysfunction in perk-/- mice reveals a role for translational control in secretory cell survival. *Mol Cell*, *7*(6), 1153-1163. https://doi.org/10.1016/s1097-2765(01)00264-7

Harding, H. P., Zhang, Y., Scheuner, D., Chen, J. J., Kaufman, R. J., & Ron, D. (2009). Ppp1r15 gene knockout reveals an essential role for translation initiation factor 2 alpha (eIF2alpha) dephosphorylation in mammalian development. *Proc Natl Acad Sci U S A*, *106*(6), 1832-1837. https://doi.org/10.1073/pnas.0809632106

Harding, H. P., Zhang, Y., Zeng, H., Novoa, I., Lu, P. D., Calfon, M., Sadri, N., Yun, C., Popko, B., Paules, R., Stojdl, D. F., Bell, J. C., Hettmann, T., Leiden, J. M., & Ron, D. (2003). An integrated stress response regulates amino acid metabolism and resistance to oxidative stress. *Mol Cell*, *11*(3), 619-633. https://doi.org/10.1016/s1097-2765(03)00105-9

Heitman, J., Movva, N. R., & Hall, M. N. (1991). Targets for cell cycle arrest by the immunosuppressant rapamycin in yeast. *Science*, *253*(5022), 905-909. https://doi.org/10.1126/science.1715094

Helleday, T. (2010). Homologous recombination in cancer development, treatment and development of drug resistance. *Carcinogenesis*, *31*(6), 955-960. https://doi.org/10.1093/carcin/bgq064

Helseth, A. R., Hernandez-Martinez, R., Hall, V. L., Oliver, M. L., Turner, B. D., Caffall, Z. F., Rittiner, J. E., Shipman, M. K., King, C. S., Gradinaru, V., Gerfen, C., Costa-Mattioli, M., & Calakos, N. (2021). Cholinergic neurons constitutively engage the ISR for dopamine modulation and skill learning in mice. *Science*, *372*(6540). https://doi.org/10.1126/science.abe1931

Hennings, H., Michael, D., Cheng, C., Steinert, P., Holbrook, K., & Yuspa, S. H. (1980). Calcium regulation of growth and differentiation of mouse epidermal cells in culture. *Cell*, *19*(1), 245-254. https://doi.org/10.1016/0092-8674(80)90406-7

Hinnebusch, A. G. (1988). Mechanisms of gene regulation in the general control of amino acid biosynthesis in Saccharomyces cerevisiae. *Microbiol Rev*, *52*(2), 248-273. https://doi.org/10.1128/mr.52.2.248-273.1988

Hodgson, L., Shen, F., & Hahn, K. (2010). Biosensors for characterizing the dynamics of rho family GTPases in living cells. *Curr Protoc Cell Biol*, *Chapter 14*, Unit 14 11 11-26. https://doi.org/10.1002/0471143030.cb1411s46

Hu, Y., & Smyth, G. K. (2009). ELDA: extreme limiting dilution analysis for comparing depleted and enriched populations in stem cell and other assays. *J Immunol Methods*, *347*(1-2), 70-78. https://doi.org/10.1016/j.jim.2009.06.008

Ikebe, M., & Hartshorne, D. J. (1985). Phosphorylation of smooth muscle myosin at two distinct sites by myosin light chain kinase. *J Biol Chem*, *260*(18), 10027-10031. https://www.ncbi.nlm.nih.gov/pubmed/3839510

Ingolia, N. T., Brar, G. A., Rouskin, S., McGeachy, A. M., & Weissman, J. S. (2012). The ribosome profiling strategy for monitoring translation in vivo by deep sequencing of ribosome-protected mRNA fragments. *Nat Protoc*, *7*(8), 1534-1550. https://doi.org/10.1038/nprot.2012.086

Ingolia, N. T., Brar, G. A., Stern-Ginossar, N., Harris, M. S., Talhouarne, G. J., Jackson, S. E., Wills, M. R., & Weissman, J. S. (2014). Ribosome profiling reveals pervasive translation outside of annotated protein-coding genes. *Cell Rep*, *8*(5), 1365-1379. https://doi.org/10.1016/j.celrep.2014.07.045

Ingolia, N. T., Ghaemmaghami, S., Newman, J. R., & Weissman, J. S. (2009). Genome-wide analysis in vivo of translation with nucleotide resolution using ribosome profiling. *Science*, *324*(5924), 218-223. https://doi.org/10.1126/science.1168978

Ingolia, N. T., Lareau, L. F., & Weissman, J. S. (2011). Ribosome profiling of mouse embryonic stem cells reveals the complexity and dynamics of mammalian proteomes. *Cell*, *147*(4), 789-802. https://doi.org/10.1016/j.cell.2011.10.002

Jiang, F., & Doudna, J. A. (2017). CRISPR-Cas9 Structures and Mechanisms. *Annu Rev Biophys*, *46*, 505-529. https://doi.org/10.1146/annurev-biophys-062215-010822

Johnston, J. A., Ward, C. L., & Kopito, R. R. (1998). Aggresomes: a cellular response to misfolded proteins. *J Cell Biol*, *143*(7), 1883-1898. https://doi.org/10.1083/jcb.143.7.1883

Kim, J., & Guan, K. L. (2019). mTOR as a central hub of nutrient signalling and cell growth. *Nat Cell Biol*, *21*(1), 63-71. https://doi.org/10.1038/s41556-018-0205-1

Kodama, A., Karakesisoglou, I., Wong, E., Vaezi, A., & Fuchs, E. (2003). ACF7: an essential integrator of microtubule dynamics. *Cell*, *115*(3), 343-354. https://doi.org/10.1016/s0092-8674(03)00813-4

Kojima, E., Takeuchi, A., Haneda, M., Yagi, A., Hasegawa, T., Yamaki, K., Takeda, K., Akira, S., Shimokata, K., & Isobe, K. (2003). The function of GADD34 is a recovery from a shutoff of protein synthesis induced by ER stress: elucidation by GADD34-deficient mice. *FASEB J*, *17*(11), 1573-1575. https://doi.org/10.1096/fj.02-1184fje

Kopito, R. R. (2000). Aggresomes, inclusion bodies and protein aggregation. *Trends Cell Biol*, *10*(12), 524-530. https://doi.org/10.1016/s0962-8924(00)01852-3

Krukowski, K., Nolan, A., Frias, E. S., Boone, M., Ureta, G., Grue, K., Paladini, M. S., Elizarraras, E., Delgado, L., Bernales, S., Walter, P., & Rosi, S. (2020). Small molecule cognitive enhancer reverses age-related memory decline in mice. *Elife*, *9*. https://doi.org/10.7554/eLife.62048

Lauffenburger, D. A., & Horwitz, A. F. (1996). Cell migration: a physically integrated molecular process. *Cell*, *84*(3), 359-369. https://doi.org/10.1016/s0092-8674(00)81280-5

Leegwater, P. A., Vermeulen, G., Konst, A. A., Naidu, S., Mulders, J., Visser, A., Kersbergen, P., Mobach, D., Fonds, D., van Berkel, C. G., Lemmers, R. J., Frants, R. R., Oudejans, C. B., Schutgens, R. B., Pronk, J. C., & van der Knaap, M. S. (2001). Subunits of the translation initiation factor eIF2B are mutant in leukoencephalopathy with vanishing white matter. *Nat Genet*, *29*(4), 383-388. https://doi.org/10.1038/ng764

Lehman, S. L., Ryeom, S., & Koumenis, C. (2015). Signaling through alternative Integrated Stress Response pathways compensates for GCN2 loss in a mouse model of soft tissue sarcoma. *Sci Rep*, *5*, 11781. https://doi.org/10.1038/srep11781

Liu, J., Xu, Y., Stoleru, D., & Salic, A. (2012). Imaging protein synthesis in cells and tissues with an alkyne analog of puromycin. *Proc Natl Acad Sci U S A*, *109*(2), 413-418. https://doi.org/10.1073/pnas.1111561108

Liu, Q., Kang, S. A., Thoreen, C. C., Hur, W., Wang, J., Chang, J. W., Markhard, A., Zhang, J., Sim, T., Sabatini, D. M., & Gray, N. S. (2012). Development of ATP-competitive mTOR inhibitors. *Methods Mol Biol*, *821*, 447-460. https://doi.org/10.1007/978-1-61779-430-8_29

Love, M. I., Huber, W., & Anders, S. (2014). Moderated estimation of fold change and dispersion for RNA-seq data with DESeq2. *Genome Biol*, *15*(12), 550. https://doi.org/10.1186/s13059-014-0550-8

Madarampalli, B., Yuan, Y., Liu, D., Lengel, K., Xu, Y., Li, G., Yang, J., Liu, X., Lu, Z., & Liu, D. X. (2015). ATF5 Connects the Pericentriolar Materials to the Proximal End of the Mother Centriole. *Cell*, *162*(3), 580-592. https://doi.org/10.1016/j.cell.2015.06.055

McEwen, E., Kedersha, N., Song, B., Scheuner, D., Gilks, N., Han, A., Chen, J. J., Anderson, P., & Kaufman, R. J. (2005). Heme-regulated inhibitor kinase-mediated phosphorylation of eukaryotic translation initiation factor 2 inhibits translation, induces stress granule formation, and mediates survival upon arsenite exposure. *J Biol Chem*, *280*(17), 16925-16933. https://doi.org/10.1074/jbc.M412882200

McGlincy, N. J., & Ingolia, N. T. (2017). Transcriptome-wide measurement of translation by ribosome profiling. *Methods*, *126*, 112-129. https://doi.org/10.1016/j.ymeth.2017.05.028

Meijer, H. A., & Thomas, A. A. (2002). Control of eukaryotic protein synthesis by upstream open reading frames in the 5'-untranslated region of an mRNA. *Biochem J*, *367*(Pt 1), 1-11. https://doi.org/10.1042/BJ20011706

Meurs, E., Chong, K., Galabru, J., Thomas, N. S., Kerr, I. M., Williams, B. R., & Hovanessian, A. G. (1990). Molecular cloning and characterization of the human double-stranded RNA-activated protein kinase induced by interferon. *Cell*, *62*(2), 379-390. https://doi.org/10.1016/0092-8674(90)90374-n

Meyer, H. J., & Rape, M. (2014). Enhanced protein degradation by branched ubiquitin chains. *Cell*, *157*(4), 910-921. https://doi.org/10.1016/j.cell.2014.03.037

Mimnaugh, E. G., Xu, W., Vos, M., Yuan, X., & Neckers, L. (2006). Endoplasmic reticulum vacuolization and valosin-containing protein relocalization result from simultaneous hsp90 inhibition by geldanamycin and proteasome inhibition by velcade. *Mol Cancer Res*, *4*(9), 667-681. https://doi.org/10.1158/1541-7786.MCR-06-0019

Musch, A. (2004). Microtubule organization and function in epithelial cells. *Traffic*, *5*(1), 1-9. https://doi.org/10.1111/j.1600-0854.2003.00149.x

Nandi, D., Tahiliani, P., Kumar, A., & Chandu, D. (2006). The ubiquitin-proteasome system. *J Biosci*, *31*(1), 137-155. https://doi.org/10.1007/BF02705243

Nassar, D., Latil, M., Boeckx, B., Lambrechts, D., & Blanpain, C. (2015). Genomic landscape of carcinogen-induced and genetically induced mouse skin squamous cell carcinoma. *Nat Med*, *21*(8), 946-954. https://doi.org/10.1038/nm.3878

Nedelsky, N. B., & Taylor, J. P. (2019). Bridging biophysics and neurology: aberrant phase transitions in neurodegenerative disease. *Nat Rev Neurol*, *15*(5), 272-286. https://doi.org/10.1038/s41582-019-0157-5

Nguyen, H. G., Conn, C. S., Kye, Y., Xue, L., Forester, C. M., Cowan, J. E., Hsieh, A. C., Cunningham, J. T., Truillet, C., Tameire, F., Evans, M. J., Evans, C. P., Yang, J. C., Hann, B., Koumenis, C., Walter, P., Carroll, P. R., & Ruggero, D. (2018). Development of a stress response therapy targeting aggressive prostate cancer. *Sci Transl Med*, *10*(439). https://doi.org/10.1126/scitranslmed.aar2036

Ochaba, J., Morozko, E. L., O'Rourke, J. G., & Thompson, L. M. (2018). Fractionation for Resolution of Soluble and Insoluble Huntingtin Species. *J Vis Exp*(132). https://doi.org/10.3791/57082

Ohoka, N., Yoshii, S., Hattori, T., Onozaki, K., & Hayashi, H. (2005). TRB3, a novel ER stress-inducible gene, is induced via ATF4-CHOP pathway and is involved in cell death. *EMBO J*, *24*(6), 1243-1255. https://doi.org/10.1038/sj.emboj.7600596

Olzscha, H., Schermann, S. M., Woerner, A. C., Pinkert, S., Hecht, M. H., Tartaglia, G. G., Vendruscolo, M., Hayer-Hartl, M., Hartl, F. U., & Vabulas, R. M. (2011). Amyloid-like aggregates sequester numerous metastable proteins with essential cellular functions. *Cell*, *144*(1), 67-78. https://doi.org/10.1016/j.cell.2010.11.050

Pakos-Zebrucka, K., Koryga, I., Mnich, K., Ljujic, M., Samali, A., & Gorman, A. M. (2016). The integrated stress response. *EMBO Rep*, *17*(10), 1374-1395. https://doi.org/10.15252/embr.201642195

Panegyres, P. K., & Chen, H. Y. (2021). Alzheimer's disease, Huntington's disease and cancer. *J Clin Neurosci*, *93*, 103-105. https://doi.org/10.1016/j.jocn.2021.09.012

Paramore, A., & Frantz, S. (2003). Bortezomib. *Nat Rev Drug Discov*, *2*(8), 611-612. https://doi.org/10.1038/nrd1159

Perez, A. R., Pritykin, Y., Vidigal, J. A., Chhangawala, S., Zamparo, L., Leslie, C. S., & Ventura, A. (2017). GuideScan software for improved single and paired CRISPR guide RNA design. *Nat Biotechnol*, *35*(4), 347-349. https://doi.org/10.1038/nbt.3804

Rabouw, H. H., Langereis, M. A., Anand, A. A., Visser, L. J., de Groot, R. J., Walter, P., & van Kuppeveld, F. J. M. (2019). Small molecule ISRIB suppresses the integrated stress response within a defined window of activation. *Proc Natl Acad Sci U S A*, *116*(6), 2097-2102. https://doi.org/10.1073/pnas.1815767116

Rajagopalan, H., & Lengauer, C. (2004). Aneuploidy and cancer. *Nature*, *432*(7015), 338-341. https://doi.org/10.1038/nature03099

Rouschop, K. M., Dubois, L. J., Keulers, T. G., van den Beucken, T., Lambin, P., Bussink, J., van der Kogel, A. J., Koritzinsky, M., & Wouters, B. G. (2013). PERK/eIF2alpha signaling protects therapy resistant hypoxic cells through induction of glutathione synthesis and protection against ROS. *Proc Natl Acad Sci U S A*, *110*(12), 4622-4627. https://doi.org/10.1073/pnas.1210633110

Salaroglio, I. C., Panada, E., Moiso, E., Buondonno, I., Provero, P., Rubinstein, M., Kopecka, J., & Riganti, C. (2017). PERK induces resistance to cell death elicited by endoplasmic reticulum stress and chemotherapy. *Mol Cancer*, *16*(1), 91. https://doi.org/10.1186/s12943-017-0657-0

Sanchez, A. D., & Feldman, J. L. (2017). Microtubule-organizing centers: from the centrosome to non-centrosomal sites. *Curr Opin Cell Biol*, *44*, 93-101. https://doi.org/10.1016/j.ceb.2016.09.003

Sansbury, B. M., Hewes, A. M., & Kmiec, E. B. (2019). Understanding the diversity of genetic outcomes from CRISPR-Cas generated homology-directed repair. *Commun Biol*, *2*, 458. https://doi.org/10.1038/s42003-019-0705-y

Santagata, S., Hu, R., Lin, N. U., Mendillo, M. L., Collins, L. C., Hankinson, S. E., Schnitt, S. J., Whitesell, L., Tamimi, R. M., Lindquist, S., & Ince, T. A. (2011). High levels of nuclear heat-shock factor 1 (HSF1) are associated with poor prognosis in breast cancer. *Proc Natl Acad Sci U S A*, *108*(45), 18378-18383. https://doi.org/10.1073/pnas.1115031108

Saxton, R. A., & Sabatini, D. M. (2017). mTOR Signaling in Growth, Metabolism, and Disease. *Cell*, *168*(6), 960-976. https://doi.org/10.1016/j.cell.2017.02.004

Scheuner, D., Song, B., McEwen, E., Liu, C., Laybutt, R., Gillespie, P., Saunders, T., Bonner-Weir, S., & Kaufman, R. J. (2001). Translational control is required for the unfolded protein response and in vivo glucose homeostasis. *Mol Cell*, *7*(6), 1165-1176. https://doi.org/10.1016/s1097-2765(01)00265-9

Schiffmann, R., Moller, J. R., Trapp, B. D., Shih, H. H., Farrer, R. G., Katz, D. A., Alger, J. R., Parker, C. C., Hauer, P. E., Kaneski, C. R., & et al. (1994). Childhood ataxia with diffuse central nervous system hypomyelination. *Ann Neurol*, *35*(3), 331-340. https://doi.org/10.1002/ana.410350314

Schober, M., & Fuchs, E. (2011). Tumor-initiating stem cells of squamous cell carcinomas and their control by TGF-beta and integrin/focal adhesion kinase (FAK) signaling. *Proc Natl Acad Sci U S A*, *108*(26), 10544-10549. https://doi.org/10.1073/pnas.1107807108

Schober, M., Raghavan, S., Nikolova, M., Polak, L., Pasolli, H. A., Beggs, H. E., Reichardt, L. F., & Fuchs, E. (2007). Focal adhesion kinase modulates tension signaling to control actin and focal adhesion dynamics. *J Cell Biol*, *176*(5), 667-680. https://doi.org/10.1083/jcb.200608010

Schwanhausser, B., Busse, D., Li, N., Dittmar, G., Schuchhardt, J., Wolf, J., Chen, W., & Selbach, M. (2011). Global quantification of mammalian gene expression control. *Nature*, *473*(7347), 337-342. https://doi.org/10.1038/nature10098

Sehgal, S. N., Baker, H., & Vezina, C. (1975). Rapamycin (AY-22,989), a new antifungal antibiotic. II. Fermentation, isolation and characterization. *J Antibiot (Tokyo)*, *28*(10), 727-732. https://doi.org/10.7164/antibiotics.28.727

Sendoel, A., Dunn, J. G., Rodriguez, E. H., Naik, S., Gomez, N. C., Hurwitz, B., Levorse, J., Dill, B. D., Schramek, D., Molina, H., Weissman, J. S., & Fuchs, E. (2017). Translation from unconventional 5' start sites drives tumour initiation. *Nature*, *541*(7638), 494-499. https://doi.org/10.1038/nature21036

Shi, H. B., Tang, B., Liu, Y. W., Wang, X. F., & Chen, G. J. (2015). Alzheimer disease and cancer risk: a meta-analysis. *J Cancer Res Clin Oncol*, *141*(3), 485-494. https://doi.org/10.1007/s00432-014-1773-5

Shi, Y., Vattem, K. M., Sood, R., An, J., Liang, J., Stramm, L., & Wek, R. C. (1998). Identification and characterization of pancreatic eukaryotic initiation factor 2 alpha-subunit kinase, PEK, involved in translational control. *Mol Cell Biol*, *18*(12), 7499-7509. https://doi.org/10.1128/MCB.18.12.7499

Sidrauski, C., Acosta-Alvear, D., Khoutorsky, A., Vedantham, P., Hearn, B. R., Li, H., Gamache, K., Gallagher, C. M., Ang, K. K., Wilson, C., Okreglak, V., Ashkenazi, A., Hann, B., Nader, K., Arkin, M. R., Renslo, A. R., Sonenberg, N., & Walter, P. (2013). Pharmacological brake-release of mRNA translation enhances cognitive memory. *Elife*, *2*, e00498. https://doi.org/10.7554/eLife.00498

Sidrauski, C., McGeachy, A. M., Ingolia, N. T., & Walter, P. (2015). The small molecule ISRIB reverses the effects of eIF2alpha phosphorylation on translation and stress granule assembly. *Elife*, *4*. https://doi.org/10.7554/eLife.05033

Signer, R. A., Magee, J. A., Salic, A., & Morrison, S. J. (2014). Haematopoietic stem cells require a highly regulated protein synthesis rate. *Nature*, *509*(7498), 49-54. https://doi.org/10.1038/nature13035

Skopkova, M., Hennig, F., Shin, B. S., Turner, C. E., Stanikova, D., Brennerova, K., Stanik, J., Fischer, U., Henden, L., Muller, U., Steinberger, D., Leshinsky-Silver, E., Bottani, A., Kurdiova, T., Ukropec, J., Nyitrayova, O., Kolnikova, M., Klimes, I., Borck, G., Bahlo, M., Haas, S. A., Kim, J. R., Lotspeich-Cole, L. E., Gasperikova, D., Dever, T. E., & Kalscheuer, V. M. (2017). EIF2S3 Mutations Associated with Severe X-Linked Intellectual Disability Syndrome MEHMO. *Hum Mutat*, *38*(4), 409-425. https://doi.org/10.1002/humu.23170

Starck, S. R., Jiang, V., Pavon-Eternod, M., Prasad, S., McCarthy, B., Pan, T., & Shastri, N. (2012). Leucine-tRNA initiates at CUG start codons for protein synthesis and presentation by MHC class I. *Science*, *336*(6089), 1719-1723. https://doi.org/10.1126/science.1220270

Starck, S. R., Tsai, J. C., Chen, K., Shodiya, M., Wang, L., Yahiro, K., Martins-Green, M., Shastri, N., & Walter, P. (2016). Translation from the 5' untranslated region shapes the integrated stress response. *Science*, *351*(6272), aad3867. https://doi.org/10.1126/science.aad3867

Thrower, J. S., Hoffman, L., Rechsteiner, M., & Pickart, C. M. (2000). Recognition of the polyubiquitin proteolytic signal. *EMBO J*, *19*(1), 94-102. https://doi.org/10.1093/emboj/19.1.94

Tian, X., Zhang, S., Zhou, L., Seyhan, A. A., Hernandez Borrero, L., Zhang, Y., & El-Deiry, W. S. (2021). Targeting the Integrated Stress Response in Cancer Therapy. *Front Pharmacol*, *12*, 747837. https://doi.org/10.3389/fphar.2021.747837

Tinkle, C. L., Lechler, T., Pasolli, H. A., & Fuchs, E. (2004). Conditional targeting of E-cadherin in skin: insights into hyperproliferative and degenerative responses. *Proc Natl Acad Sci U S A*, *101*(2), 552-557. https://doi.org/10.1073/pnas.0307437100

Valastyan, J. S., & Lindquist, S. (2014). Mechanisms of protein-folding diseases at a glance. *Dis Model Mech*, *7*(1), 9-14. https://doi.org/10.1242/dmm.013474

Walter, P., & Ron, D. (2011). The unfolded protein response: from stress pathway to homeostatic regulation. *Science*, *334*(6059), 1081-1086. https://doi.org/10.1126/science.1209038

Wek, R. C., Ramirez, M., Jackson, B. M., & Hinnebusch, A. G. (1990). Identification of positive-acting domains in GCN2 protein kinase required for translational activation of

GCN4 expression. *Mol Cell Biol*, *10*(6), 2820-2831. https://doi.org/10.1128/mcb.10.6.2820-2831.1990

Wojcik, C., Yano, M., & DeMartino, G. N. (2004). RNA interference of valosin-containing protein (VCP/p97) reveals multiple cellular roles linked to ubiquitin/proteasome-dependent proteolysis. *J Cell Sci*, *117*(Pt 2), 281-292. https://doi.org/10.1242/jcs.00841

Wolfenson, H., Yang, B., & Sheetz, M. P. (2019). Steps in Mechanotransduction Pathways that Control Cell Morphology. *Annu Rev Physiol*, *81*, 585-605. https://doi.org/10.1146/annurev-physiol-021317-121245

Wong, K., Armstrong, R. C., Gyure, K. A., Morrison, A. L., Rodriguez, D., Matalon, R., Johnson, A. B., Wollmann, R., Gilbert, E., Le, T. Q., Bradley, C. A., Crutchfield, K., & Schiffmann, R. (2000). Foamy cells with oligodendroglial phenotype in childhood ataxia with diffuse central nervous system hypomyelination syndrome. *Acta Neuropathol*, *100*(6), 635-646. https://doi.org/10.1007/s004010000234

Wong, Y. L., LeBon, L., Edalji, R., Lim, H. B., Sun, C., & Sidrauski, C. (2018). The small molecule ISRIB rescues the stability and activity of Vanishing White Matter Disease eIF2B mutant complexes. *Elife*, *7*. https://doi.org/10.7554/eLife.32733

Woodruff, J. B., Ferreira Gomes, B., Widlund, P. O., Mahamid, J., Honigmann, A., & Hyman, A. A. (2017). The Centrosome Is a Selective Condensate that Nucleates Microtubules by Concentrating Tubulin. *Cell*, *169*(6), 1066-1077 e1010. https://doi.org/10.1016/j.cell.2017.05.028

Wu, X., Kodama, A., & Fuchs, E. (2008). ACF7 regulates cytoskeletal-focal adhesion dynamics and migration and has ATPase activity. *Cell*, *135*(1), 137-148. https://doi.org/10.1016/j.cell.2008.07.045

Yang, H., Li, J. J., Liu, S., Zhao, J., Jiang, Y. J., Song, A. X., & Hu, H. Y. (2014). Aggregation of polyglutamine-expanded ataxin-3 sequesters its specific interacting partners into inclusions: implication in a loss-of-function pathology. *Sci Rep*, *4*, 6410. https://doi.org/10.1038/srep06410

Yang, H., Schramek, D., Adam, R. C., Keyes, B. E., Wang, P., Zheng, D., & Fuchs, E. (2015). ETS family transcriptional regulators drive chromatin dynamics and malignancy in squamous cell carcinomas. *Elife*, *4*, e10870. https://doi.org/10.7554/eLife.10870

Yang, Y. L., Reis, L. F., Pavlovic, J., Aguzzi, A., Schafer, R., Kumar, A., Williams, B. R., Aguet, M., & Weissmann, C. (1995). Deficient signaling in mice devoid of double-stranded RNA-dependent protein kinase. *EMBO J*, *14*(24), 6095-6106. https://www.ncbi.nlm.nih.gov/pubmed/8557029

Young-Baird, S. K., Lourenco, M. B., Elder, M. K., Klann, E., Liebau, S., & Dever, T. E. (2020). Suppression of MEHMO Syndrome Mutation in eIF2 by Small Molecule ISRIB. *Mol Cell*, *77*(4), 875-886 e877. https://doi.org/10.1016/j.molcel.2019.11.008

Zaffagnini, G., Savova, A., Danieli, A., Romanov, J., Tremel, S., Ebner, M., Peterbauer, T., Sztacho, M., Trapannone, R., Tarafder, A. K., Sachse, C., & Martens, S. (2018). p62 filaments capture and present ubiquitinated cargos for autophagy. *EMBO J*, *37*(5). https://doi.org/10.15252/embj.201798308

Zhang, P., McGrath, B., Li, S., Frank, A., Zambito, F., Reinert, J., Gannon, M., Ma, K., McNaughton, K., & Cavener, D. R. (2002). The PERK eukaryotic initiation factor 2 alpha kinase is required for the development of the skeletal system, postnatal growth, and the function and viability of the pancreas. *Mol Cell Biol*, *22*(11), 3864-3874. https://doi.org/10.1128/MCB.22.11.3864-3874.2002

Zhu, P. J., Huang, W., Kalikulov, D., Yoo, J. W., Placzek, A. N., Stoica, L., Zhou, H., Bell, J. C., Friedlander, M. J., Krnjevic, K., Noebels, J. L., & Costa-Mattioli, M. (2011). Suppression of PKR promotes network excitability and enhanced cognition by interferon-gamma-mediated disinhibition. *Cell*, *147*(6), 1384-1396. https://doi.org/10.1016/j.cell.2011.11.029

Zhu, P. J., Khatiwada, S., Cui, Y., Reineke, L. C., Dooling, S. W., Kim, J. J., Li, W., Walter, P., & Costa-Mattioli, M. (2019). Activation of the ISR mediates the behavioral and neurophysiological abnormalities in Down syndrome. *Science*, *366*(6467), 843-849. https://doi.org/10.1126/science.aaw5185